

Effects of Geometric Nonlinearities on the Fidelity of  
Aeroelasticity Loads Analyses of Very Flexible Airframes

By

Muhammadh Ali Abdhullah Salman  
M.Eng. in Aerospace Studies

A thesis submitted to the Faculty of Graduate and Postdoctoral  
Affairs in partial fulfillment of the requirements for the degree of  
Master of Applied Science  
in  
Aerospace Engineering

Carleton University  
Ottawa, Ontario

## **Abstract**

In this thesis, a modified iterative methodology is proposed, which improves upon existing work in literature by including geometrically nonlinear large rotation effects along the wingspan as an additional downwash into the methodology to improve the fidelity of the calculated loads. It is found that when the airframe is highly flexible, significant increases in the critical wing root loads are observed, as well as substantial changes in the trimmed aircraft configurations.

A sensitivity analysis is performed on aircraft wing loads due to geometric nonlinearity, with respect to a number of conceptual design parameters. The parameters found to be most significantly affected by geometrically nonlinear effects in dynamic aeroelasticity are the out of plane stiffness of the aircraft and the position of the aerodynamic centre of the wing. Changes in stiffness are found to have highly nonlinear effects on the resultant bending moments, requiring full calculation of the entire design space.

**Keywords:** *Aeroelasticity, Nonlinear Aeroelasticity, Geometric Nonlinearity, Dynamic Aeroelasticity, Sensitivity Analysis, Nonlinear Loads Analysis.*

## **Preface**

The following thesis is an original work developed by Muhammadh Ali Abdhullah Salman, under the supervision of Professor Mostafa ElSayed, conforming to all requirements, as stated by Carleton University.

The work done in the thesis is part of the Bombardier Aerospace MuFOX multidisciplinary project. Bombardier Aerospace has provided the author with structural and aeroelastic model data which was used in Chapters 3.3, 5, and 0. All output data has been normalized to protect Bombardier's Intellectual Property.

The work presented in Chapter 4 has been published in the Journal of Aeroelasticity and Structural Dynamics under the title "Structural Nonlinearities and their Impact on the Fidelity of Critical Steady Maneuver Loads and Trimming Configuration of Very Flexible Airframes", co-authored by Professor Mostafa ElSayed and Denis Walch [1].

The work presented in Chapters 5 and 6 is currently being formatted for submission to peer-reviewed publication.

## **Acknowledgements**

I would like to express my deepest gratitude to my supervisor, Professor Mostafa El Sayed, for his advice, support, and guidance throughout the course of my research.

I would like also to thank Mr. Denis Walch of Bombardier Aerospace for his valuable input and suggestions towards the progress of this work.

The work performed in this project would not have been possible without the financial support from Bombardier Aerospace, in collaboration with CARIC Montreal and MITACS Canada.

My friends and coworkers in the Aerospace Structures and Materials Engineering Laboratory at Carleton University have been very helpful over these past two years, and I am grateful for all the eye-opening conversations and useful comments and feedback. Sincere thanks to Paul Thomas and Michelle Guzman for the friendly and fun conversations, valuable feedback, and most certainly their valued friendship.

Last but not least, my deepest thanks to my parents for their love, kindness, endless support, and encouragement.

# Table of Contents

Acknowledgements.....	iv
Table of Contents.....	v
Nomenclature.....	ix
List of Figures.....	xvii
List of Tables.....	xxii
1 Introduction.....	23
1.1 Background.....	23
1.2 Motivation.....	24
1.3 Literature Review.....	25
1.3.1 Modeling of geometric nonlinearities.....	25
1.3.2 Nonlinear aeroelastic modeling strategies.....	28
1.4 Thesis Objective.....	28
1.5 Thesis Outline.....	29
1.6 Thesis Contribution.....	30
2 Review of Nonlinear Beam Models.....	32
2.1 Displacement Based Method.....	32
2.2 Strain based geometrically nonlinear beam.....	45
2.3 Modal superposition method.....	51
2.4 Intrinsic Formulation.....	53

2.5	Chapter Summary.....	60
3	Case Study - Cantilever Beam Problem.....	61
3.1	Numerical solution of nonlinear equations .....	62
3.2	Verification of results.....	64
3.2.1	Static test results .....	64
3.2.2	Dynamic test results.....	66
3.3	Key differences between formulations.....	68
3.4	Chapter Summary.....	69
4	Nonlinear Static Aeroelasticity.....	70
4.1	Theoretical Formulation.....	70
4.1.1	Nonlinear Structural Formulation.....	70
4.1.2	Nonlinear Aeroelasticity Formulation .....	72
4.1.3	Linear Aerodynamic Formulation.....	74
4.2	Methodology .....	77
4.2.1	Modified Iterative Method.....	78
4.2.2	Case Study .....	81
4.2.3	Limitations .....	90
4.3	Results .....	90
4.3.1	Steady flight conditions .....	91
4.3.2	Variation of root angle of attack.....	96

4.3.3	Parametric variation of equivalent beam dimensions .....	98
4.4	Chapter Summary.....	111
5	Dynamic Aeroelasticity: Parametric Case Study.....	112
5.1	Theoretical Framework .....	113
5.1.1	Sensitivity Analysis .....	113
5.1.2	Mass and stiffness variation.....	114
5.1.3	ASWING beam model.....	117
5.1.4	Aeroelastic model .....	120
5.1.5	Aerodynamic Model .....	122
5.1.6	Discrete Gust Model .....	125
5.2	Case Study.....	125
5.2.1	Sensitivity due to change in wing stiffness distribution .....	127
5.2.2	Sensitivity by central difference method .....	127
5.3	Results and Discussion.....	128
5.3.1	Baseline comparison .....	128
5.3.2	Variation of Aircraft Design Parameters .....	129
5.4	Chapter Summary.....	139
6	Dynamic Aeroelasticity: Sensitivity Analysis .....	140
6.1	Changes in wing stiffness.....	140
6.2	Changes in wing and tail aerodynamic centre.....	141

6.3	Changes in engine mass and position.....	142
6.4	Chapter Summary.....	144
7	Conclusion .....	146
8	References.....	149
Appendix A: Strain Based Formulation Matrices.....		159
	Matrix exponential $e^{\mathbf{A}(\boldsymbol{\xi} - \boldsymbol{\xi}_0)}$ .....	159
	Jacobian Matrices.....	160
	Matrix $\mathbf{J}\mathbf{h}\boldsymbol{\varepsilon}$ .....	160
	Matrix $\mathbf{J}\mathbf{p}\boldsymbol{\varepsilon}$ .....	163
	Matrix $\mathbf{J}\boldsymbol{\theta}\boldsymbol{\varepsilon}$ .....	163
Appendix B: Intrinsic Formulation Matrices.....		166

# Nomenclature

Uppercase letters	Definition
$A$	Cross sectional area
$A$	Strain/Curvature matrix
$A_{AIC}$	Aerodynamic influence coefficient matrix
$B_{grav}, B_F, B_M$	Force, Moment transformation matrices
$B$	Body frame
$B$	Displacement transformation matrix: elemental to global frame
$B^G, B^L$	Nonlinear, linear, strain-displacement matrices
$C$	Linear elastic constitutive matrix
$C^{wb}, C$	Rotation vector between deformed and undeformed frame
$C$	Damping matrix
$D$	Displacement-downwash matrix
$D_\sigma$	<b>D</b> matrix for aerodynamic degrees of freedom
$D_{ij}$	Elements of <b>D</b> matrix
$E$	Young's Modulus
$F$	Elemental force (generalized)
$F_{point}, F_{dist}$	Point and distributed elemental forces
$F$	Force vector (internal or external)
$G$	Shear modulus
$G_{spline}$	Aero-structure splining matrix
$H$	Elemental angular momenta

$I_{11}, I_{22}, I_{33}$	Second moments of area
$\hat{I}_{11}, \hat{I}_{22}$	Normalized Second moments of area
$I_{xx}, I_{yy}, I_{zz}$	Mass moments of inertia
$J$	Torsional moment of area
$\hat{J}$	Normalized torsional moment of area
$J$	Jacobian matrix
$K_l$	Components of stiffness matrix
$\mathbf{K}$	Stiffness matrix
$\mathcal{K}$	Kinetic energy
$K_1, K_2, K_y, K_z$	Shear area factors
$L_o, L_f$	Initial and deformed length of beam
$L_{gust}$	Length of gust disturbance
$L_i$	Length of beam element $i$
$M$	Bending moment in element
$M_{point}, M_{dist}$	Point and distributed elemental moments
$\mathbf{M}$	Mass matrix
$M$	Components of mass matrix
$\hat{M}$	Normalized mass
$N$	Elemental axial force
$P$	Elemental linear momenta
$\mathbf{P}$	Deformed beam point position vector
$Q_{WM}$	Matrix used for rotation parameters

<b>Q</b>	Downwash-nodal force matrix
<b>Q<sub>σ</sub></b>	<b>Q</b> matrix for aerodynamic degrees of freedom
<b>R</b>	External applied force vector
<i>S<sub>ij</sub></i>	Components of Second Piola-Kirchhoff stress
<i>U<sub>gust</sub></i>	Gust velocity
<i>U<sub>free</sub></i>	Free stream velocity of airflow
<b>U</b>	Physical deformation/displacement vector
<b>U<sub>n</sub></b>	Displacement vector for aircraft wing nodes
<i>u</i>	Potential energy
<i>V</i>	Volume
<i>W</i>	Work
<i>X</i>	Gust penetration distance
<b>Z</b>	GEBT formulation finite element matrices

<b>Lowercase letters</b>	<b>Definition</b>
$a$	Equivalent beam half-width
$a_{th}$	Equivalent thin-beam width
$\hat{a}_i$	Newmark method coefficients, $i \in \{1, \dots, 7\}$
$b$	Equivalent beam half-height
$b_{th}$	Equivalent thin-beam height
$\mathbf{b}$	Undeformed beam local reference frame
$\mathbf{b}_i$	Columns of $\mathbf{B}$ matrix, $i \in \{1,2,3\}$
$\underline{c}, \underline{c}_0$	Cosine
$c_{WM}$	Rotation variable parameters
$e^{A(\xi-\xi_0)}, e^{\bar{G}}, e^{\overline{2G}}$	Exponential matrices
$e_1$	Unit direction vector
$\check{f}_i$	Distributed load on element $i$ .
$\hat{f}_{aero}$	Aerodynamic pressure
$\mathbf{f}$	Arbitrary force
$g$	Gravity
$g_g$	Flight profile load alleviation factor
$h$	Position and orientation vector
$i$	Integer count/increment
$j$	Integer count/increment
$j1, j2$	Start and end points of arbitrary beam element
$k$	Integer count/increment

$l$	Arbitrary length
$m$	Mass per unit length
$\check{m}_i$	Distributed moment on element $i$ .
$p$	Position vector, global coordinate system
$\mathbf{p}$	Beam point position vector
$\mathbf{p}$	Undeformed beam point position vector
$q_{\text{dyn}}$	Dynamic Pressure
$q$	Generalized displacement vector
$\mathbf{q}$	Displacement variation vectors
$\mathbf{r}$	Displacement variation vectors
$r_x, r_y, r_z$	$x, y, z$ distance from element c.g. to beam neutral axis
$\underline{s}, \underline{s}_0$	Sine
$t$	Time
$t_{th}$	Equivalent thin-beam wall thickness
$u_1, u_2$	Deformation in $x$ -axis, global coordinate system
$\bar{u}$	Element elongation
$\hat{u}$	Element deformation, local coordinate system
$\hat{u}_\sigma$	Aerodynamic degrees of freedom
$\mathbf{v}_w$	Beam velocity, local coordinate system
$\mathbf{v}_B$	Rigid body velocities of beam, global coordinate system
$\hat{v}$	Element deformation, local coordinate system
$v_1, v_2$	Deformation in $y$ -axis, global coordinate system

$\hat{w}$	Downwash
$w_x, w_y, w_z$	Local orientation vector, global coordinate system
$x, y, z$	Arbitrary coordinates in any coordinate system
$x_1, x_2$	Nodal coordinates, global coordinate system
$\hat{x}$	Distance along element neutral axis
$y_1, y_2$	Nodal coordinates, global coordinate system
$\hat{y}$	Distance perpendicular to element neutral axis
$z_1, z_2$	Nodal coordinates, global coordinate system

<b>Greek letters</b>	<b>Definition</b>
$\alpha$	Rigid body rotation of element
$\alpha_0$	Angle of attack
$\hat{\alpha}$	Coefficient used in strain formulation
$\beta, \beta_0$	Element angle with $x$ -axis, global coordinate system
$\boldsymbol{\beta}$	Beam velocity and angular velocity vector
$\delta$	Infinitesimal variation
$\delta q$	Generalized displacement
$\delta\psi$	Generalized rotation
$\Delta$	Difference in quantity
$\mathbf{\Delta}$	Arbitrary structural parameter/configuration
$\varepsilon, \varepsilon_x$	Extensional strain
$\boldsymbol{\varepsilon}$	Strain degrees of freedom vector
$\hat{\Gamma}$	Kernel function for non-planar surface
$\gamma$	Element curvature (translational)
$\kappa, \kappa_y, \kappa_z$	Element curvature (rotational)
$\bar{\kappa}$	Undeformed beam curvature, global coordinate system
$\boldsymbol{\kappa}$	Deformed beam curvature, global coordinate system
$\lambda$	Sweep angle
$\hat{\xi}$	1D linear shape function
$\xi$	Normalized distance along beam
$\eta$	Parametric distance along wingspan

$\rho$	Density
$\sigma$	Stress
$\psi$	generalized
$\omega_B$	Angular velocities of beam, global coordinate system
$\omega_w$	Angular velocity of beam element, deformed frame
$\theta_1, \theta_2$	Nodal rotations, local coordinate system
$\bar{\theta}_1, \bar{\theta}_2$	Nodal rotations, global coordinate system
$\zeta$	Sensitivity

# List of Figures

Figure 1: Aeroelastic load calculation process .....	23
Figure 2: Beam element in global coordinate system [52] .....	33
Figure 3: An infinitesimal increment to the displacement.....	36
Figure 4: Frames of reference used in the intrinsic beam formulation .....	54
Figure 5: Cantilever beam used verification of nonlinear methodologies .....	61
Figure 6: Deformed configuration of cantilever beam subject to gravity load.....	65
Figure 7: Bending moment across length of cantilever beam.....	65
Figure 8: Tip displacement of cantilever beam as a function of time.....	68
Figure 9: Dynamic bending moment at clamped end of cantilever beam .....	68
Figure 10: Flowchart depicting the Modified Nastran Iterative Method.....	79
Figure 11: Reduction from Global Finite Element Model (GFEM) to a Stick Model (SM) for a generic twin engine aircraft .....	82
Figure 12: Schematic drawing showing GFEM reduction process to Stick Model.....	83
Figure 13: Comparison of normalized bending moment along wingspan of GFEM and Stick Model.....	85
Figure 14: Comparison of normalized shear force along wingspan of GFEM and Stick Model .....	86
Figure 15: Comparison of normalized torsional moment along wingspan of GFEM and Stick Model.....	86
Figure 16: Variation of the in-plane stiffness, torsional stiffness, and element mass, as a function of out of plane stiffness .....	88

Figure 17: Displaced wing profile comparison between linear SOL 144 and nonlinear iterative method. Deformation has been magnified $\times 3$ .....	90
Figure 18: Comparison of local angle of attack, $\alpha L$ , along wingspan for linear and nonlinear methods.....	91
Figure 19: Comparison of out of plane bending moment along wingspan for linear and nonlinear methods.....	93
Figure 20: Comparison of out of plane shear force along wingspan for linear and nonlinear methods.....	93
Figure 21: Comparison of twisting moment along wingspan for linear and nonlinear methods.....	94
Figure 22: Comparison of out of plane bending moment along wingspan between ASWING and the modified nonlinear iterative method.....	95
Figure 23: Comparison of out of plane shear force along wingspan between ASWING and the modified nonlinear iterative method.....	95
Figure 24: Comparison of out of plane bending moment at wing root, for linear and iterative nonlinear aeroelastic solution methods.....	97
Figure 25: Comparison of out of plane shear force at wing root, for linear and iterative nonlinear aeroelastic solution methods.....	97
Figure 26: Comparison of torsional moment at wing root, for linear and iterative nonlinear aeroelastic solution methods.....	98
Figure 27: Increase in nonlinear load (out of plane bending moment) at the wing root, $\Delta e$ , compared to the corresponding linear load, with parametric variations of the in and out of plane stiffnesses, $I_{22}$ , and $I_{11}$ . .....	99

Figure 28: Increase in nonlinear load (out of plane shear force) at the wing root with parametric variations of the in and out of plane stiffnesses, $I_{22}$ , and $I_{11}$ .	100
Figure 29: Increase in nonlinear load (torsional moment) at the wing root with parametric variations of the in and out of plane stiffnesses, $I_{22}$ , and $I_{11}$ .	100
Figure 30: Nonlinear increase in loads at wing root, $\Delta e$ , as the out of plane stiffness, $I_{11}$ , is varied	101
Figure 31: Increase in tip deflection, $\Delta utip$ , due to nonlinearity, as the out of plane stiffness, $I_{11}$ , is varied.	102
Figure 32: Normalized nonlinear out of plane bending moment across wingspan as stiffness varies.	104
Figure 33: Normalized nonlinear out of plane shear force across wingspan as stiffness varies.	104
Figure 34: Normalized nonlinear torsional moment across wingspan as stiffness varies.	105
Figure 35: Normalized nonlinear out of plane bending moment across wingspan.	105
Figure 36: Normalized nonlinear out of plane shear force across wingspan.	106
Figure 37: Normalized nonlinear torsional moment across wingspan.	106
Figure 38: Normalized linear out of plane bending moment across wingspan.	107
Figure 39: Normalized linear out of plane shear force across wingspan.	108
Figure 40: Normalized linear torsional bending moment across wingspan.	108
Figure 41: Variation of angle of attack, $\alpha_{aoa}$ , with wing stiffness	109
Figure 42: Variation of elevator deflection, $\delta_{elev}$ , with wing stiffness.	110
Figure 43: Variation of aileron deflection, $\delta_{ail}$ , with wing stiffness	110

Figure 44: Dimensioning of thin-walled beam used to parametrize wing elements.....	115
Figure 45: Variation of the in-plane stiffness, torsional stiffness, and element mass, as a function of out of plane stiffness .....	116
Figure 46: Normalized out of plane bending moment during dynamic gust simulation	129
Figure 47: Variation in the positive peak gust load vs wing stiffness, <b>I11</b> .....	130
Figure 48: Variation in the negative peak gust load vs wing stiffness, <b>I11</b> .....	130
Figure 49: Wing-Fuselage attachment .....	132
Figure 50: Variation in the positive peak gust load as the aerodynamic centre is moved forward and aft.....	132
Figure 51: Variation in the negative peak gust load as the aerodynamic centre is moved forward and aft.....	133
Figure 52: Tail-Fuselage attachment .....	134
Figure 53: Variation in the positive peak gust load as the tail aerodynamic centre is moved forward and aft.....	134
Figure 54: Variation in the negative peak gust load as the tail aerodynamic centre is moved forward and aft.....	135
Figure 55: Engine C.G. shift.....	135
Figure 56: Variation in the positive peak gust load as the engine centre of mass is moved longitudinally .....	136
Figure 57: Variation in the negative peak gust load as the engine centre of mass is moved longitudinally .....	136
Figure 58: Variation in the positive peak gust load as the engine centre of mass is moved laterally .....	137

Figure 59: Variation in the negative peak gust load as the engine centre of mass is moved laterally .....	137
Figure 60: Variation in the positive peak gust load as the engine mass is varied by $\pm 5\%$ .....	138
Figure 61: Variation in the negative peak gust load as the engine mass is varied by $\pm 5\%$ .....	138
Figure 62: Sensitivity of nonlinear loads to variations in out of plane stiffness.....	140
Figure 63: Sensitivity of nonlinear loads to variations in wing positioning .....	141
Figure 64: Sensitivity of nonlinear loads to variations in tail positioning.....	142
Figure 65: Sensitivity of nonlinear loads to variations in engine longitudinal position .	143
Figure 66: Sensitivity of nonlinear loads to variations in engine lateral position .....	143
Figure 67: Sensitivity of nonlinear loads to variations in engine mass changes .....	144
Figure 68: Sensitivity of nonlinear bending peak loads to variations of design parameters .....	144

## List of Tables

Table 1: Structural properties of cantilever beam.....	62
Table 2: Comparison of tip displacement and root bending moment for static loading conditions.....	66
Table 3: Comparison of tip displacement and root bending moment for dynamic loading conditions.....	66
Table 4: Steady flight conditions used.....	87
Table 5: Parameters being studied for the sensitivity analyses.....	126

# 1 Introduction

## 1.1 Background

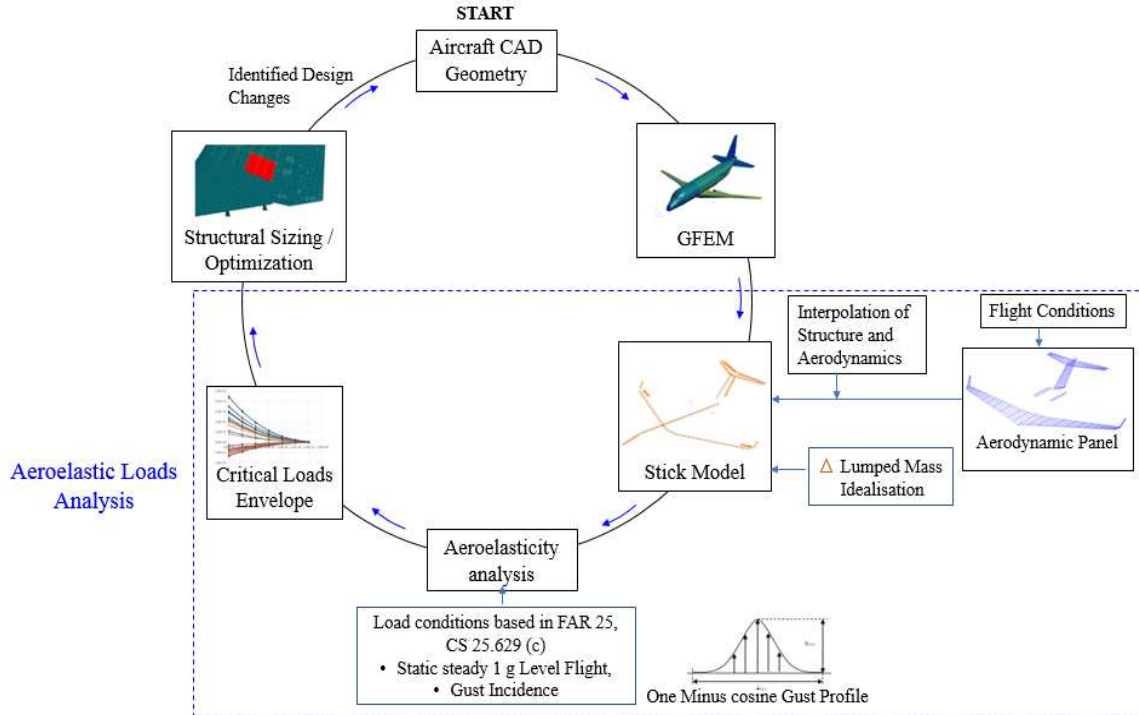


Figure 1: Aeroelastic load calculation process

A critical stage in the certification and approval of a new or modified aircraft design is the loads calculation process, shown in Figure 1, also referred to as “loops”. The process begins with the Global Finite Element Model, or GFEM of the aircraft, which is reduced to a 1D beam equivalent model. The aircraft model is then subject to a large number of flight simulations, encompassing the entire flight envelope, and the largest loads for each aircraft component, such as the wing, fuselage, tail, etc. is condensed into a critical load envelope. The loads envelope represents the absolute worst case loads that can be encountered by the aircraft. These loads are then applied on the GFEM model to optimize the structure, removing material where unnecessary, and strengthening certain locations if

the loads exceed manufacturer/platform specific allowable limits. The now modified GFEM structure is then reduced to a stick model and the “loop” process is repeated until the aircraft design meets regulatory and certification requirements.

## **1.2 Motivation**

Minimizing aircraft weight to maximize its fuel efficiency and performance is among the major design objectives in new aircraft development programs [2]. The general trend towards increasing the fuel efficiency of the aircraft has led to the shift towards higher aspect ratio wings due to their significant effect on induced drag [3]. As induced drag is a large part of the total drag, reducing it can have substantial effects on fuel economy [4]. Both design trends have the effect of increasing the deformation of the aircraft wing under loading. Weight minimization leads to reduced torsional and bending stiffness, which in turn lead to increased wing deflections under loading. Similarly, increasing the aspect ratio of a wing results in a higher slenderness ratio which upturns the wing deflection. Large airframe deflections result in significant changes in its geometry under loading resulting in a nonlinear behaviour. Such nonlinear effects can have major effects on the aeroelastic behaviour of the aircraft, which has been covered by a number of survey and review papers [5], [6]. In addition to the effects on static loads, the use of geometrically nonlinear structural formulations can lead to significant changes in the response of aircraft to dynamic loading conditions [7], [8].

An unintended consequence of such behavior is that it moves away from what is expected from a typical linear structural model. As such, the effects of geometric nonlinearities have to be considered during the loads “loop” process especially in the aeroelastic analysis of aircraft, to obtain higher fidelity loads and better model its response under large

deformations. Therefore, the effects of geometric nonlinearity needs to be included in any high fidelity aeroelastic solution sequence [9].

### **1.3 Literature Review**

#### **1.3.1 Modeling of geometric nonlinearities**

Four methodologies for the modelling of geometrical nonlinearities in structural analyses are reviewed in this section, namely, the displacement-based methods, the geometrically exact intrinsic beams methods, the strain-based methods and the modal methods. Since one dimensional stick models [10]–[18] are a common approach for the structural representation in aeroelasticity analyses within the aerospace industries, the focus of attention in this thesis is on nonlinear beam formulations.

##### ***1.3.1.1 Displacement based methods***

The most commonly used formulation for the modeling of geometrically nonlinear effects in structural analysis is the displacement-based method. This methodology is also widely employed in commercial finite element codes such as MSC Nastran [19], ANSYS [20], [21], ADINA [22], [23], among others [24]. Example of such implementation includes the nonlinear composite beam theory by Bauchau and Hong [25], [26]. Since the independent variables are the rotation and the displacement, visualization and application of the constraints is straight forward. However, the presence of higher order nonlinear terms in the deformation field makes the displacement-based formulations computationally expensive, requiring more time and resources to solve [27].

### *1.3.1.2 Strain based formulation*

Strain based formulations represent the beam deformations using variable derivatives of the standard displacement-based method; namely extensional, shear, twist, and curvature, as opposed to displacements and rotations [28]. These formulations have the advantage of avoiding shear locking phenomenon due to spurious strain energy, as well as accurate representations of rigid body modes [29]. In the strain based methodology, stress resultants, such as internal beam forces and moments, can be directly obtained from the strain degrees of freedom without additional numerical differentiation of displacement variable, while maintaining the same level of accuracy as obtained for the independent strain degrees of freedom [30]. One of the first strain-based formulations applied for geometrically nonlinear analyses was developed by Eric Brown for the aeroelastic analysis of highly flexible composite wings [31]. Here, the equations for the nonlinear beam models by Patil [32] and Hodges [33] were reformulated using strains as the independent variables. The methodology was further improved by Shearer [34] and Su [35] by rewriting the iterative equations in closed form solution, and by including the ability to add arbitrary nodal point constraints, respectively, resulting in a formulation that allows for arbitrary aircraft configurations, such as strut-braced or joined-wing type aircraft [27].

### *1.3.1.3 Modal methods*

The cost of direct integration of finite element equations is often directly proportional to the size of the system. While the method of modal superposition, where the system is reduced from the size of the entire physical system to a select number of modes, is very common in linear dynamic response analysis [36]–[38], a key difference with nonlinear analyses is that the stiffness matrix, and thus, the mode shapes and natural

frequencies, are often dependant on the applied load and current state of deformation. On the other hand, Bathe showed that even the eigenvectors and eigenvalues derived from a linear modal decomposition can be used to accurately model the effect of nonlinearities using an iterative solution methodology [23], [24].

#### *1.3.1.4 Geometrically Exact Intrinsic Beam*

The foundation for the exact equilibrium equations for thin beams under deformation was initially proposed by Love, in the Treatise on Mathematical Theory of Elasticity [39], which considered beams bending, rotation, and elongation. This work was expanded upon by Reissner, to include the effects of shear forces and deformations, to become the first “geometrically exact” intrinsic beam theory [40]. The term intrinsic is used to indicate that the equations are formulated in terms of virtual displacements and rotations, and therefore are not restricted to a particular choice of displacement or rotation parameter [41]. The work was further extended by Hegemier and Nair to formulate a small strain, large deformation theory for untwisted isotropic rods in extension, torsion, and twist [42]. The work done by Hodges built upon prior work, extending the formulation for initially curved and twisted beams with capabilities for anisotropic material models [43]. Due to the “intrinsic” nature of the formulation, the singularities associated with common choices of rotation parameter were not present in the formulations [44]. The “intrinsic” nature also has led to formulations with second order nonlinearities, resulting in a computationally efficient solution of calculations [6], [33]. In addition, it is found that mixed variational formulations potentially can have higher solution accuracy and robustness than displacement-based formulations [45]. For structures that are better

represented as plates than beams, a formulation for moving anisotropic plates is presented by Hodges, et.al. [46].

### 1.3.2 Nonlinear aeroelastic modeling strategies

The static and dynamic behaviour of highly flexible aircraft has been investigated using a wide variety of methods, ranging from approximations, to fully nonlinear solvers with coupled aerodynamics [47], [48]. Modal methods have been used to model the behaviour of High-Altitude Long Endurance (HALE) type aircrafts, using selected rigid body and vibration modes to model their response. However, such methods did not include the effect of geometric nonlinearities due to the inevitable large deformations present along the wingspan [49]. Later work to include geometrically nonlinear effects was conducted, including the work by Patil et al., using the geometrically exact mixed variation formulation to investigate the flutter behaviour of aircraft [50]. Strain based methodologies have been used in the structural formulation of the nonlinear solver UM/NAST [48]. Displacement based nonlinear beam formulations were used in the development of ASWING at MIT, to solve static and dynamic aeroelasticity problems [47]. However, the clear limitation of the methods discussed prior is their purpose-built nature. These codes were developed without industry usage in mind, and as such cannot be applied to a commercial aerospace environment without significant changes to existing industry standard aircraft loads calculation processes.

## 1.4 Thesis Objective

In this thesis, the effect of geometric nonlinearities on static and dynamic aeroelastic flight loads is studied at length. The main objective of the first half of the thesis is to present a nonlinear static aeroelastic method to improve the fidelity of aircraft loads to be used in

the aircraft design process. An iterative methodology is presented to calculate flight loads in static aeroelastic conditions by considering effects of geometric nonlinearity on the structure. The method, named the “modified iterative method”, allows the calculation of higher fidelity aeroelastic loads using a geometrically nonlinear beam formulation. The proposed method is validated using an external nonlinear aeroelastic solver, ASWING, and shows excellent agreement between the two. A case study using a Bombardier aircraft platform is presented, and the results detail the significant differences in wing loading due to large displacement effects.

The latter half of the thesis focuses on loads prediction during the conceptual design stage of a new aircraft, with consideration of geometrically nonlinear effects. During a conceptual design stage, several aircraft configurations will be investigated against design criteria. To emulate this scenario, key aircraft design parameters are varied, and a sensitivity analysis is performed on the load increment due to nonlinear effects. Results of the study indicate a highly nonlinear relationship between aircraft wing flexibility and peak gust loads. The objective of this work is to allow designers to determine which conceptual design changes require a geometrically nonlinear solver, and which changes can be estimated by a linear solver.

## **1.5 Thesis Outline**

The work completed towards the thesis is presented in seven chapters. The second chapter reviews the mathematical bases for four geometrically nonlinear beam modeling theories. The third chapter presents the results of a case study where a highly flexible beam model was implemented with each of the four nonlinear beam models from the previous chapter are compared. Chapter four describes the proposed modified iterative method to

implement a geometrically nonlinear static aeroelastic solution method using existing commercial solvers, validated with a custom nonlinear solver. Chapter five details the methodology of studying the gust loads when aircraft design parameters are varied rapidly, such as in a preliminary design study. Chapter six presents the results of the sensitivity analysis from the prior Chapter, discussing the sensitivities of the aircraft peak gust loads to variations in wing stiffness, aerodynamic loading, and engine properties. Chapter seven concludes the thesis, discussing the key findings, as well as proposing further avenues of exploration as future work.

## **1.6 Thesis Contribution**

In the first half of the thesis, a geometrically static aeroelastic solution method is presented, significantly improving upon the fidelity of loads compared to the work presented in literature [9]. The major advantage of the work presented over existing nonlinear aeroelastic solvers is the accessibility to engineers working in the aerospace industry. The proposed method remains within the MSC Nastran environment, allowing for easy implementation within any aircraft manufacturer's aeroelastic loads design loop.

The results of the sensitivity analysis performed in the latter half of the thesis allow the prediction of the effect of geometric nonlinearity on the dynamic loads experienced by an airframe. This is especially useful to designers during the conceptual design stage where key aircraft design parameters will change quite rapidly. The results allow the designer to differentiate between critical design parameters which require a nonlinear aeroelastic solver across the design space, and non-critical parameters which can be estimated based on a linear gradient based approach.

In addition, the work presented allows manufacturers to determine the extent of structural changes that can be performed on an airframe before geometrically nonlinear effects have to be considered to maintain aircraft platform specific accuracy thresholds.

## 2 Review of Nonlinear Beam Models

The primary objective of this Chapter is to review geometrically nonlinear beam formulations which include effects of geometric nonlinearity in static and dynamic loading conditions. As such, the derivation of the beam theories presented in this chapter allow for the resultant elemental beam loads calculated to capture effects of geometric nonlinearities.

### 2.1 Displacement Based Method

In this section, the two node beam element is used, based on the co-rotational beam element, with a modified strain measure, proposed to alleviate effects of membrane locking [51]–[53], which is an artificial stiffening effect in curved beam elements in a state of pure bending [54].

For a beam element in the  $x - y$  plane, the degrees of freedom at each end are two in-plane translations, and one in-plane rotation. Thus, the deformation degrees of freedom vector for an element,  $\mathbf{U}_{G,elem}$ , in the global coordinate system is given as:

$$\mathbf{U}_{G,elem} = [u_1 \quad v_1 \quad \theta_1 \quad u_2 \quad v_2 \quad \theta_2] \quad (1)$$

where  $u, v$ , and  $\theta$  are the deformations in the  $x$  and  $y$  directions, and the rotation about the  $z$ -axis, respectively. The subscripts 1 and 2 are beam end nodal identification numbers.

Figure 2 displays the beam in its original and deformed configuration, along with the displacements and rotations in the global and the element local coordinate systems.

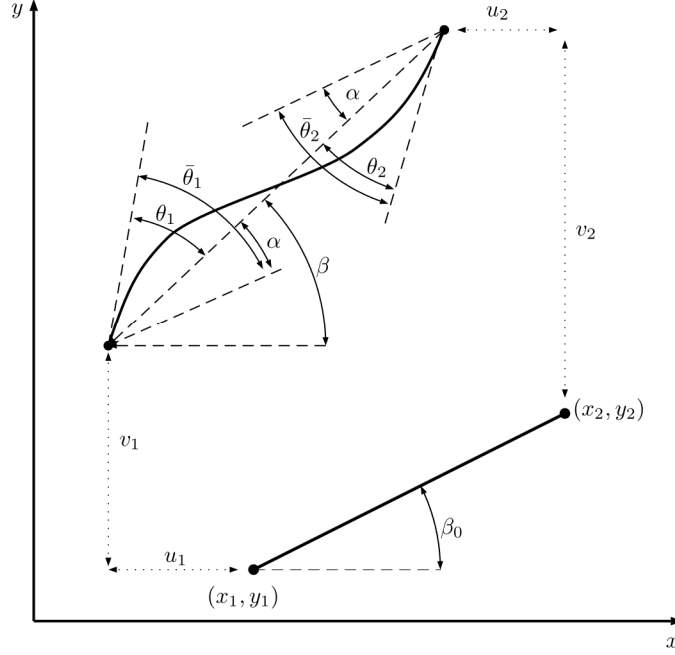


Figure 2: Beam element in global coordinate system [52]

The local element deformations and rotations are given by:

$$\begin{aligned}
 \bar{u} &= L_f - L_o \\
 \bar{\theta}_1 &= \theta_1 - \alpha \\
 \bar{\theta}_2 &= \theta_2 - \alpha
 \end{aligned} \tag{2}$$

where  $L_f$  and  $L_o$  are the element current and initial lengths, respectively.  $\bar{\theta}_1$  and  $\bar{\theta}_2$  are the nodal rotations, while  $\alpha$  is the elemental rigid body rotation.

The elemental lengths can then be obtained from the global displacement vector shown in Equation 1 as:

$$\begin{aligned}
 L_f &= \sqrt{(x_2 + u_2 - x_1 - u_1)^2 + (y_2 + v_2 - y_1 - v_1)^2} \\
 L_o &= \sqrt{(x_2 - x_1)^2 + (y_2 - y_1)^2}
 \end{aligned} \tag{3}$$

The rigid body rotation of the element is defined as:

$$\sin \alpha = \underline{c}_0 \underline{s} - \underline{s}_0 \underline{c} \quad (4)$$

$$\cos \alpha = \underline{c}_0 \underline{c} + \underline{s}_0 \underline{s}$$

where the individual sines,  $s$ , and cosines,  $c$ , are dependent on the rigid body orientation shown in Figure 2.

$$\begin{aligned} \underline{c}_0 &= \cos \beta_0 = \frac{x_2 - x_1}{L_o} \\ \underline{s}_0 &= \sin \beta_0 = \frac{y_2 - y_1}{L_o} \\ \underline{c} &= \cos \beta = \frac{x_2 + u_2 - x_1 - u_1}{L_f} \\ \underline{s} &= \sin \beta = \frac{y_2 + v_2 - y_1 - v_1}{L_f} \end{aligned} \quad (5)$$

The shape functions used are based on those classically employed in Euler-Bernoulli beam theory, namely linear shape function for axial displacement, and a cubic shape function for transverse displacement [24], [51], [52].

The deformation along the beam can then be written by the following geometric relationships

$$\begin{aligned} \hat{u} &= \frac{x}{L_o} \bar{u} \\ \hat{v} &= \hat{x} \left(1 - \frac{\hat{x}}{L_o}\right)^2 \bar{\theta}_1 + \frac{\hat{x}^2}{L_o} \left(\frac{\hat{x}}{L_o} - 1\right) \bar{\theta}_2 \end{aligned} \quad (6)$$

where  $\hat{x}$  is the physical distance along an element,  $\hat{y}$  is the distance from the neutral axis, and  $\hat{u}$ ,  $\hat{v}$  are the corresponding deformations at a distance  $\hat{x}$  along the beam element. As per the Euler-Bernoulli assumptions, the curvature of the beam,  $\kappa$ , is defined as:

$$\kappa = \frac{\partial^2 \hat{v}}{\partial \hat{x}^2} = \left( \frac{6\hat{x}}{L_o^2} - \frac{4}{L_o} \right) \bar{\theta}_1 + \left( \frac{6\hat{x}}{L_o^2} - \frac{2}{L_o} \right) \bar{\theta}_2 \quad (7)$$

The strain measure is taken to be an average measure as defined in the work by Battini [52] to avoid the issues associated with membrane locking present in  $C^1$  continuity elements such as the Euler-Bernoulli beam element [55]. The  $C^1$  continuity refers to the fact that the first derivative of the shape functions required for the strain calculations are continuous across element boundaries [56].

This modified strain measure is given as follows:

$$\varepsilon = \varepsilon_f - \kappa \hat{y} = \frac{1}{L_o} \int_{L_o} \left[ \frac{\partial \hat{u}}{\partial \hat{x}} + \frac{1}{2} \left( \frac{\partial \hat{v}}{\partial \hat{x}} \right)^2 \right] d\hat{x} - \kappa \hat{y} \quad (8)$$

Substituting Equations 6 and 7 into Equation 8, an expression is obtained for the strain at any point  $x, y$  within the beam element as:

$$\varepsilon = \frac{\bar{u}}{L_o} + \frac{1}{15} \left( \bar{\theta}_1^2 - \frac{\bar{\theta}_1 \bar{\theta}_2}{2} + \bar{\theta}_2^2 \right) + \frac{\hat{y}}{L_o} \left( (4 - 6\xi) \bar{\theta}_1 + (2 - 6\xi) \bar{\theta}_2 \right) \quad (9)$$

where the elemental natural coordinate,  $\xi$ , is used to denote a normalized distance along the element, which is given by:

$$\xi = \frac{\hat{x}}{L_o} \quad (10)$$

To obtain the equations of the system, the principle of virtual work is used to relate the virtual work due to elemental deformations in the local coordinate system to the virtual work due to deformations in the global coordinate system, resulting in the following expression for the incremental virtual work as:

$$\delta W_{elem} = \delta \mathbf{U}_{G,elem}^T \mathbf{F}_{G,elem} = \delta \mathbf{U}_L^T \mathbf{F}_L = \delta \mathbf{U}_{G,elem}^T \mathbf{B}^T \mathbf{F}_L \quad (11)$$

$\mathbf{U}_{G,elem}$  and  $\mathbf{U}_L$  refer to the elemental displacement vector in the global and local coordinate systems and relate to each other with a currently unknown matrix  $\mathbf{B}$ .

$$\delta\mathbf{U}_L = \mathbf{B}\delta\mathbf{U}_{G,elem} \quad (12)$$

Differentiating Equation 2, the following expression for the virtual local displacement is obtained

$$\delta\bar{u} = \delta L_f - \delta L_o = \delta L_f \quad (13)$$

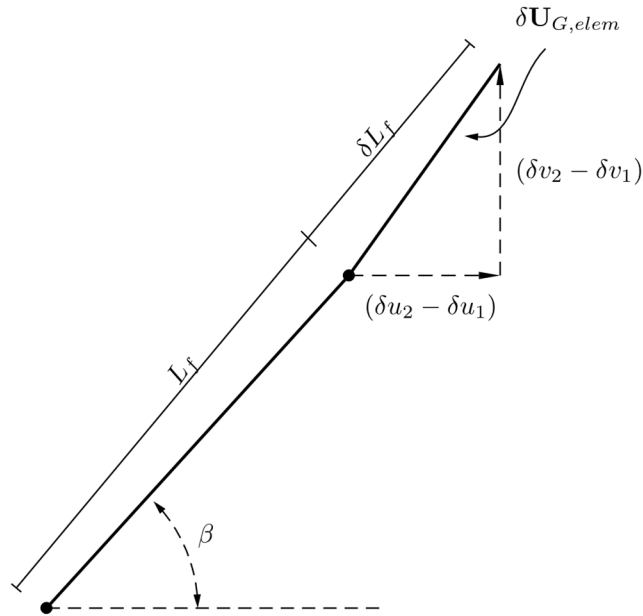


Figure 3: An infinitesimal increment to the displacement

Figure 3 shows the geometric relationship between the beam orientation angle,  $\beta$ , and the variation in elemental displacement,  $\delta L_f$ . This variation can be evaluated geometrically given the assumption of  $\delta\mathbf{U}_{G,elem}$  being a small infinitesimal displacement at the end of the element as:

$$\delta\bar{u} = \underbrace{\frac{x_2 + u_2 - x_1 - u_1}{L_f}}_{\cos \beta} (\delta u_2 - \delta u_1) + \underbrace{\frac{y_2 + v_2 - y_1 - v_1}{L_f}}_{\sin \beta} (\delta v_2 - \delta v_1) \quad (14)$$

Taking an increment in Equation 2, and given  $\alpha = \beta - \beta_0$ , the following expressions relating the variation in local displacements to the corresponding global values is obtained as:

$$\begin{aligned}\delta\bar{\theta}_1 &= \delta\theta_1 - \delta\alpha = \delta\theta_1 - \delta\beta \\ \delta\bar{\theta}_2 &= \delta\theta_2 - \delta\alpha = \delta\theta_2 - \delta\beta\end{aligned}\quad (15)$$

Differentiating the last expressions of Equation 5 results in

$$\begin{aligned}\delta(\sin \beta) &= \delta\left(\frac{y_2 + v_2 - y_1 - v_1}{L_f}\right) \\ \delta\beta \cos \beta &= \delta\left(\frac{1}{L_f}\right)(y_2 + v_2 - y_1 - v_1) + \frac{1}{L_f}\delta(y_2 + v_2 - y_1 - v_1)\end{aligned}\quad (16)$$

Rearranging Equation 16, an expression for the variation of the beam orientation angle,  $\beta$  is obtained:

$$\delta\beta = \frac{1}{L_f^2 \cos \beta} \left( (\delta v_2 - \delta v_1)L_f - \delta L_f(y_2 + v_2 - y_1 - v_1) \right) \quad (17)$$

Using Equation 17, the final expression for the variation in elemental rigid body rotation is obtained as:

$$\delta\beta = \frac{1}{\underline{c}L_f} \left( (\delta v_2 - \delta v_1) - \underline{c}s(\delta u_2 - \delta u_1) - \underline{s}^2(\delta v_2 - \delta v_1) \right) \quad (18)$$

Equations 14 and 18 can be arranged in matrix format as:

$$\begin{Bmatrix} \delta\bar{u} \\ \delta\bar{\theta}_1 \\ \delta\bar{\theta}_2 \end{Bmatrix} = \mathbf{B} \begin{Bmatrix} \delta u_1 \\ \delta v_1 \\ \delta\theta_1 \\ \delta u_1 \\ \delta v_1 \\ \delta\theta_2 \end{Bmatrix} \quad (19)$$

where

$$\mathbf{B} = \begin{bmatrix} -\cos \beta & -\sin \beta & 0 & \cos \beta & \sin \beta & 0 \\ -\sin \beta & \cos \beta & 1 & \sin \beta & -\cos \beta & 0 \\ \frac{-\sin \beta}{L_f} & \frac{\cos \beta}{L_f} & 0 & \frac{\sin \beta}{L_f} & \frac{-\cos \beta}{L_f} & 1 \\ -\sin \beta & \cos \beta & 0 & \sin \beta & -\cos \beta & 1 \\ \frac{-\sin \beta}{L_f} & \frac{\cos \beta}{L_f} & 0 & \frac{\sin \beta}{L_f} & \frac{-\cos \beta}{L_f} & 1 \end{bmatrix} \quad (20)$$

The global force contribution due to the internal element force vector from a single element can then be given as:

$$\mathbf{F}_{G,elem} = \mathbf{B}^T \mathbf{F}_L \quad (21)$$

where the elemental virtual work is given by:

$$\delta W_{elem} = \int_V \sigma \delta \varepsilon dV \quad (22)$$

where  $V$  is the volume of the element.

The constitutive model of the beam assumes a linear elastic model, with geometric nonlinearities arising from the nonlinear strain displacement relationship as shown in Equations 8 and 9. Therefore, the stress-strain relationship is as follows:

$$\sigma = E \varepsilon \quad (23)$$

where  $\sigma$  is the elemental stress, and  $E$  is the Young's modulus of the material.

To compute the integral from Equation 22, the variational derivative of Equation 9 is taken as:

$$\begin{aligned} \delta \varepsilon = & \frac{\delta \bar{u}}{L_o} + \frac{1}{30} (4\bar{\theta}_1 \delta \bar{\theta}_1 - \bar{\theta}_1 \delta \bar{\theta}_2 - \bar{\theta}_2 \delta \bar{\theta}_1 + 4\bar{\theta}_2 \delta \bar{\theta}_2) \\ & + \frac{\hat{y}}{L_o} \left( (4 - 6\xi) \delta \bar{\theta}_1 + (2 - 6\xi) \delta \bar{\theta}_2 \right) \end{aligned} \quad (24)$$

Substituting Equations 23 and 24 into Equation 22 and numerically integrated, a relationship for the beam internal moments and forces is obtained as:

$$\delta W_{elem} = N\delta\bar{u} + M_1\delta\bar{\theta}_1 + M_2\delta\bar{\theta}_2 \quad (25)$$

where

$$N = EA \left( \frac{\bar{u}}{L_o} + \frac{1}{15} \left( \bar{\theta}_1^2 - \frac{\bar{\theta}_1\bar{\theta}_2}{2} + \bar{\theta}_2^2 \right) \right) \quad (26)$$

$$M_1 = EAL_o \left( \frac{\bar{u}}{L_o} + \frac{1}{15} \left( \bar{\theta}_1^2 - \frac{\bar{\theta}_1\bar{\theta}_2}{2} + \bar{\theta}_2^2 \right) \right) \left( \frac{2}{15}\bar{\theta}_1 - \frac{1}{30}\bar{\theta}_2 \right) + \frac{EI}{L_o} (4\bar{\theta}_1 + 2\bar{\theta}_2) \quad (27)$$

$$M_2 = EAL_o \left( \frac{\bar{u}}{L_o} + \frac{1}{15} \left( \bar{\theta}_1^2 - \frac{\bar{\theta}_1\bar{\theta}_2}{2} + \bar{\theta}_2^2 \right) \right) \left( \frac{2}{15}\bar{\theta}_2 - \frac{1}{30}\bar{\theta}_1 \right) + \frac{EI}{L_o} (4\bar{\theta}_2 + 2\bar{\theta}_1) \quad (28)$$

The tangent stiffness matrix of a system is defined as the variation of internal force with respect to a variation in displacement as:

$$\begin{aligned} \delta \mathbf{F}_{G,elem} &= \mathbf{K}_{G,elem} \delta \mathbf{U}_{G,elem} = \delta \mathbf{U}_L \\ &= \mathbf{B}^T \delta \mathbf{F}_L + N \delta \mathbf{B}_1 + M_1 \delta \mathbf{B}_2 + M_2 \delta \mathbf{B}_3 \end{aligned} \quad (29)$$

where  $\mathbf{b}_i$  are the corresponding columns of  $\mathbf{B}^T$ , for  $i \in \{1,2,3\}$ .

To evaluate their variation, vectors  $\mathbf{r}$  and  $\mathbf{q}$  are defined as follows:

$$\begin{aligned} \mathbf{r} &= [-\cos \beta \quad -\sin \beta \quad 0 \quad \cos \beta \quad \sin \beta \quad 0]^T \\ \mathbf{q} &= [\sin \beta \quad -\cos \beta \quad 0 \quad -\sin \beta \quad \cos \beta \quad 0]^T \end{aligned} \quad (30)$$

and their variations are given as:

$$\begin{aligned}\delta \mathbf{r} &= \mathbf{q} \delta \beta \\ \delta \mathbf{q} &= -\mathbf{r} \delta \beta\end{aligned}\tag{31}$$

Resulting in the following expressions for  $\mathbf{b}_1$ ,  $\mathbf{b}_2$ , and  $\mathbf{b}_3$

$$\begin{aligned}\mathbf{b}_1 &= \mathbf{r} \\ \mathbf{b}_2 &= [0 \ 0 \ 1 \ 0 \ 0 \ 0]^T - \frac{1}{L_f} \mathbf{q} \\ \mathbf{b}_3 &= [0 \ 0 \ 1 \ 0 \ 0 \ 1]^T - \frac{1}{L_f} \mathbf{q}\end{aligned}\tag{32}$$

The corresponding variations for  $\delta \mathbf{b}_i$  are given as:

$$\begin{aligned}\delta \mathbf{b}_1 &= \delta \mathbf{r} = \frac{\mathbf{q} \mathbf{q}^T}{L_f} \delta \mathbf{U}_G \\ \delta \mathbf{b}_2 &= \delta \mathbf{b}_3 = \frac{\mathbf{q} \delta L_f}{L_f^2} - \frac{\delta \mathbf{q}}{L_f}\end{aligned}\tag{33}$$

and  $\delta \mathbf{F}_L$  is given by:

$$\delta \mathbf{F}_L = \mathbf{K}_L \delta \mathbf{U}_L\tag{34}$$

where the components of  $\mathbf{K}_L$  are obtained by differentiating the expressions for  $N$ ,  $M_1$  and  $M_2$  with respect to  $\bar{u}$ ,  $\bar{\theta}_1$  and  $\bar{\theta}_2$ .

The elemental tangent stiffness matrix is then given as:

$$\mathbf{K}_L = \begin{bmatrix} K_{l_{11}} & K_{l_{12}} & K_{l_{13}} \\ K_{l_{21}} & K_{l_{22}} & K_{l_{23}} \\ K_{l_{31}} & K_{l_{32}} & K_{l_{33}} \end{bmatrix}\tag{35}$$

where the individual components of the stiffness matrix are given as follows:

$$\begin{aligned}
K_{l_{11}} &= \frac{\partial N}{\partial \bar{u}} = \frac{EA}{L_o} \\
K_{l_{12}} &= \frac{\partial N}{\partial \bar{\theta}_1} = EA \left( \frac{2}{15} \bar{\theta}_1 - \frac{1}{30} \bar{\theta}_2 \right) \\
K_{l_{13}} &= \frac{\partial N}{\partial \bar{\theta}_2} = EA \left( \frac{2}{15} \bar{\theta}_2 - \frac{1}{30} \bar{\theta}_1 \right) \\
K_{l_{22}} &= \frac{\partial M_1}{\partial \bar{\theta}_1} = EAL_o \left( \frac{2}{15} \bar{\theta}_1 - \frac{1}{30} \bar{\theta}_2 \right)^2 + \frac{4EI}{L_o} \\
&\quad + \frac{2}{15} EAL_o \left( \frac{\bar{u}}{L_o} + \frac{1}{15} \left( \bar{\theta}_1^2 - \frac{\bar{\theta}_1 \bar{\theta}_2}{2} + \bar{\theta}_2^2 \right) \right) \\
K_{l_{23}} &= \frac{\partial M_1}{\partial \bar{\theta}_2} = EAL_o \left( \frac{2}{15} \bar{\theta}_2 - \frac{1}{30} \bar{\theta}_1 \right) \left( \frac{2}{15} \bar{\theta}_1 - \frac{1}{30} \bar{\theta}_2 \right) + \frac{2EI}{L_o} \\
&\quad - \frac{1}{30} EAL_o \left( \frac{\bar{u}}{L_o} + \frac{1}{15} \left( \bar{\theta}_1^2 - \frac{\bar{\theta}_1 \bar{\theta}_2}{2} + \bar{\theta}_2^2 \right) \right) \\
K_{l_{33}} &= \frac{\partial M_2}{\partial \bar{\theta}_2} = EAL_o \left( \frac{2}{15} \bar{\theta}_2 - \frac{1}{30} \bar{\theta}_1 \right)^2 + \frac{4EI}{L_o} \\
&\quad + \frac{2}{15} EAL_o \left( \frac{\bar{u}}{L_o} + \frac{1}{15} \left( \bar{\theta}_1^2 - \frac{\bar{\theta}_1 \bar{\theta}_2}{2} + \bar{\theta}_2^2 \right) \right) \\
K_{l_{12}} &= K_{l_{21}} \quad K_{l_{13}} = K_{l_{31}} \quad K_{l_{23}} = K_{l_{32}}
\end{aligned} \tag{36}$$

and the global tangent stiffness matrix contribution for a single element is given as follows

$$\mathbf{K}_{G,elem} = \underbrace{\mathbf{B}^T \mathbf{K}_L \mathbf{B}}_{\text{"pseudo"-linear}} + \underbrace{\frac{\mathbf{q}\mathbf{q}^T}{L_f} N + \frac{1}{L_f^2} (\mathbf{r}\mathbf{q}^T + \mathbf{q}\mathbf{r}^T)(M_1 + M_2)}_{\text{nonlinear}} \tag{37}$$

One has to note that, in Equation 37, the “pseudo”-linear elemental stiffness matrix, is actually fully linear when the original Euler-Bernoulli’s strain measure, given below, is used.

$$\varepsilon = \frac{\bar{u}}{L_o} + \frac{\hat{y}}{L_o} \left( (4 - 6\xi)\bar{\theta}_1 + (2 - 6\xi)\bar{\theta}_2 \right) \quad (38)$$

However, when the modified strain measure is used, the  $\mathbf{B}^T \mathbf{K}_L \mathbf{B}$  term is no longer linear and is now dependant on the current deformation of the beam.

The elemental stiffness and internal force contributions, given by Equations 37 and 21, are summed for the entire structure, and the following equation is obtained for the static structure at equilibrium.

$$\underbrace{[\mathbf{K}_{glob}] \mathbf{U}}_{\mathbf{F}_{internal}} = \mathbf{R}_{applied} \quad (39)$$

where  $\mathbf{U}$  is the deformation configuration at equilibrium, when the global internal force vector,  $\mathbf{F}_{internal}$ , is equal to the external applied force vector  $\mathbf{R}_{applied}$ . This equation is solved iteratively using the full Newton-Raphson method from Bathe [24]. For a non-follower/deformation independent loading, the iterative expression is written as:

$$\Delta \mathbf{R}^{k-1} = \mathbf{R} - \mathbf{F}_{int}^{k-1} \quad (40)$$

where  $\mathbf{R}$  is the applied load,  $\mathbf{F}_{int}^{k-1}$  is the global internal force vector at iteration  $k - 1$ , and  $\Delta \mathbf{R}^{k-1}$  is the out of balance load on the structure.

$$\mathbf{K}^{k-1} \Delta \mathbf{U}^k = \mathbf{R}^{k-1} \quad (41)$$

where  $\mathbf{K}^{k-1}$  is the tangent stiffness matrix containing the linear and nonlinear stiffnesses, at the previous iteration, and  $\Delta \mathbf{U}^k$  is the deformation due to the out of balance load vector.

$$\mathbf{U}^k = \mathbf{U}^{k-1} + \Delta\mathbf{U}^k \quad (42)$$

Equation 42 is iterated until the displacement between iterations is below a user-defined convergence tolerance.

In the dynamic case, Equation 39 is rewritten to include inertial and damping effects, at time step,  $t + \Delta t$ , as:

$$\mathbf{M}\ddot{\mathbf{U}}_{t+\Delta t} + \mathbf{C}_t^k \dot{\mathbf{U}}_{t+\Delta t} + \mathbf{K}_t \Delta\mathbf{U} = \mathbf{R}_{t+\Delta t} - \mathbf{F}_{int_{t+\Delta t}} \quad (43)$$

where  $\mathbf{M}$  is the mass matrix, and  $\mathbf{C}_t^k$  is the damping matrix which could be time dependant, and (  $\cdot$  ) indicates a time derivative

The choice of mass matrix in a finite element analysis can influence the dynamic loads. In this work, a coupled mass matrix is chosen, which for a 2D beam element, is given as follows [57]:

$$M_{elem} = \frac{mL_o}{420} \begin{bmatrix} 140 & 0 & 0 & 70 & 0 & 0 \\ 0 & 156 & 22L_o & 0 & 54 & -13L_o \\ 0 & 22L_o & 4L_o^2 & 0 & 13L_o & -3L_o^2 \\ 70 & 0 & 0 & 140 & 0 & 0 \\ 0 & 54 & 13L_o & 0 & 156 & -22L_o \\ 0 & -13L_o & -3L_o^2 & 0 & -22L_o & 4L_o^2 \end{bmatrix} \quad (44)$$

where  $m$  is the mass per unit length of the beam. Using the Newmark method of time integration, the time integration scheme is given in the proceeding equations [58].

At each time step, an effective stiffness matrix, consisting of the updated nonlinear stiffness matrix, as well as inertial effects, along with an effective load vector, is calculated as:

$$\mathbf{K}_{eff_t} = \mathbf{K}_t + \hat{a}_0 \mathbf{M} \quad (45)$$

$$\mathbf{R}_{eff_{t+\Delta t}} = \mathbf{R}_{t+\Delta t} + \mathbf{M}(\hat{a}_1 \dot{\mathbf{U}}_t + \hat{a}_2 \ddot{\mathbf{U}}_t) - \mathbf{F}_{int_t} \quad (46)$$

where the subscript  $t$  and  $t + \Delta t$  indicate the quantities at the current and next timesteps.

The following equation is solved for the displacement,  $\mathbf{U}$ :

$$\mathbf{K}_{eff_t} \mathbf{U} = \mathbf{R}_{eff_{t+\Delta t}} \quad (47)$$

and then iteratively solved to obtain the deformation corresponding to the system in dynamic equilibrium. The process is started by initializing  $\mathbf{U} = \mathbf{U}^0$ .

The  $k - 1$  approximation to the displacement, acceleration and effective load are calculated as:

$$\ddot{\mathbf{U}}_{t+\Delta t}^{k-1} = \hat{a}_0 \mathbf{U}^{k-1} - \hat{a}_1 \dot{\mathbf{U}}_t - \hat{a}_2 \ddot{\mathbf{U}}_t \quad (48)$$

$$\mathbf{U}_{t+\Delta t}^{k-1} = \mathbf{U}_t + \mathbf{U}^{k-1} \quad (49)$$

$$\mathbf{R}_{eff_{t+\Delta t}}^{k-1} = \mathbf{R}_{t+\Delta t} - \mathbf{M} \ddot{\mathbf{U}}_{t+\Delta t}^{k-1} - \mathbf{F}_{int_{t+\Delta t}}^{k-1} \quad (50)$$

The incremental displacement is then solved as:

$$\mathbf{K}_{eff_t} \Delta \mathbf{U}^k = \mathbf{R}_{eff_{t+\Delta t}}^{k-1} \quad (51)$$

and the updated displacement is given as:

$$\mathbf{U}^k = \mathbf{U}^{k-1} + \Delta \mathbf{U}^k \quad (52)$$

The above equations are iterated in a loop until the solution is considered converged for the corresponding time step. Following this, the displacement, velocity, and acceleration for the next time step is given as:

$$\mathbf{U}_{t+\Delta t} = \mathbf{U}_t + \mathbf{U}^k \quad (53)$$

$$\ddot{\mathbf{U}}_{t+\Delta t} = \hat{a}_3 \mathbf{U}^k + \hat{a}_4 \dot{\mathbf{U}}_t + \hat{a}_5 \ddot{\mathbf{U}}_t \quad (54)$$

$$\dot{\mathbf{U}}_{t+\Delta t} = \dot{\mathbf{U}}_t + \hat{a}_6 \ddot{\mathbf{U}}_t + \hat{a}_7 \ddot{\mathbf{U}}_{t+\Delta t} \quad (55)$$

The  $\hat{a}_i$  quantities indicate coefficients used in the Newmark method [37] where  $i \in \{1,2,3, \dots, 7\}$ ., and are given as follows:

$$\begin{aligned} \hat{a}_0 = \frac{4}{\Delta t^2} = \hat{a}_3, \quad \hat{a}_1 = \frac{4}{\Delta t} = -\hat{a}_4, \quad \hat{a}_2 = 1 = -\hat{a}_5 \\ \hat{a}_6 = \frac{\Delta t}{2} = \hat{a}_7 \end{aligned} \quad (56)$$

## 2.2 Strain based geometrically nonlinear beam

In the strain-based formulation, the beam deformation is represented by extensional, twisting and bending strains, which are the beam's independent degrees of freedom [28]. The mathematical formulation presented below is based on the works by [31], [34], [35], [59]

The elemental degrees of freedom for the formulation are given by the strain vector,  $\boldsymbol{\varepsilon}$ , shown in Equation (57) which represents the extensional, torsional, out of plane, and in plane bending strains respectively.

$$\boldsymbol{\varepsilon} = \begin{bmatrix} \varepsilon_x \\ \kappa_x \\ \kappa_y \\ \kappa_z \end{bmatrix} \quad (57)$$

where  $\varepsilon_x$  is the beam extensional strain and  $\kappa_x, \kappa_y$ , and  $\kappa_z$  are the twist, out of plane, and in plane curvatures of the beam respectively.

The position and orientation of a node on the beam is given by

$$h(\xi)^T = [p \quad w_x \quad w_y \quad w_z]^T \quad (58)$$

where  $p$  is the vector representing the absolute position of the node, and  $w_x, w_y,$  and  $w_z$  are orientation vectors to define the beam local coordinate system in the global reference frame, and  $\xi$  is an element natural coordinate, denoting the normalized distance along the length of the beam.

The relationship between the displacement and the strain is given by a set of matrix partial differential equations, as shown in Equation (59)

$$\begin{aligned} \frac{\partial}{\partial x} p_w &= (1 + \varepsilon_x) w_x \\ \frac{\partial}{\partial x} w_x &= \kappa_z w_y - \kappa_y w_z \\ \frac{\partial}{\partial x} w_y &= \kappa_x w_z - \kappa_z w_x \\ \frac{\partial}{\partial x} w_z &= \kappa_y w_x - \kappa_x w_y \end{aligned} \quad (59)$$

Which can be represented in a more compact form as:

$$\frac{\partial}{\partial x} h(\xi) = A(\xi) h(\xi) \quad (60)$$

where the matrix,  $A(\xi)$  is given as follows:

$$A(\xi) = \begin{bmatrix} 0 & 1 + \varepsilon_x & 0 & 0 \\ 0 & 0 & \kappa_z & -\kappa_y \\ 0 & -\kappa_z & 0 & \kappa_x \\ 0 & \kappa_y & -\kappa_x & 0 \end{bmatrix} \quad (61)$$

The solution to Equation (59) is given in the form of a matrix exponential, which relates the position vector along the beam  $h(\xi)$  to the position vector of the start of the beam (a boundary condition), as follows:

$$h(\xi) = e^{A(\xi-\xi_0)} h_0 \quad (62)$$

where  $h_0$  is the known position and orientation at the start of the beam, and  $\xi_0$  is the corresponding beam coordinate. Given that the strains are constant over the entire element, the position and orientation of any point along the beam coordinate  $s$  can be obtained, given the current strain in the beam element, using Equation (62). The full derivation of the discrete solution to Equation (62) is available in [31], [34].

Defining the original undeformed length of an element as,  $\Delta\xi$ :

$$\Delta\xi = \xi_{end} - \xi_0 \quad (63)$$

where  $\xi_0$  and  $\xi_{end}$  denote the two ends of an undeformed beam element.

and a matrix  $\bar{G}$ , is defined as:

$$\bar{G} = \frac{\Delta\xi}{2} A \quad (64)$$

The nodal position vectors of an element,  $n$ , can then be defined as:

$$\begin{aligned} h_{n,1} &= h_{n,0} \\ h_{n,2} &= e^{\bar{G}n} h_{n,0} \\ h_{n,3} &= e^{2\bar{G}n} h_{n,0} \end{aligned} \quad (65)$$

The total independent degrees of freedom and their time derivatives are given as follows:

$$\mathbf{q} = \begin{bmatrix} \boldsymbol{\varepsilon} \\ \mathbf{p}_B \\ \boldsymbol{\theta}_B \end{bmatrix}, \quad \dot{\mathbf{q}} = \begin{bmatrix} \dot{\boldsymbol{\varepsilon}} \\ \mathbf{v}_B \\ \boldsymbol{\omega}_B \end{bmatrix} \quad (66)$$

The bolded quantities indicate that the components of the  $\mathbf{q}$  and  $\dot{\mathbf{q}}$  vectors are 4x1 column vectors as well, and  $\boldsymbol{\varepsilon}$  is the element strain vector defined previously in Equation (57).

In the implementation of the formulation in this work, only the strain variable,  $\boldsymbol{\varepsilon}$ , is considered, as the simple case study being examined is a clamped beam, with no rigid body motion or rotation allowed.

The equations of motion for the elastic deformation of the beam is derived using the principle of virtual work.

The location of any point,  $\mathbf{p}$ , along the beam is given by the vector to the body-fixed frame,  $\mathbf{p}_B$ , and the local beam frame,  $\mathbf{p}_w$  as follows:

$$\mathbf{p} = \mathbf{p}_B + \mathbf{p}_w \quad (67)$$

where the vector in the local beam frame is given by the beam position in the local beam frame and the corresponding direction vectors

$$\mathbf{p} = \mathbf{p}_B + xw_x + yw_y + zw_z \quad (68)$$

and  $x, y$ , and  $z$  represent the coordinates of any point along the beam, presented in the beam local reference frame.

To apply the principle of virtual work, the infinitesimal work done by applying a force on a unit volume is given as follows:

$$\delta W = - \underbrace{\delta \mathbf{p}}_{distance} \cdot \underbrace{\mathbf{f} \rho dA d\xi}_{force} \quad (69)$$

The second time derivative of Equation (68) is substituted into Equation (69) and integrated over a single beam nodal cross-section, resulting in the following expression for the internal virtual work, containing both the flexible and rigid body terms.

$$\begin{aligned}
\delta W_{int}(\xi) = & -\delta h^T(\xi) \left( \int_{A(\xi)} \rho \begin{bmatrix} 1 & x & y & z \\ x & x^2 & xy & xz \\ y & yx & y^2 & yz \\ z & zx & zy & z^2 \end{bmatrix} \cdot \begin{bmatrix} \ddot{p}_w(\xi) \\ \dot{w}_x(\xi) \\ \dot{w}_y(\xi) \\ \dot{w}_z(\xi) \end{bmatrix} dA + \right. \\
& \int_{A(\xi)} \rho \begin{bmatrix} 1 & x & y & z \\ x & x^2 & xy & xz \\ y & yx & y^2 & yz \\ z & zx & zy & z^2 \end{bmatrix} \cdot \begin{bmatrix} I \tilde{p}_w^T(\xi) \\ 0 \tilde{w}_x^T(\xi) \\ 0 \tilde{w}_y^T(\xi) \\ 0 \tilde{w}_z^T(\xi) \end{bmatrix} \boldsymbol{\beta} dA + \\
& \int_{A(\xi)} \rho \begin{bmatrix} 1 & x & y & z \\ x & x^2 & xy & xz \\ y & yx & y^2 & yz \\ z & zx & zy & z^2 \end{bmatrix} \cdot \begin{bmatrix} \tilde{\omega}_B & 0 & 0 & 0 \\ 0 & \tilde{\omega}_B & 0 & 0 \\ 0 & 0 & \tilde{\omega}_B & 0 \\ 0 & 0 & 0 & \tilde{\omega}_B \end{bmatrix} \cdot \begin{bmatrix} I \tilde{p}_w^T(\xi) \\ 0 \tilde{w}_x^T(\xi) \\ 0 \tilde{w}_y^T(\xi) \\ 0 \tilde{w}_z^T(\xi) \end{bmatrix} \boldsymbol{\beta} dA + \\
& \left. 2 \int_{A(\xi)} \rho \begin{bmatrix} 1 & x & y & z \\ x & x^2 & xy & xz \\ y & yx & y^2 & yz \\ z & zx & zy & z^2 \end{bmatrix} \cdot \begin{bmatrix} 0 \dot{\tilde{p}}_w^T(\xi) \\ 0 \dot{\tilde{w}}_x^T(\xi) \\ 0 \dot{\tilde{w}}_y^T(\xi) \\ 0 \dot{\tilde{w}}_z^T(\xi) \end{bmatrix} \boldsymbol{\beta} dA \right) \quad (70)
\end{aligned}$$

$$M_{node}(\xi) = \int_{A(\xi)} \rho \begin{bmatrix} 1 & x & y & z \\ x & x^2 & xy & xz \\ y & yx & y^2 & yz \\ z & zx & zy & z^2 \end{bmatrix} dA \quad (71)$$

$$M_{node}(\xi) = \begin{bmatrix} m & mr_x & mr_y & mr_z \\ mr_x & \frac{I_{xx} - I_{yy} + I_{zz}}{2} & I_{xy} & I_{xz} \\ mr_y & I_{yx} & \frac{I_{xx} - I_{yy} + I_{zz}}{2} & I_{yz} \\ mr_z & I_{zx} & I_{zy} & \frac{I_{xx} - I_{yy} + I_{zz}}{2} \end{bmatrix} \quad (72)$$

where  $\boldsymbol{\beta}$  is a vector containing the linear and angular velocities of the beam element. Equation (70) is simplified by excluding the terms containing rigid body terms, resulting in the following simplified equation:

$$\delta W_{int}(\xi) = -\delta \boldsymbol{\varepsilon}^T(\xi) \cdot (J_{h\varepsilon}^T \mathbf{M}(\xi) J_{h\varepsilon} \cdot \ddot{\boldsymbol{\xi}}(\xi) + J_{h\varepsilon}^T \mathbf{M}(\xi) \dot{J}_{h\varepsilon} \cdot \dot{\boldsymbol{\xi}}(\xi)) \quad (73)$$

Following a similar procedure for the internal strain, strain rates, and external applied forces, excluding the rigid body terms, the following expression is obtained for the external virtual work, this time, for the entire element. Note that once again, all terms related to the rigid body motion have been excluded in this work. The full expressions can be found in [31], [34], [35].

$$\begin{aligned} \delta W_{int} + \delta W_{ext} = \\ \delta \boldsymbol{\varepsilon}^T \cdot \left( -J_{h\varepsilon}^T \mathbf{M}_{elem} J_{h\varepsilon} \ddot{\boldsymbol{\xi}} - J_{h\varepsilon}^T \mathbf{M}_{elem} \dot{J}_{h\varepsilon} \dot{\boldsymbol{\xi}} - \mathbf{C}_{elem} \dot{\boldsymbol{\xi}} - \mathbf{K}_{elem} (\boldsymbol{\varepsilon} - \boldsymbol{\varepsilon}_0) \right) + \\ \delta \boldsymbol{\varepsilon}^T \cdot (J_{h\varepsilon}^T \mathbf{B}_{grav} \mathbf{g} + J_{p\varepsilon}^T \mathbf{B}_F \mathbf{F}_{dist} + J_{\theta\varepsilon}^T \mathbf{B}_M \mathbf{M}_{dist} + J_{p\varepsilon}^T \mathbf{F}_{point} + J_{\theta\varepsilon}^T \mathbf{M}_{point}) \end{aligned} \quad (74)$$

where  $\mathbf{M}_{elem}$ ,  $\mathbf{K}_{elem}$ , and  $\mathbf{C}_{elem}$  are the elemental mass, stiffness, and damping matrices respectively.  $\mathbf{B}_{grav}$ ,  $\mathbf{B}_F$ , and  $\mathbf{B}_M$  are matrices relating load vectors for gravity  $\mathbf{g}$ , distributed loads and moments  $\mathbf{F}_{dist}$ ,  $\mathbf{M}_{dist}$ , point loads and moments  $\mathbf{F}_{point}$ ,  $\mathbf{M}_{point}$ , to the strains.

Setting Equation (74) to zero, the complete nonlinear strain-based equations of motion for a beam with no rigid body motion or rotation allowed is obtained. It is re-written below in matrix format.

$$[\mathbf{M}_{ff}]\{\ddot{\boldsymbol{\varepsilon}}\} + [\mathbf{C}_{ff}]\{\dot{\boldsymbol{\varepsilon}}\} + [\mathbf{K}_{ff}]\{\boldsymbol{\varepsilon}\} = \mathbf{R}_f \quad (75)$$

where [ ] indicate matrices and { } indicate column vectors corresponding to the quantity in them, assembled for the entire finite element structure.

$$\begin{aligned} \mathbf{R}_f = & [\mathbf{K}_{ff}]\{\boldsymbol{\varepsilon}_0\} + [J_{h\varepsilon}^T][\mathbf{B}_{grav}]\{g\} + [J_{p\varepsilon}^T][\mathbf{B}_F]\{F_{dist}\} \\ & + [J_{\theta\varepsilon}^T][\mathbf{B}_M]\{M_{dist}\} + [J_{p\varepsilon}^T]\{F_{point}\} + [J_{\theta\varepsilon}^T]\{M_{point}\} \end{aligned} \quad (76)$$

The Jacobian matrices,  $J$ , were derived in the work by Shearer [34] and are given in Appendix A.

### 2.3 Modal superposition method

The modal method presented below uses the eigenvalues and eigenvectors obtained from a linear modal decomposition to solve for a system of equations, using the generalized displacements as degrees of freedom.

The displacements, generally taken to be a function of time, are decomposed into two separate arrays, each of which consist of only the space and time dependency of the physical displacements.

$$\mathbf{U}(t) = \boldsymbol{\Phi}\mathbf{X}(t) \quad (77)$$

The undamped free vibration problem for a system with  $n$  degrees of freedom is considered,

$$\mathbf{M}\ddot{\mathbf{U}} + \mathbf{K}\mathbf{U} = \mathbf{0} \quad (78)$$

and a periodic solution is assumed for the displacement,  $\mathbf{U}$ , as:

$$\mathbf{U} = \Phi \sin(\omega(t - t_0)) \quad (79)$$

Substituting Equation 79 into Equation 78 results in the following expression

$$\mathbf{K}\Phi = \omega^2 \mathbf{M}\Phi \quad (80)$$

Solving for the unknowns  $\Phi$ , and  $\omega$ , an expression is obtained as follows:

$$\mathbf{K}\Phi = \mathbf{M}\Phi\Omega^2 \quad (81)$$

where  $\Phi$  and  $\Omega^2$  are  $n \times n$  square matrices containing the mass normalized eigenvectors and eigenvalues of the system respectively for a system with  $n$  degrees of freedom.  $\mathbf{I}$  is an identity matrix of size  $n \times n$ .

$$\Phi^T \mathbf{K} \Phi = \Omega^2 \quad (82)$$

$$\Phi^T \mathbf{M} \Phi = \mathbf{I}$$

Substituting Equation 77 into Equation 78, with the inclusion of damping terms, the following expression for linear dynamic analysis is obtained:

$$\ddot{\mathbf{X}} + \Phi^T \mathbf{C} \Phi \dot{\mathbf{X}} + \Omega^2 \mathbf{X} = \Phi^T \mathbf{R} \quad (83)$$

where the generalized displacements,  $\mathbf{X}$ , and the applied loads,  $\mathbf{R}$ , are time dependant.

For the nonlinear modal analysis, the above equation is rewritten using the mode shapes from the eigenvalue decomposition of the global tangent stiffness matrix from the nonlinear static analysis, which contains linear and geometrically nonlinear components.

$$\ddot{\mathbf{X}} + \Phi_{NL}^T \mathbf{C} \Phi_{NL} \dot{\mathbf{X}} + \Omega_{NL}^2 \mathbf{X} = \Phi_{NL}^T \mathbf{R} \quad (84)$$

Equation 84 can be solved using a Newmark time integration to obtain the dynamic response of the structure to an applied load  $\mathbf{R}$ , in the same way as was solved in Section 2.1.

## 2.4 Intrinsic Formulation

In the previous methodologies, the formulations were based on a choice of independent variable, namely the displacements and rotations, or strains and curvatures. Intrinsic beam formulations, however, are not based solely upon a specific choice of independent variable [41].

In this section, the mixed variational formulation of the geometrically exact beam theory, is detailed, with the notation following that used in [43], [60].

The intrinsic equations of motion are derived from Hamilton's principle, which is given as follows:

$$\int_{t_1}^{t_2} \int_0^l [\delta(\mathcal{K} - \mathcal{U}) + \overline{\delta W}] dx_1 dt = \overline{\delta \mathcal{A}} \quad (85)$$

where  $t_2 - t_1$  is an arbitrary time,  $l$  is the length of the segment being integrated,  $\mathcal{K}$ ,  $\mathcal{U}$  and  $\overline{\delta W}$  are the kinetic energy, potential energy, and virtual work due to applied loads, per unit length.  $\overline{\delta \mathcal{A}}$  is the virtual action which is the integral of the virtual work, here representing the boundary conditions and the ends of the time interval.

The potential energy density can be represented by the beam stress resultants as:

$$\int_0^l \delta \mathcal{U} dx_1 = \int_0^l \left[ \delta \gamma^T \left( \frac{\delta \mathcal{U}}{\delta \gamma} \right)^T + \delta \kappa^T \left( \frac{\delta \mathcal{U}}{\delta \kappa} \right)^T \right] dx_1 \quad (86)$$

where  $\gamma$  and  $\kappa$  are the beam generalized strains and curvatures,

$$\mathbf{F} = \left( \frac{\delta \mathcal{U}}{\delta \gamma} \right)^T \quad \mathbf{M} = \left( \frac{\delta \mathcal{U}}{\delta \kappa} \right)^T \quad (87)$$

and  $\mathbf{F}$  and  $\mathbf{M}$  are the internal force and moment vectors.

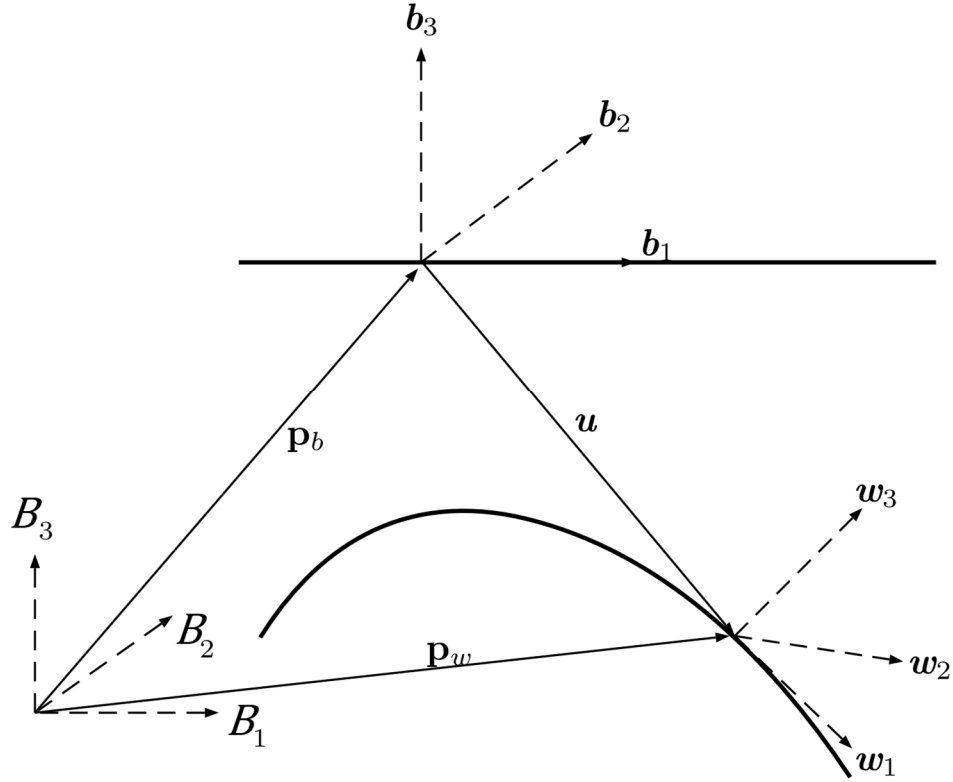


Figure 4: Frames of reference used in the intrinsic beam formulation

For any point along the beam reference line, the relationship between the undeformed reference frame  $\mathbf{b}$  and the deformed reference frame  $\mathbf{w}$ , as shown in Figure 4, is given by the rotation vector  $\underline{\underline{C}}^{wb}$ , where

$$\mathbf{p}_w = \underline{\underline{C}}^{wb} \cdot \mathbf{p}_b \quad (88)$$

The vector definition of the strains and curvature are then defined as follows

$$\begin{aligned} \boldsymbol{\gamma} &= \underline{\underline{C}}^{bw} \mathbf{P}' - \mathbf{p}' \\ \boldsymbol{\kappa} &= \underline{\underline{C}}^{bw} \bar{\boldsymbol{\kappa}} - \boldsymbol{\kappa} \end{aligned} \quad (89)$$

The curvature of the beam due to deformation,  $u$ , can then be given as follows

$$\kappa = \bar{\kappa} \cdot \mathbf{w} - \kappa \cdot \mathbf{b} = \bar{\kappa}_w - \kappa_b \quad (90)$$

where  $C = C^{wb}$  and  $C^T = C^{bw}$ , and  $\bar{\kappa}_w, \kappa_b$  are the deformed and undeformed beam curvatures, respectively. The  $w$  and  $b$  subscripts correspond to the deformed and undeformed beam reference frames. A virtual displacement vector is used to substitute for the physical displacement variation, removing it from the formulation, resulting in the following expression for the potential energy density

$$\begin{aligned} \delta\mathcal{U} &= \delta\gamma^T \mathbf{F} + \delta\kappa^T \mathbf{M} \\ &= \left[ (\overline{\delta q'})^T - \overline{\delta q}^T \widetilde{\kappa}_w - \overline{\delta\psi}^T (\tilde{e}_1 + \tilde{\gamma}) \right] \mathbf{F} \\ &\quad + \left[ (\overline{\delta\psi'})^T - \overline{\delta\psi}^T \widetilde{\kappa}_w \right] \mathbf{M} \end{aligned} \quad (91)$$

where the  $\widetilde{\phantom{x}}$  operator denotes the skew symmetric cross product matrix for a given vector.

Similarly, the variation in the kinetic energy density of the beam can be written as follows

$$\begin{aligned} \delta\mathcal{K} &= \delta\mathbf{v}_w^T \mathbf{P} + \delta\boldsymbol{\omega}_w^T \mathbf{H} \\ &= \left[ (\overline{\delta\dot{q}})^T - \overline{\delta q}^T \widetilde{\boldsymbol{\omega}}_w - \overline{\delta\dot{\psi}}^T \widetilde{\mathbf{v}}_w \right] \mathbf{P} \\ &\quad + \left[ (\overline{\delta\dot{\psi}})^T - \overline{\delta\dot{\psi}}^T \widetilde{\boldsymbol{\omega}}_w \right] \mathbf{H} \end{aligned} \quad (92)$$

where the virtual displacements  $\delta q$  and  $\delta\psi$  are defined as follows

$$\begin{aligned} C\delta u &= \overline{\delta q_w} = \overline{\delta q} \\ \widetilde{\delta\psi} &= -\delta C' C^T \end{aligned} \quad (93)$$

$\mathbf{P}, \mathbf{H}, \mathbf{v}_w$ , and  $\boldsymbol{\omega}$  are the linear momentum, angular momentum, linear velocity, and angular velocity of the beam, respectively.

The virtual work due to applied forces and moments per unit length,  $\check{f}, \check{m}$ , is given as follows

$$\overline{\delta\mathcal{W}} = \int_0^l [\overline{\delta q^T} \check{f} + \overline{\delta\psi^T} \check{m}] dx_1 \quad (94)$$

Substituting Equations 91, 92, and 94 into Equation 85, and integrating by parts with respect to  $t$  and  $x_1$ , the following expression is obtained

$$\begin{aligned} & \int_{t_1}^{t_2} \int_0^l \{ \overline{\delta q^T} (F' + \widetilde{\kappa}_w F - \dot{P} - \widetilde{\omega}_w P + \check{f}) \\ & + \overline{\delta\psi^T} (M' + \widetilde{\kappa}_w M + (\tilde{e}_1 + \tilde{\gamma})F - \dot{H} - \widetilde{v}_w P - \widetilde{\omega}_w H \\ & + m) \} dx_1 dt \\ & = \int_0^l [\overline{\delta q^T} (\hat{P} - P) + \overline{\delta\psi^T} (\hat{H} - H)]_{t_1}^{t_2} dx_1 \\ & - \int_{t_1}^{t_2} [\overline{\delta q^T} (\hat{F} - F) + \overline{\delta\psi^T} (\hat{M} - M)]_0^l dt \end{aligned} \quad (95)$$

The relationship between the velocities and strains to the momenta and internal forces, respectively, are given as follows

$$\begin{aligned} \begin{Bmatrix} P \\ H \end{Bmatrix} &= I \begin{Bmatrix} \mathbf{v}_w \\ \boldsymbol{\omega}_w \end{Bmatrix} \\ \begin{Bmatrix} F \\ M \end{Bmatrix} &= S \begin{Bmatrix} \gamma \\ \kappa \end{Bmatrix} \end{aligned} \quad (96)$$

where the sectional mass matrix is given as

$$\mathbf{M}_{elem} = \begin{bmatrix} m & 0 & 0 & 0 & mr_z & -mr_y \\ 0 & m & 0 & -mr_z & 0 & 0 \\ 0 & 0 & m & mr_y & 0 & 0 \\ 0 & -mr_z & mr_y & i_{22} + i_{33} & 0 & 0 \\ mr_z & 0 & 0 & 0 & i_{22} & -i_{23} \\ -mr_y & 0 & 0 & 0 & -i_{23} & i_{33} \end{bmatrix} \quad (97)$$

where  $m$  is the mass per unit length, and  $r_{x,y,z}$  are the distances from the centre of mass to the centre of the element.

The sectional stiffness matrix can be fully populated, to account for coupling effects between deformation modes in the case of anisotropic materials. In this work, the case study models a simple isotropic beam, and so,  $S$  is given as

$$\mathbf{K}_{elem} = \begin{bmatrix} EA & 0 & 0 & 0 & 0 & 0 \\ 0 & GK_2 & 0 & 0 & 0 & 0 \\ 0 & 0 & GK_3 & 0 & 0 & 0 \\ 0 & 0 & 0 & GJ & 0 & 0 \\ 0 & 0 & 0 & 0 & EI_2 & 0 \\ 0 & 0 & 0 & 0 & 0 & EI_3 \end{bmatrix} \quad (98)$$

where  $GK_2$  and  $GK_3$  are the shear stiffnesses,  $EI_2$  and  $EI_3$  are the bending stiffnesses, and  $EA$  and  $GJ$  are the extensional and torsional stiffnesses.

In the work authored by Wang and Yu. [60], the mixed formulation is derived by using the following kinematical relationships

$$\begin{aligned} u' &= C^{bw}(e_1 + \gamma) - e_1 - \tilde{\kappa}_b u \\ \dot{u} &= C^{bw} \mathbf{v}_w - v - \tilde{\omega} u \end{aligned} \quad (99)$$

$$\begin{aligned} c'_{WM} &= Q_{WM}^{-1}(\kappa + \kappa_b - C^{wb} \kappa_b) \\ c_{\dot{W}M} &= Q_{WM}^{-1}(\omega_w - C^{wb})\omega \end{aligned} \quad (100)$$

where  $\omega$  and  $v$  are the velocities of undeformed reference frame  $\mathbf{b}$  in the inertial/global reference frame, shown in Figure 4,  $c_{WM}$  are the rotation parameters used in the formulation, and  $Q_{WM}$  is defined as follows

$$Q_{WM} = \frac{1}{(4 - c_0)^2} \left[ \left( 4 - \frac{1}{4} c_{WM}^T c_{WM} \right) \Delta - 2\widetilde{c_{WM}} + \frac{1}{2} c_{WM} c_{WM}^T \right] \quad (101)$$

$$Q_{WM}^{-1} = \left( 1 - \frac{1}{16} c_{WM}^T c_{WM} \right) \Delta + \frac{1}{2} \widetilde{c_{WM}} + \frac{1}{8} c_{WM} c_{WM}^T$$

Equations 99, 100, and 101 are substituted into Equation 95 using the method of Lagrange multipliers, and can be written as follows

$$\int_0^l \left\{ \delta u_B'^T F_B + \delta \psi_B'^T M_B \right. \\
+ \overline{\delta \psi}_B^T \left[ \dot{H}_B + \tilde{\omega}_B H_B + \tilde{\mathbf{v}}_B P_B - C^{Bw} (\tilde{e}_1 + \tilde{\gamma}) F_w \right] \\
+ \delta u_B^T (\dot{P}_B + \tilde{\omega}_B P_B) - \overline{\delta F}_B^T [C^{Bw} (e_1 + \gamma) - C^{Bb} e_1] \\
- \overline{\delta F}_B'^T u_B - \overline{\delta M}_B'^T c_{WM_B} - \overline{\delta M}_B^T Q_{WM_B}^{-1} C^{Bb} \kappa \\
+ \overline{\delta P}_B^T (\mathbf{v}_B - v_B - \tilde{\omega}_B u_B - \dot{u}_B) \\
+ \overline{\delta H}_B^T (\boldsymbol{\omega}_w - \omega_w - C^{Bb} Q_{WM_B} c_{\dot{W}M_B}) - \delta u_B^T \check{f}_B \\
\left. - \overline{\delta \psi}_B^T \tilde{m}_B \right\} dx_1 \quad (102)$$

$$= \left[ \delta u_B^T \hat{F}_B + \overline{\delta \psi}_B^T \hat{M}_B - \overline{\delta F}_B^T \hat{u}_B - \overline{\delta M}_B^T \widehat{c_{WM_B}} \right]_0^l$$

Equation 102 represents the total equation of motion, implementing the Geometrically Exact Beam Theory using a mixed formulation, with the displacements and rotations,  $u_B, c_{WM_B}$  taken in the inertial frame,  $B$ , and the body linear and angular forces and momenta,  $F_w, M_w, P_w, H_w$  in the deformed state  $w$ .  $\mathbf{v}_B$  and  $v_B$ , and  $\boldsymbol{\omega}_B$  and  $\omega_B$ , are the

beam velocities (linear and angular) of the deformed and undeformed frames respectively, given in inertial frame  $B$

Linear shape functions are used for  $\delta u_B, \overline{\delta \psi}_B, \overline{\delta F}_B, \overline{\delta M}_B$ , and constant shape functions for  $\overline{\delta P}_B, \overline{\delta H}_B$ . The linear shape function for  $\delta u_B$  is given below as an example

$$\delta u_B = (1 - \xi)\delta u_i + \xi\delta u_{i+1} \quad (103)$$

$$\xi = \frac{x_1 - L_i}{L_{i+1} - L_i} \quad (104)$$

Given a beam with  $N_{elem}$  two noded elements, the equations for the finite element matrices at the starting point of the beam are given as

$$\begin{aligned} \mathbf{Z}_{u_1}^- - F_1^* &= 0 \\ \mathbf{Z}_{\psi_1}^- - M_1^* &= 0 \\ \mathbf{Z}_{F_1}^- - \hat{u}_1^* &= 0 \\ \mathbf{Z}_{M_1}^- - \widehat{c_{WM_1}}^* &= 0 \end{aligned} \quad (105)$$

where (  $*$  ) quantities are the external forces and moments to balance the internal element stress resultants, and (  $_1$  ) subscript indicates the first node.

Similarly, the force moment balance at the end of the beam, node  $N_{elem} + 1$ , is given as

$$\begin{aligned} \mathbf{Z}_{u_{N_{elem}}}^+ - F_{N_{elem}+1}^* &= 0 \\ \mathbf{Z}_{\psi_{N_{elem}}}^+ - M_{N_{elem}+1}^* &= 0 \\ \mathbf{Z}_{F_{N_{elem}}}^+ - \hat{u}_{N_{elem}+1}^* &= 0 \\ \mathbf{Z}_{M_{N_{elem}}}^+ - \hat{c_{WM}_{N_{elem}+1}}^* &= 0 \end{aligned} \quad (106)$$

The force balance for nodes  $i$  to  $N_{elem} - 1$  along the beam is given as

$$\begin{aligned}
\mathbf{Z}_{u_i}^+ + \mathbf{Z}_{u_{i-1}}^- &= 0 \\
\mathbf{Z}_{\psi_i}^+ + \mathbf{Z}_{\psi_{i-1}}^- &= 0 \\
\mathbf{Z}_{F_i}^+ + \mathbf{Z}_{F_{i-1}}^- &= 0 \\
\mathbf{Z}_{M_i}^+ + \mathbf{Z}_{M_{i-1}}^- &= 0
\end{aligned} \tag{107}$$

and the momentum for beam elements  $i$  to  $N_{elem}$  is

$$\begin{aligned}
\mathbf{Z}_{P_i} &= 0 \\
\mathbf{Z}_{H_i} &= 0
\end{aligned} \tag{108}$$

The matrices in the above equations, denoted with  $\mathbf{Z}$ , are calculated by analytical integration of Equation 102, and their expanded form can be found in Appendix B.

The above equations contain the equations of motions,  $(u, \psi)$  strain-displacement relations,  $(F, M)$  and velocity-displacement,  $(P, H)$ , equations.

The final bandwidth of the system is  $18N_{elem} + 6N_{kp}$  equations for a system with  $N_{elem}$  elements and  $N_{kp}$  boundary or “key” points.

## 2.5 Chapter Summary

This chapter details the mathematical formulations for the four geometrical nonlinearity methods reviewed in this thesis, namely, the displacement-based, the strain-based, the intrinsic and the modal methods. The focus of attention is on modeling of geometrically nonlinear beams, as stick models are the common structural representation techniques employed in the aerospace industries.

### 3 Case Study - Cantilever Beam Problem

To validate the nonlinear methodologies detailed in the previous section, a simple test case is presented, using a highly flexible cantilever beam, clamped at one end, as a case study. This was chosen due to its similarity of a highly flexible wing in a static aeroelastic condition.

For each of the formulations, the beam was discretized into 20 elements. The structural properties of the beam are given in Table 1.

To model static deflection, the beam was subjected to a uniformly distributed load across its length, and was prescribed in a purely vertical direction, non-follower load, as shown in Figure 5. The dynamic response of the beam was verified using the same distributed non-follower load, with a sinusoidal component, as given below

$$F_{dyn} = F_{static} \sin 2\pi t \quad (109)$$

where  $F_{static}$  is the static distributed load, and  $t$  is the current time in the transient solution.

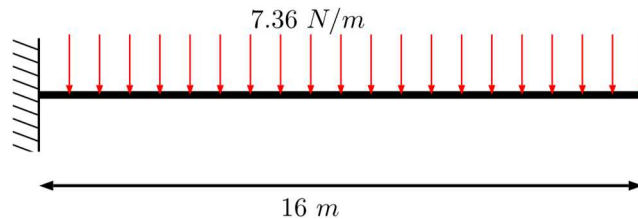


Figure 5: Cantilever beam used verification of nonlinear methodologies

Table 1: Structural properties of cantilever beam

$L_o$	16 m
$EA$	$10^{10} N$
$EI_{11}$	$2 \times 10^4 N \cdot m^2$
$EI_{22}$	$4 \times 10^6 N \cdot m^2$
$GJ$	$2.6 \times 10^4 N \cdot m^2$
$I_{xx}$	$0.1 kg \cdot m^2$
$I_{yy}$	$0 kg \cdot m^2$
$I_{zz}$	$0.1 kg \cdot m^2$
$\rho_{linear}$	$0.75 kg/m$

where  $EA, EI_{11}, EI_{22}$  are the extensional, out of plane, and in plane bending stiffnesses of the beam.  $GJ$  is the torsional stiffness and  $I_{xx}, I_{yy}$ , and  $I_{zz}$  are the mass moments of inertia about the beam primary axes.  $\rho_{linear}$  is the mass per unit length.

### 3.1 Numerical solution of nonlinear equations

For the displacement-based method, a MATLAB [61] code, based on the theory described in Section 2.1 is used to iteratively solve for the static solution using a full Newton Raphson solution scheme [24], [51]. For the dynamic root loads, the element internal force vector was computed as a pseudo-static analysis at each time step, using the overall load vector, including the applied load, elastic loads, and inertial loads, at the current time step.

For the strain-based method, the static and dynamic solutions were run using a MATLAB code based on the theory from [31], [34], [35], [59] detailed in Section 2.2. The strains in the static deformed configuration were solved by the following expression

$$\{\boldsymbol{\varepsilon}\} = [\mathbf{K}_{ff}]^{-1} \mathbf{R}_f \quad (110)$$

The physical displacements were then obtained using the strain-displacement Jacobian matrices as shown in Strain Based Formulation Matrices. The dynamic equations of motion were solved by setting the overall acceleration of the system at each time step to zero, and solving the differential equations using the constant time step backward difference *ode15s* time integration solver in MATLAB [62]. The dynamic forces and moments along the beam were obtained by substitution of the strains,  $\boldsymbol{\varepsilon}$ , and strain-rates,  $\dot{\boldsymbol{\varepsilon}}$ , at each time-step Equation 75 in Section 2.2, along with the condition of zero acceleration,  $\ddot{\boldsymbol{\varepsilon}}$ .

The geometrically exact intrinsic beam theory formulation was validated using the online tool “GEBT” from cdmHUB [63] based on the Geometrically Exact Beam Theory (GEBT) [64].

This tool implemented a mixed formulation of the geometrically exact beam theory, using displacements, rotations, velocities, and momenta as the independent degrees of freedom, and contained the capability for static and dynamic analyses of highly flexible beams. The static and dynamic analyses were run by solving Equation 102 using an eigenvalue solver [64].

The modal equations of motion were solved using the same dynamic solver used in the displacement-based method, with the exception of the physical matrices being replaced by

modal domain equivalents. As a modal method is inherently dynamic, no static results are provided.

### **3.2 Verification of results**

To verify the results from the various nonlinear methodologies, the test case beam was created in MSC Nastran input, using CBEAM elements, capable of modeling small-strain large-deformation geometric nonlinearities in static and dynamic analyses [65]. MSC Nastran is a widely used commercial finite element solver, which has been extensively used in the aerospace industry, and as such, is a convenient tool to validate the other nonlinear methods examined in this thesis. To ensure that the simulation results of MSC NASTRAN solution sequence 129 for transient nonlinear analysis is taking into effect geometric nonlinearity at each time step, the solver is forced to update the stiffness matrix at every interval. Correspondingly for static solutions, NASTRAN solution sequence 106 is used, with the stiffness matrix being updated at each step.

#### **3.2.1 Static test results**

The results for the static deformed configuration for the three nonlinear methodologies, as well as the bending moment along the beam, are shown in Figure 6 and Figure 7, respectively.

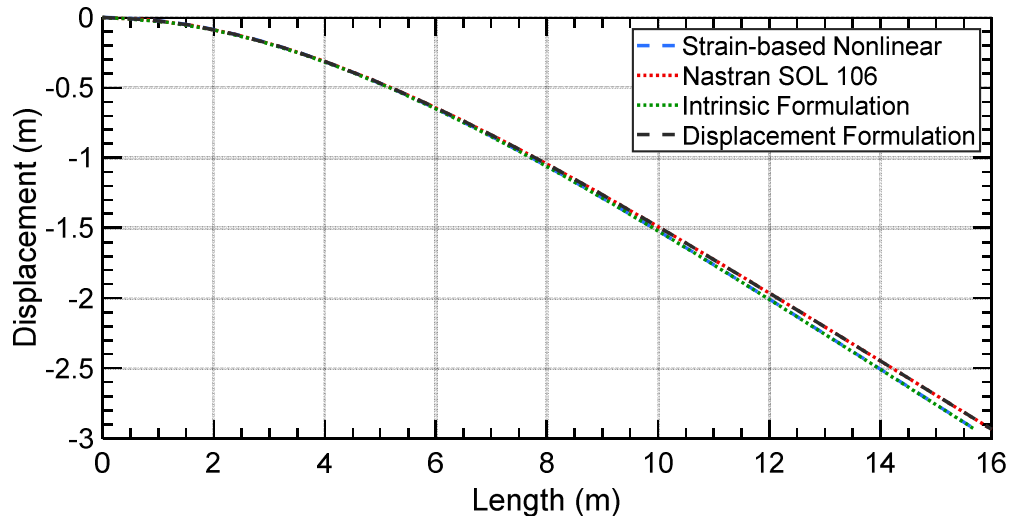


Figure 6: Deformed configuration of cantilever beam subject to gravity load

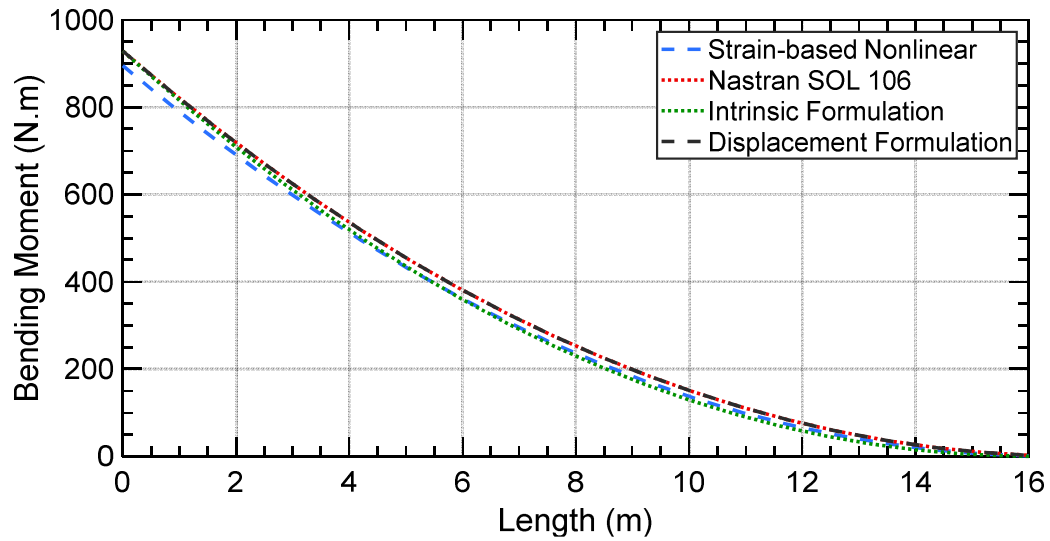


Figure 7: Bending moment across length of cantilever beam

The results of the static nonlinear deflection show general agreement between the methods. In particular, the geometrically nonlinear Euler-Bernoulli displacement-based beam element shows results which are indistinguishable from MSC Nastran, indicating an excellent match. This was partially to be expected, as the geometrically nonlinear beam

theory presented in Section 2.1, is the same as total Lagrangian formulation used in MSC Nastran [19].

The intrinsic GEBT formulation and the strain formulation are also in general agreement with the other results, however, the results are not identical to that of MSC Nastran. The beam tip deflection for the different simulation methods are within 1% of each other. However, the bending moment at the root calculated by the strain-based methodology is 3.58% lower than that of the other methods.

Table 2: Comparison of tip displacement and root bending moment for static loading conditions

Methodology	Tip Displacement ( $m$ )	Error (%)	Root Bending Moment ( $Nm$ )	Error (%)
Nastran SOL 106	2.934	0.00	928.9	0.00
Displacement	2.934	0.00	928.9	0.00
Strain	2.932	-0.07	895.6	-3.58
Intrinsic	2.930	-0.13	929.0	0.01

### 3.2.2 Dynamic test results

In the dynamic loading case, the tip displacement and the root bending moments are plotted as a function of time, as shown in Figure 8 and Figure 9.

Table 3: Comparison of tip displacement and root bending moment for dynamic loading conditions

Methodology	Maximum Tip Displacement ( $m$ )	Error (%)	Maximum Root Bending Moment ( $Nm$ )	Error (%)
Nastran SOL 129	1.699	0.00	378.9	0.00
Displacement	1.607	-5.41	423.2	10.4
Strain	1.693	-0.35	381.2	0.61
Intrinsic	1.706	0.41	382.5	0.95
Modal	1.592	-6.30	406.2	6.72

The transient tip response of the beam to a sinusoidal input matches very closely across the strain and intrinsic methods, while the modal and displacement methods show the largest discrepancy in peak displacements occurring for the displacement-based solver, at 6.7% and 10.4% respectively. The root bending loads are more varied, as while they all have a similar general waveform, it can be seen that the strain based method is less sensitive to the higher frequency variations in moment, which was described by Su [35]. The intrinsic method shows general agreement with Nastran's transient SOL 129. The displacement method results are very close to the other two.

Overall, all three methods show close agreement with each other with the exception of the modal method, which is to be expected as only 5 modes were used. Using more mode shapes would increase the accuracy of the modal method while simultaneously removing any computational advantage over the other methods.

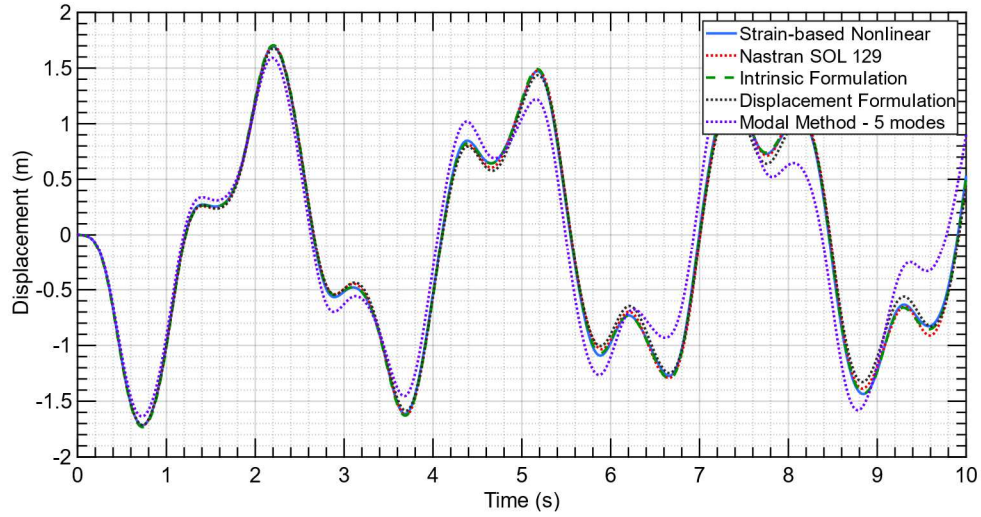


Figure 8: Tip displacement of cantilever beam as a function of time

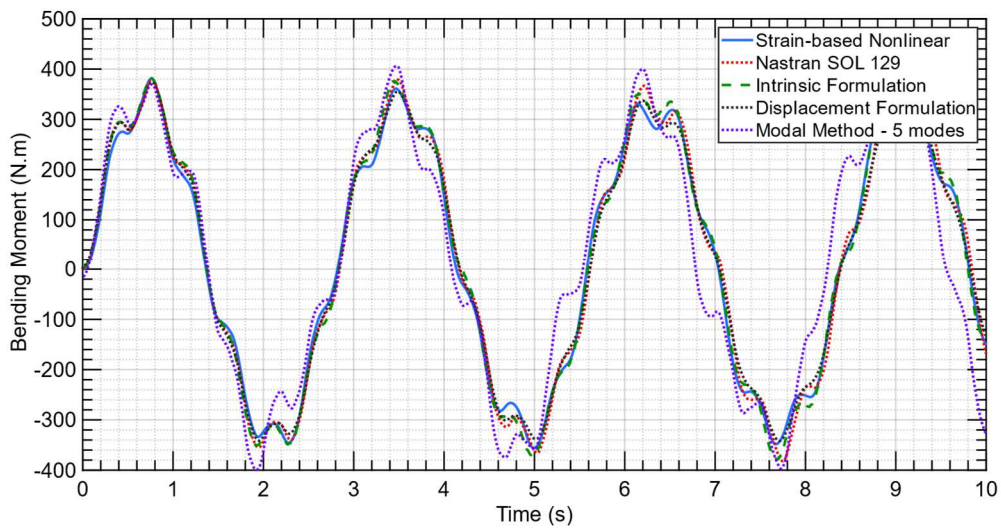


Figure 9: Dynamic bending moment at clamped end of cantilever beam

### 3.3 Key differences between formulations

There are a number of differences between the nonlinear methods, which are a result of the differing mathematical formulations. The key differences are discussed in summary below.

Displacement based methods have the most straightforward problem setup and solution methods due to the choice of physically relevant independent variables, which comes at the expense of computational time due to frequently having second or higher order nonlinear terms in the equations of motion.

Strain methods are advantageous for static problems due to the constant stiffness matrix, which results in a straightforward solution. In addition, the computation of beam internal forces is direct, due to not having to compute strains from displacements as in other methods. It has also been stated in literature that strain based methods may have issues capturing high-frequency components of the dynamic response.

Intrinsic methods, depending on the formulation, may have computational advantages due to formulations having low order nonlinearities, when compared to the displacement based method.

Modal methods have the fastest solution times of all methods, depending on the number of modes used, which comes at the expense of result accuracy, with more modes increasing the accuracy as well as solution time

### **3.4 Chapter Summary**

This Chapter provided the results of the comparative study between four separate nonlinear beam modeling methodologies, as well as their fidelity in calculation of loads when compared to commercially validated nonlinear solvers. In addition, the results justify the choice of using a displacement based beam model to model geometrically nonlinear effects in aeroelastic loads calculation as shown in the next Chapter.

## 4 Nonlinear Static Aeroelasticity

In linear structural analyses, the equations of equilibrium are formulated with respect to the undeformed geometry, as the geometrical variation due to infinitesimal deformations are assumed to be negligible [66]. When the deformations are large enough, this assumption is no longer accurate, and the equations of motion can be defined with respect to the deformed structure, resulting in nonlinear governing equations of motion [67].

### 4.1 Theoretical Formulation

Commercial Finite Element code packages, such as MSC Nastran [19], often use a Lagrangian method, where the Finite Element mesh follows the deformation of the structure [68]. Within this, there are two formulations, the Total Lagrangian Formulation (TLF) [69] and the Updated Lagrangian Formulation (ULF) [58]. In the TLF, equilibrium is expressed relative to the original undeformed structure, while in the ULF, the reference state is the current [58].

#### 4.1.1 Nonlinear Structural Formulation

The theory for a geometrically nonlinear corotational beam element was presented in Section 2.1. More generally, the geometrically nonlinear equations for a solid are obtained via inclusion of higher order nonlinear terms in the strain-displacement relationship. The following equations are based on the formulation for general elements, as derived in the reference text by Bathe [24]. The resulting set of equations are given below

$${}^t\varepsilon_{ij} = {}^t\varepsilon_{Lij} + {}^t\varepsilon_{NLij} \quad (111)$$

where  $\varepsilon$  are components of the Green-Lagrange strain tensor, consisting of linear and nonlinear strains, given at time  $t$ , with respect to physical coordinates axes  $i, j$ , where  $i, j \in 1, 2, 3$ .

The constitutive model is still linear, as hyper-elasticity or plasticity are not considered, and thus the stress-strain relationship is given as follows:

$${}^t S_{ij} = {}^t C_{ijrs} {}^t \varepsilon_{rs} \quad (112)$$

where  $S_{ij}$  are components of the Second Piola-Kirchhoff (PK2) stress tensor,  $C_{ijrs}$  are components of the linear elasticity tensor, and  $r, s \in 1, 2, 3$ . At the next incremental iteration,  $t + \Delta t$ , the PK2 tensor is denoted as follows:

$${}^{t+\Delta t} S_{ij} = {}^t S_{ij} + {}^t \tau_{ij} \quad (113)$$

where  $\tau$  are the components of the Cauchy (or true) stress tensor.

The principle of virtual work is used to formulate the primary static equation, as follows:

$$\int_V ({}^{t+\Delta t} S_{ij}) ({}^{t+\Delta t} \varepsilon_{ij}) dV = {}^{t+\Delta t} W \quad (114)$$

where  $W$  is the virtual work due to external applied forces. It is important to note that the usage of time steps,  $t = 0, \Delta t, 2\Delta t, \dots$ , in the static formulation of this chapter are equivalent to iterations in  $k = 1, 2, 3 \dots$ , from Section 2.1. As such, the equations will be written in the latter form for the rest of this chapter.

Substituting in Equations 111, 112, and 113 into Equation 114, the following finite element equation is obtained

$$\left[ \int_V [{}^k\mathbf{B}^L]^T \mathbf{C} [{}^k\mathbf{B}^L] dV + \int_V [{}^k\mathbf{B}^G]^T {}^k\boldsymbol{\tau} [{}^k\mathbf{B}^G] dV \right] \Delta \mathbf{U} \quad (115)$$

$$= {}^{k+1}\mathbf{R} - \int_V [{}^k\mathbf{B}^L]^T {}^k\hat{\boldsymbol{\tau}} dV$$

where  $\mathbf{C}$  is the elasticity tensor,  ${}^k\boldsymbol{\tau}$  and  ${}^k\hat{\boldsymbol{\tau}}$  are the matrix and vector forms of the Cauchy stress tensor, and  $\Delta \mathbf{U}$  is the incremental deformation from iteration  $k$  to  $k + 1$ .  ${}^{k+1}\mathbf{R}$  is the vector of applied forces at the next iteration,  ${}^k\mathbf{B}^L$  and  ${}^k\mathbf{B}^G$  are the linear and non-linear strain-displacement transformation matrices respectively. After integration of the equations using Gauss-Legendre quadrature, Equation 115 can be rewritten as given below

$$[{}^k\mathbf{K}^L + {}^k\mathbf{K}^G] \Delta \mathbf{U} = {}^{k+1}\mathbf{R} - {}^k\mathbf{F} \quad (116)$$

where  ${}^k\mathbf{K}^L$  and  ${}^k\mathbf{K}^G$  are the linear and nonlinear stiffness matrices, and  ${}^k\mathbf{F}$  is the vector of internal element stresses, all assembled at iteration  $k$ .

#### 4.1.2 Nonlinear Aeroelasticity Formulation

In a standard aeroelastic analysis, the aerodynamic pressure,  $\hat{f}_{aero}$ , is related to the downwash,  $\hat{w}$ , at the aerodynamic surfaces as follows

$$\hat{f}_{aero} = q_{dyn} \mathbf{A}_{AIC}^{-1} \hat{w} \quad (117)$$

and the downwash is given as follows

$$\hat{w} = \mathbf{D} \mathbf{U}_{aero} + \hat{w}^g \quad (118)$$

The Aerodynamic Influence Coefficient (AIC) matrix is given by  $\mathbf{A}_{AIC}$ ,  $q_{dyn}$  is the dynamic pressure at the desired flight conditions, and  $\mathbf{D}$  is the matrix relating the displacements of the aerodynamic panels,  $\mathbf{U}_{aero}$ , to the downwash. In a standard linear aeroelastic solution, vector of additional downwash,  $\hat{w}^g$ , is usually zero, unless the wing

being modeled has an initial camber or twist distribution. In this work, the additional downwash vector is used to include the nonlinear component of wing twist due to large deformation effects.

The total aerodynamic force vector of the structure,  $\hat{\mathbf{L}}$ , can then be given as follows

$$\hat{\mathbf{L}} = \mathbf{S}\hat{\mathbf{f}}_{aero} + \mathbf{F}_{rig} \quad (119)$$

where  $\mathbf{S}$  is a matrix relating nodal pressures to nodal forces, and  $\mathbf{F}_{rig}$  is a vector of rigid applied loads on the structure, such as engine loads and point loads.

The force-displacement relationship for a static structure is given by

$$\mathbf{R} = \mathbf{K}_{glob}\mathbf{U} \quad (120)$$

where  $\mathbf{R}$  is the total load on the structure,  $\hat{\mathbf{u}}$  is the global displacement vector due to the applied load, and  $\mathbf{K}_{glob}$  is the global tangent stiffness matrix of the structure.  $\mathbf{K}_{glob}$  can be formulated with respect to the initial configuration of the structure, as in linear analyses, or with respect to the deformed configuration, as in a geometrically nonlinear analysis.

Equating the RHS of Equations 119 and 120, the expression for an aeroelastic system at equilibrium is given below

$$\mathbf{S}\hat{\mathbf{f}}_{aero} + \mathbf{F}_{rig} = \mathbf{K}_{glob}\mathbf{U} \quad (121)$$

Substituting Equations 117 and 118 into the above expression yield the following relationship

$$\underbrace{q\mathbf{S}\mathbf{A}_{AIC}^{-1}}_{\mathbf{Q}} [\mathbf{D}\mathbf{U} + \hat{\mathbf{w}}^g] + \mathbf{F}_{rig} = \mathbf{K}_{glob}\mathbf{U} \quad (122)$$

Let  $\mathbf{Q}$  be a matrix that related the nodal downwash to the nodal forces. The effects of geometric nonlinearity can be incorporated into Equation 122 as follows

$$\mathbf{Q}[\mathbf{D}\mathbf{U} + \widehat{\mathbf{w}}^g] + \mathbf{F}_{rig} = [\mathbf{K}^L + \mathbf{K}^G]\mathbf{U} \quad (123)$$

and solved using an iterative procedure

$${}^k\mathbf{Q}[{}^k\mathbf{D}{}^k\mathbf{U} + {}^k\widehat{\mathbf{w}}^g] + {}^k\mathbf{F}_{rig} = \underbrace{[{}^{k+1}\mathbf{K}^L]{}^{k+1}\mathbf{U}}_{\text{linear load}} + \underbrace{[{}^{k+1}\mathbf{K}^G]{}^{k+1}\mathbf{U}}_{\text{nonlinear increment}} \quad (124)$$

where  $k$  is the iteration number,  ${}^k\widehat{\mathbf{w}}^g$  is the nonlinear increment in wing twist, and  ${}^{k+1}\mathbf{U}$  is the structural displacement vector at the end of the current iteration.

The convergence of the above equation is determined by the difference in nodal displacement along all the wing nodes,  $1, 2, \dots, n$ , given as

$${}^k\sigma_e > \max({}^k\mathbf{U}_n - {}^{k-1}\mathbf{U}_n) \quad (125)$$

where  $\mathbf{U}_n$  is a subset of  $\mathbf{U}$  containing only the nodes of the aircraft wing.

Equation 124 is determined to have converged when  $\sigma_e$  is small. For the purposes of this study, the convergence parameter is chosen such that there is less than 0.1% difference in the displacement between consecutive iterations. The increase in the loads due to the inclusion of geometric nonlinearities can then be defined as follows

$$\Delta_e = \left( \frac{[{}^k\mathbf{K}^L + {}^k\mathbf{K}^G]{}^k\mathbf{U}^{NL}}{{}^k\mathbf{K}^L\mathbf{U}^L} \right) \times 100\% \quad (126)$$

where  $\mathbf{U}^L$  and  $\mathbf{U}^{NL}$  are the linear and nonlinear deformed configuration of the aircraft, corresponding to iteration 1 and iteration  $k$  of Equation 125 respectively.

#### 4.1.3 Linear Aerodynamic Formulation

The aerodynamic loads are calculated using Nastran SOL 144, which uses the Doublet Lattice Method (DLM) [36], [70], [71]. This method is based on linearized potential flow theory, where a line of potential doublets of unknown strength lie along the

quarter-chord of each aerodynamic panel. Given  $n$  aerodynamic boxes with a constant force per unit length along the quarter-chord line,  $\mathbf{f}$ , the strength of a doublet line segment  $j$  is given as

$$\frac{\mathbf{f}_j}{4\pi\rho_{air}} \int L_j ds \quad (127)$$

where  $L_j$  is the length of the doublet line,  $ds$  is an increment along the line, and  $\rho_{air}$  is the density of air. The total downwash at any point on the aerodynamic surface  $(x_i, s_i)$  can then be written as the sum of all the downwash due to all the doublets on the surface.

$$\bar{w}(x_i, s_i) = \sum_{j=1}^n \left( \frac{\mathbf{f}_j}{4\pi\rho_{air}} U_{free}^2 \right) \int \hat{\Gamma} ds \quad (128)$$

where  $U_{free}$  is the freestream velocity of the airflow across the panels, and  $\hat{\Gamma}$  is the kernel function for a nonplanar surface [72].

When Equation 128 is applied to all the downwash points, the force per unit length along the quarter-chords of the boxes can be determined, and thus, the average pressure,  $F_{box}$ , on each aerodynamic box is written as

$$F_{box_i} = \frac{\mathbf{f}_i}{\Delta x_j \cos \lambda_j} \quad (129)$$

where  $\Delta x_j$  is the average chord of the  $j$ th box, and  $\lambda_j$  is the sweep angle of the doublet line on the box. Given the  $j$ th index of doublet lines and  $i$ th index of the downwash points, Equation 128 can be re-written as

$$\bar{w} = \sum_{j=1}^n D_{ij} f_{box_j} \quad (130)$$

where  $D_{ij}$  are the elements of matrix  $\mathbf{D}$  in Equation 118 and  $f_{box_j}$  is the average pressure,  $F_{box}$ , nondimensionalized by  $\frac{1}{2}\rho_{air}U_{free}$ . The individual elements of matrix  $\mathbf{D}$  are given as follows

$$\frac{\pi}{8}\Delta x_j \cos \lambda_j \int \hat{\Gamma} ds \quad (131)$$

Equation 118 represents the downwash acting on an aerodynamic panel. However, trimming the aircraft into a steady state condition often requires the use of aerodynamic degrees of freedom, such as angle of attack, rotation rates, and control surface deflections, to modify the net forces and moments acting on the structure, which can be incorporated into the expression for the downwash as follows:

$$\hat{w} = \mathbf{D}\mathbf{U} + \mathbf{D}_\sigma \hat{u}_\sigma + \hat{w}^g \quad (132)$$

where  $\mathbf{D}_\sigma$  is a matrix relating the aerodynamic degrees of freedom,  $\hat{u}_\sigma$ , to the downwash. All prior equations assume that the aerodynamic forces are applied directly to the structural nodes. However, due to differences in the meshing of aerodynamic panels and structural members, this is not always the case. This is because the aerodynamic panels are applied at the quarter-chord point of each aerodynamic box element, which is quite often much larger in number than the actual structural elements. The forces need to be coupled to the structural degrees of freedom of the airframe, which is achieved using a linear beam spline using an interpolation matrix.

$$\mathbf{U}_{aero} = \mathbf{G}_{spline} \mathbf{U}_{struct} \quad (133)$$

where  $\mathbf{G}_{spline}$  is the interpolation matrix relating the structural deflections  $\mathbf{U}_{struct}$ , to the aerodynamic nodal deflections  $\mathbf{U}_{aero}$

Imposing the condition that the virtual work performed by both deflections is identical, an expression for an arbitrary force transformation between the aerodynamic and structural nodes is given as follows

$$\mathbf{F}_{struct} = [\mathbf{G}_{spline}]^T \mathbf{F}_{aero} \quad (134)$$

where  $\mathbf{F}_{aero}$  is a vector of aerodynamic loads on aerodynamic nodes, and  $\mathbf{F}_{struct}$  are the resulting aerodynamic loads on structural nodes.

The final equation of motion for a static linear aeroelastic problem can then be given as follows

$$[\mathbf{K}^L - \mathbf{QD}]\mathbf{U} + \mathbf{M}\ddot{\mathbf{U}} = \mathbf{Q}_\sigma \mathbf{D}_\sigma \hat{u}_\sigma + \mathbf{Q}\hat{w}^g + \mathbf{F}_{rig} \quad (135)$$

It can be seen that this is a very similar form to Equation 123, with the addition of  $\mathbf{Q}_\sigma$ , a matrix that relates aerodynamic degrees of freedom (control surface deflections, incidence angles, rotation rates), to the aerodynamic forces,  $\mathbf{M}$  is the structural mass matrix, and  $\ddot{\mathbf{U}}$  is a vector of rigid body accelerations due to gravity and flight maneuvers. Equation 135 is partitioned to separate the restrained and free degrees of freedom, and can be solved to obtain the trimmed flight condition of the aircraft [36].

## 4.2 Methodology

This section outlines the developed methodology to couple linear aerodynamics to a geometrically nonlinear structural methodology, to create an iterative solution which incorporates geometrically nonlinear effects into static aeroelasticity. Two separate solvers in MSC Nastran are used as the tools to implement the iterative Equation 124.

#### 4.2.1 Modified Iterative Method

Equation 124 is implemented using the linear aeroelasticity (SOL 144) and nonlinear structural analysis (SOL 106) solvers of MSC Nastran. In a flexible aeroelastic trim solution, the Doublet Lattice Method is used to calculate the aerodynamic loads on the aircraft, which are a function of the aircraft current deformed configuration, to solve for Equation 135. However, the aeroelastic module in Nastran does not account for the effects of geometric nonlinearity, which can be shown to be significant for highly flexible aircraft. This work builds upon the iterative method proposed in [9], by including the effect of wing twist due to aeroelastic loading as an additional downwash, increasing the fidelity of loads calculated. As such, it can be used to determine the effects of large displacement nonlinearities on the aircraft loads. A flowchart of the iterative process is shown below in Figure 10.

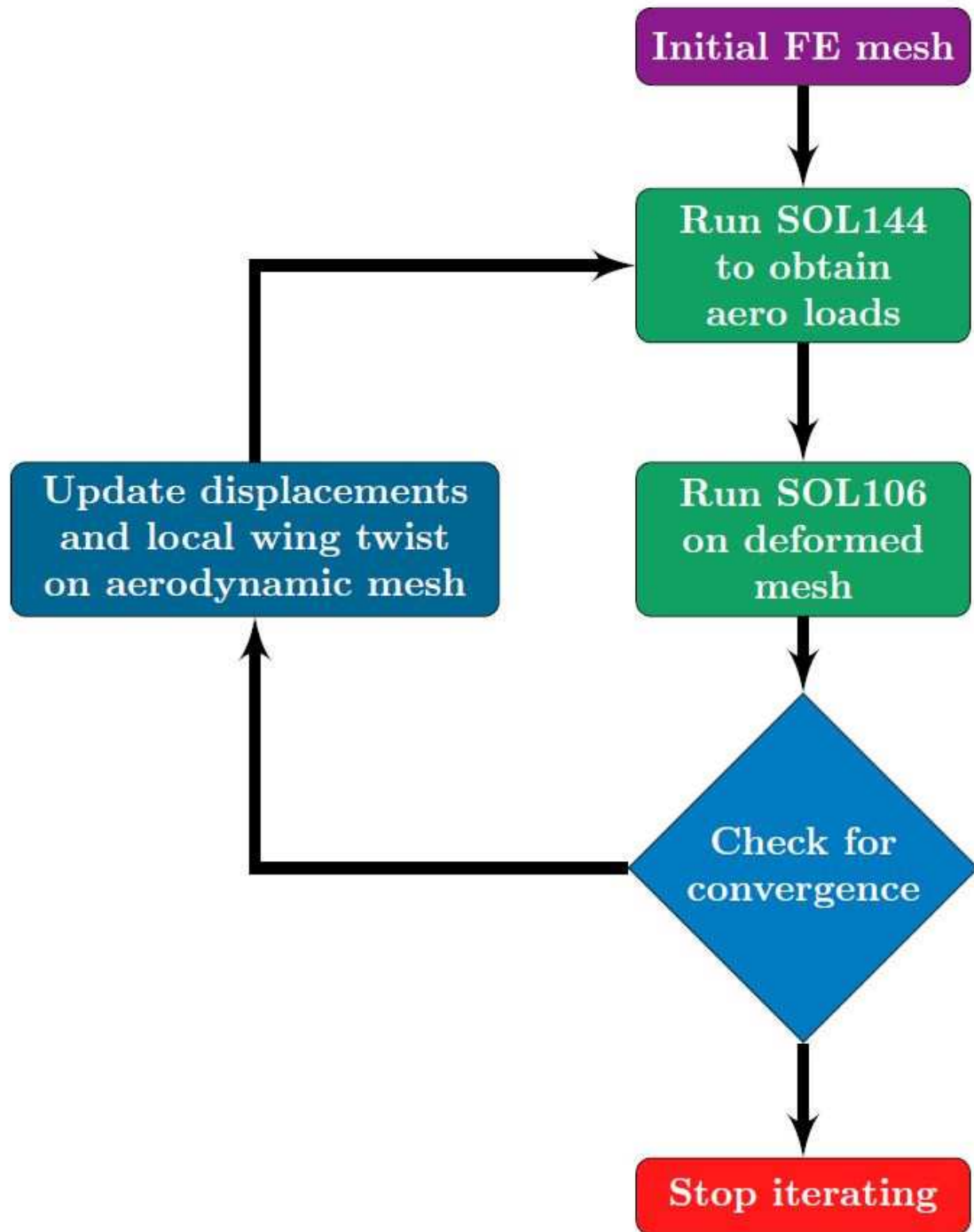


Figure 10: Flowchart depicting the Modified Nastran Iterative Method

This method uses linear panel method (DLM) aerodynamics to calculate the loads on the structure, which are applied on the undeformed structure. A displacement-based

geometrically nonlinear method is used to calculate the nonlinear displacements of the structure, including follower force effects, and the new displacements are used to update the structural and aerodynamic mesh used for the aerodynamic loads calculation to obtain a new set of loads corresponding to the new deformed configuration. The process is repeated until the structure converges at a deformed shape configuration. The loads acting on the aircraft structural elements due to this new deformed configuration can now be obtained.

#### *4.2.1.1 Limitations of Nastran Aerodynamics*

The aerodynamic implementation uses the doublet lattice method, which divides the surface into a number of panels parallel to the free stream velocity [70]. However, the DLM implementation in Nastran's aerodynamics loads solver places the flow direction in the positive  $x$ -direction, which has to be parallel to the  $x$  axis of every aerodynamic panel box element [36]. In addition, the resultant aerodynamic forces are applied in the coordinate system of the undeformed aerodynamic panel. Aerodynamic forces are based on the aerodynamic pressure on the lifting surfaces. As pressures are, by definition, normal to the surface, these aerodynamic loads are follower forces which should ideally be normal to the aerodynamic box elements as they twist and deform. However, in Nastran, the resultant aerodynamic forces are applied in the coordinate system of the undeformed panel, leading to omission of the inboard component of the lift force when the wing deforms.

Due to the assumption of a flexible structure, the wing can bend along its perpendicular axes, and twist along its own axis. This local torsional deformation changes the local angle of attack along the wing, thus changing the lift distribution of the wing, and cannot be ignored.

#### 4.2.1.2 *Proposed solution to limitations*

The above-mentioned limitations are resolved by the Modified Iterative Method in the following manners.

The follower load limitation is resolved by updating the position and orientation of the aerodynamic panels to match the deformed aircraft in the current iteration  $k$ . This allows the lift force to act as a “pseudo” follower force, as the orientation of the lift changes with every iteration to follow the deformation of the wing.

The second limitation is circumvented by adding a downwash angle on the aerodynamic panels corresponding to the local twist angle of the wing.

#### 4.2.2 **Case Study**

To verify effectiveness of the Modified Nastran Iterative Method, a Bombardier Aircraft platform is used for the purposes of this thesis for a case study. As a detailed 3D Global Finite Element Model (GFEM) of an aircraft would be very computationally expensive in an iterative aeroelastic analysis, a stick model of the aircraft is used, as shown in Figure 11.

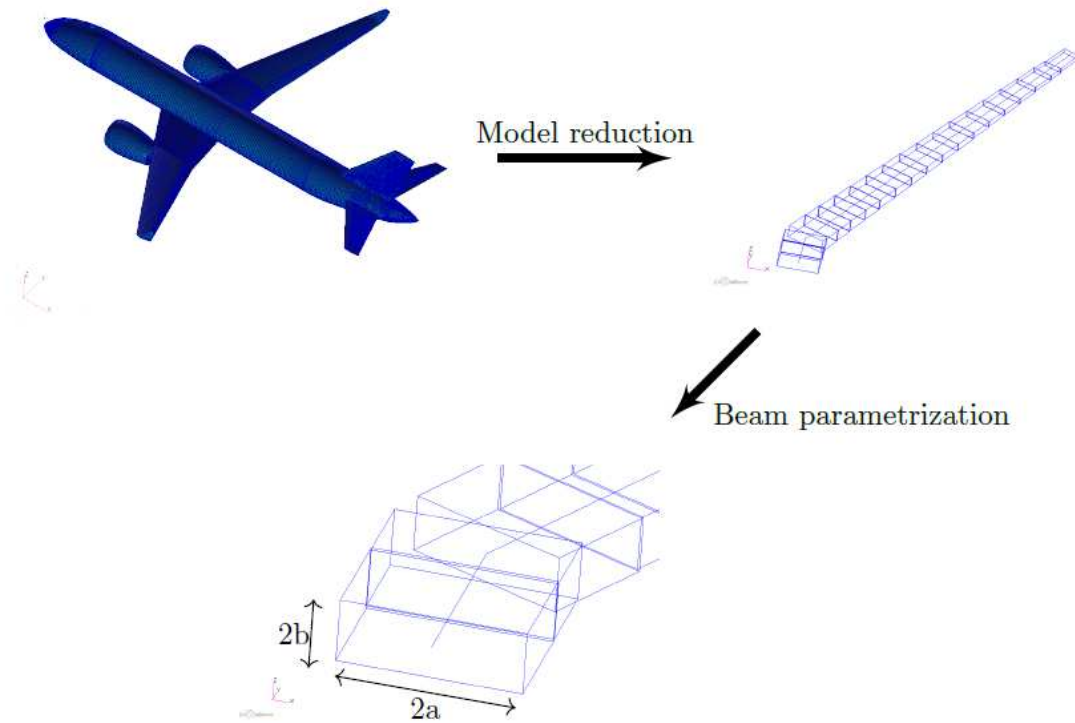


Figure 11: Reduction from Global Finite Element Model (GFEM) to a Stick Model (SM) for a generic twin engine aircraft

#### 4.2.2.1 *Stick Model generation*

A stick model is a reduced order model represented by a series of beam elements extending along the aircraft elastic axis that resembles the overall structural behavior of its 3D GFEM counterpart. There are several stick model development methodologies available in the literature [10]–[15]. A common stick model development method adopted by the aerospace industry involves the extraction of stick beam equivalent stiffness properties using unitary loading method [12], [15]. This methodology is employed in this thesis for the 3D GFEM model order reduction.

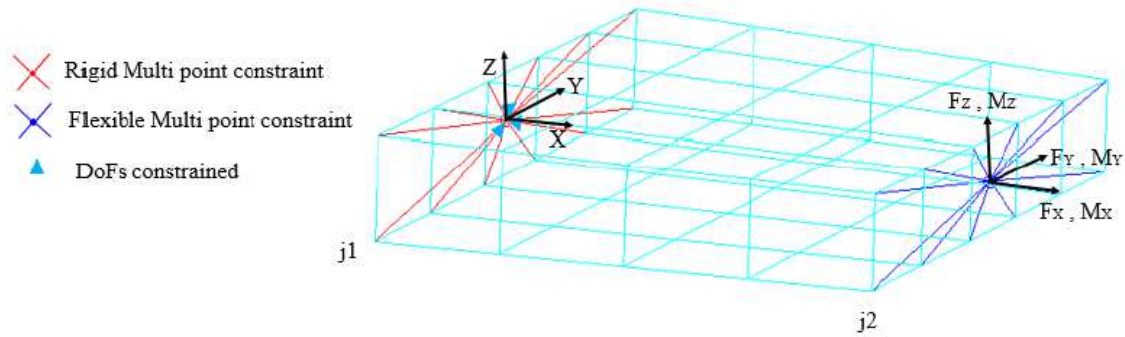


Figure 12: Schematic drawing showing GFEM reduction process to Stick Model

Figure 12 shows a schematic drawing that illustrates the stiffness extraction process of the stick model of a single bay of the 3D GFEM of aircraft wing box. A wing bay is the segment of the 3D GFEM extending between two consecutive wing stations that is replaced with a single Timoshenko beam element within the stick model reduced order model. Here, the shear centers of the cross-sections at the two ends of a single wing bay are located and a local reference coordinate system is identified at these locations. The shear centre at each subdivision is located by finding the chord-wise point of minimum torsion when a shear load is applied. The defined coordinate system is assumed as a principal coordinate system with its torsional axis extending along the line connecting the predefined shear centers at the ends of the wing bay while the first principal bending axis is assumed along the section airfoil chord line, as shown in Figure 12. A cantilevered boundary condition is assumed with the inboard end,  $j1$ , is fixed. Six load cases involving unit forces and moments are applied at the shear center of the free end,  $j2$ , and the stiffness properties for the beam element representing the wing bay are computed as given below

$$A_{j1 \rightarrow j2} = \frac{L_{j1 \rightarrow j2}}{E |\delta_{j1 \rightarrow j2}|_x} \quad (136)$$

where  $A_{j1 \rightarrow j2}$  is the equivalent cross-sectional area,  $L_{j1 \rightarrow j2}$  is the bay length,  $|\delta_{j1 \rightarrow j2}|_x$  is the axial elongation due to an applied unit load along the  $x$  axis, and  $E$  is the material Young's Modulus.

Similarly, the shear factors along the  $y$  and  $z$  directions,  $K_y$  and  $K_z$  respectively, are computed as

$$(K_y)_{j1 \rightarrow j2} = \frac{L_{j1 \rightarrow j2}}{GA_{j1 \rightarrow j2} |\delta_{j1 \rightarrow j2}|_y} \quad (137)$$

$$(K_z)_{j1 \rightarrow j2} = \frac{L_{j1 \rightarrow j2}}{GA_{j1 \rightarrow j2} |\delta_{j1 \rightarrow j2}|_z} \quad (138)$$

where  $|\delta_{j1 \rightarrow j2}|_y$  and  $|\delta_{j1 \rightarrow j2}|_z$  are the translational deformation in the  $y$  and  $z$  directions due to a corresponding unit shear loading, and  $G$  is the shear modulus.

Moments of inertia of the stick model beam element are computed using the rotational deformations corresponding to the application of unit moments in same manner as described before. The equivalent bending moments of inertia,  $I_y$  and  $I_z$ , along the  $y$  and  $z$  directions, as well as the torsional moment of inertia,  $J_x$ , in the  $x$  direction is given as

$$(I_y)_{j1 \rightarrow j2} = \frac{L_{j1 \rightarrow j2}}{E |\theta_{j1 \rightarrow j2}|_y} \quad (139)$$

$$(I_z)_{j1 \rightarrow j2} = \frac{L_{j1 \rightarrow j2}}{E |\theta_{j1 \rightarrow j2}|_z} \quad (140)$$

$$(J_x)_{j1 \rightarrow j2} = \frac{L_{j1 \rightarrow j2}}{G |\theta_{j1 \rightarrow j2}|_x} \quad (141)$$

where  $|\theta_{j_1 \rightarrow j_2}|_x$ ,  $|\theta_{j_1 \rightarrow j_2}|_y$ , and  $|\theta_{j_1 \rightarrow j_2}|_z$  are the angular deformations along  $x, y, z$  directions due to a corresponding unit moment.

It should be noted that the standard practice in the aerospace industry for aeroelasticity analysis involves the use of lumped mass idealization of the 3D GFEM [12]. The equivalent lumped mass [73]. for each aircraft bay can be easily calculated from the aircraft CAD model.

#### 4.2.2.2 Validation of Stick Model

The developed stick model was validated by comparing the loads along the wingspan for the aircraft in steady flight using the 3D GFEM model and the reduced stick model, also referred to as the EIGJ stick. The out of plane bending, out of plane shear, and torsional loads are compared along the full wing-span. As can be observed from Figure 13, Figure 14 and Figure 15, there is a very good agreement between the two models, justifying our use of the reduced stick model.

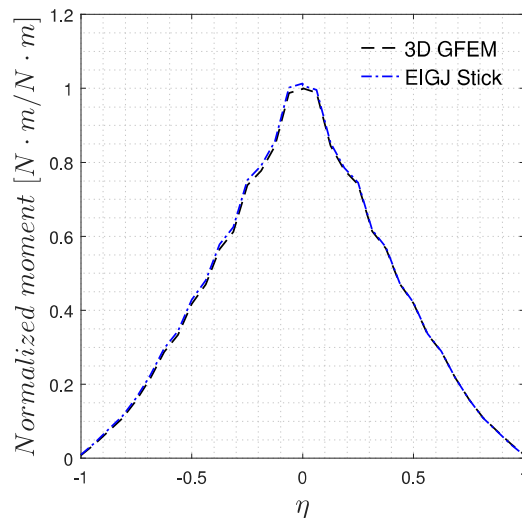


Figure 13: Comparison of normalized bending moment along wingspan of GFEM and Stick Model

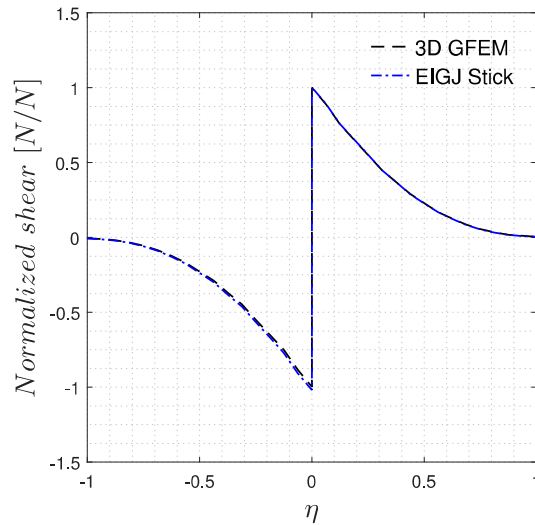


Figure 14: Comparison of normalized shear force along wingspan of GFEM and Stick Model

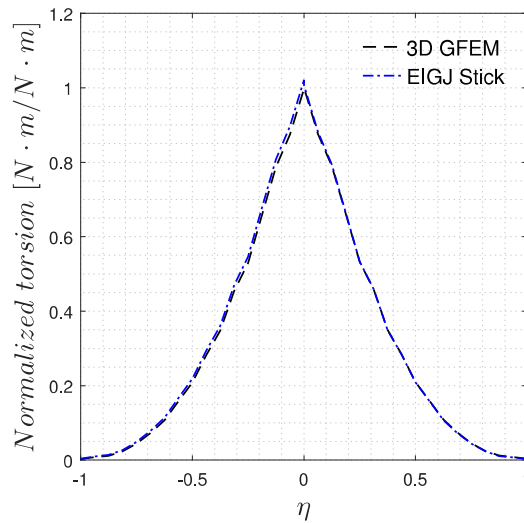


Figure 15: Comparison of normalized torsional moment along wingspan of GFEM and Stick Model

#### 4.2.2.3 Methodology to vary mass and stiffness of airframe

The aerodynamic model of the aircraft requires the inclusion of control surfaces to trim the aircraft at various flight conditions. The control surfaces defined are two ailerons, an elevator, and a rudder. All analyses are run in the steady level flight condition given in Table 4, and the model is free in the plunge and pitch degrees of freedom, and the pitch

rate is constrained to zero. The aerodynamic solver, SOL 144, poses the problem of trimming the aircraft as a system of equations.

Table 4: Steady flight conditions used

Parameter	<i>Value</i>
Mach Number	0.6
Altitude ( <i>ft</i> )	29500
Dynamic Pressure ( <i>psi</i> )	1.1272
True Air Speed ( <i>ft/s</i> )	598.20

As the goal of this study is to document the differences in loads when the aircraft structure is modified, a methodology is needed to create stiffness and mass variations to the structure. In this thesis, only the wing elements are modified, leaving the fuselage, horizontal and vertical tails unmodified. Since the analysis is being performed on an actual aircraft model, the mass and stiffness data points from the sizing optimization of the aircraft, which was provided by Bombardier Aerospace, are used to create a relationship between the structural properties ( $E, A, I_{11}, I_{22}, J$ ) and the resultant mass of each beam element. Following this, each beam element is assumed to have an equivalent rectangular cross-section. The cross-sectional dimensions of the equivalent beam element, namely the width and height, are then parametrized using the given relationships for the beam properties [74], which are used to parametrize the beam properties as functions of their geometry. The relationship between geometry and beam properties are then given by the following expressions.

$$I_{11} = \frac{4ab^3}{3} \quad (142)$$

$$I_{22} = \frac{4a^3b}{3} \quad (143)$$

$$J = ab^3 \left[ \frac{16}{3} - 3.36 \frac{b}{a} \left( 1 - \frac{b^4}{12a^4} \right) \right], \quad a \geq b \quad (144)$$

Equations 142, 143, and 144 allow the beam dimensions to be varied, to create a set of flexibility cases from the baseline structure. The structural mass is obtained using a linear relationship obtained from the design data of the aircraft, which consisted of hundreds of design iterations, where the mass is dependent on the beam dimensional and structural properties.

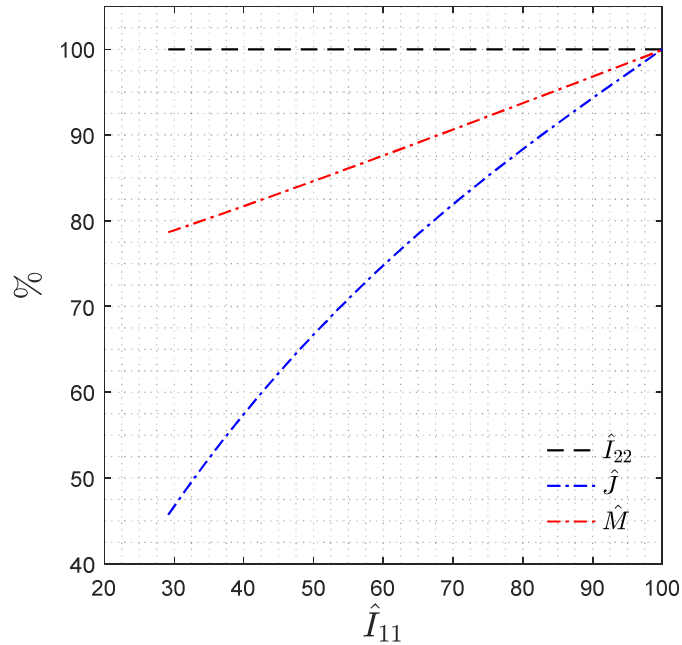


Figure 16: Variation of the in-plane stiffness, torsional stiffness, and element mass, as a function of out of plane stiffness

To generate the various mass and stiffness cases, the beam element parameters are varied such that out of plane bending stiffness,  $\hat{I}_{11}$ , ranges from 30% to 100%. The stiffness data generated, shown in Figure 16, shows the variation of the in-plane stiffness  $\hat{I}_{22}$ , the torsional stiffness  $\hat{J}$ , and the element mass  $\hat{M}$ . Note that in this section, the ( $\hat{\quad}$ ) hatted quantities represent the values that have been normalized with respect to their value on the baseline unmodified airframe.

As the individual beam stiffness along the wing stick model varies, the span-wise distribution of the stiffness is kept constant, and the stiffness parameters of every element along the wings are varied by a scaling factor determined with respect to a single element at the root. This ensures that the only difference in stiffness across all the generated model data is the relative stiffness determined by the aforementioned scaling factor. A program is written in MATLAB to take the reference aircraft and parametrize each of the wing elements by solving Equations 142 to 144 for the equivalent rectangular cross-section. The parametrized model properties are then written into the Nastran beam format, and the Modified Iterative Method is used to determine the loads.

As such, for the purposes of this thesis, the out of plane stiffness of the wing is varied from the baseline of 100%, to 30% of the baseline, representing a 21% reduction in mass,  $\hat{M}$ . The lower end of the defined range, 30%, was selected by observing the stability of the iterative system. For more flexible variants of the aircraft, it was observed that the aircraft was far too flexible to support itself in steady flight resulting in a high occurrence of numerical convergence issues.

### 4.2.3 Limitations

While the proposed method has significant advantages over the linear Nastran SOL144, it has some limitations which need to be considered when interpreting the results from the method. The first limitation is related to the aerodynamics loads calculation. As the method used to calculate the aerodynamic loads on the aircraft uses Nastran SOL144, the aerodynamics are calculated using linearized potential theory [36]. As a result, the loads obtained when local wing twist angles are close to stall may not be representative of the physical loads exerted on the aircraft structure. The second limitation of the proposed method is that it is only applicable to static aeroelastic loads calculation. Despite aeroelasticity inherently being a dynamic process, inertial effects are ignored as the process can be deemed quasi-static, due to the slow-moving nature of the flight conditions studied.

### 4.3 Results

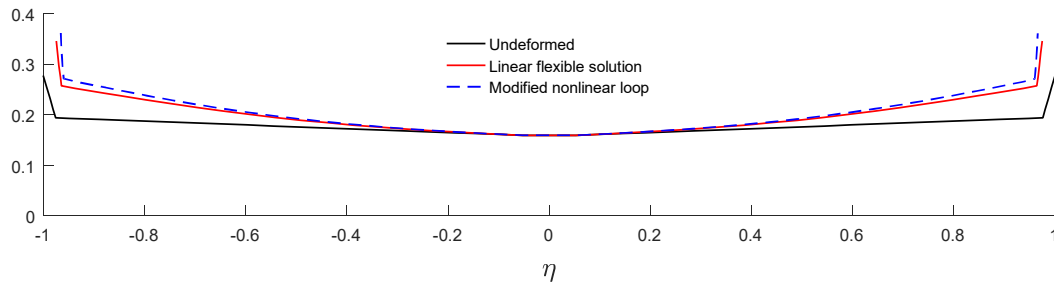


Figure 17: Displaced wing profile comparison between linear SOL 144 and nonlinear iterative method.  
Deformation has been magnified  $\times 3$

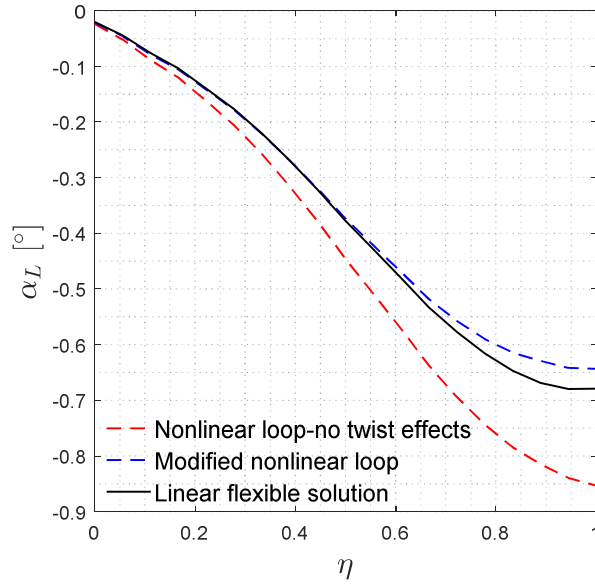


Figure 18: Comparison of local angle of attack,  $\alpha_L$ , along wingspan for linear and nonlinear methods

#### 4.3.1 Steady flight conditions

In this section, critical wing loads from the nonlinear methodology, with and without the effect of wing twist, are presented for the relatively stiff baseline aircraft stick model. This can be seen in Figure 17, which depicts the wing displacements under steady flight conditions for the linear and modified nonlinear methods, where  $\eta$  is the normalized position along the wing-span. The displacements have been scaled by a factor of three to help visualize them more clearly. The unscaled wing tip displacement in the steady flight conditions is 2.1% and 2.5% of the wing length for the linear and nonlinear aeroelastic solutions respectively, justifying our claim about the stiffness of the structure.

When the modified iterative method presented in this section is compared to the method implemented in [9], it can be seen that the inclusion of the wing twist into the iterative procedure brings it much closer to a linear flexible aeroelasticity analysis for a stiff

airframe. The variation of local angle of attack along the wingspan is shown in Figure 18, and the results for out of plane bending, out of plane shear, and wing torsional loads along the wing span are presented in Figure 19, Figure 20, and Figure 21. It can also be seen that the primary loads that are overestimated by the exclusion of wing twist in previous nonlinear iterative methodologies are the out of plane bending and shear loads, while torsional loads are largely unaffected. The loads from the nonlinear loop without twist effects, shown in Figure 19 and Figure 20, are significantly affected by the inclusion of geometrically nonlinear effects. This results in the root out of plane bending moment and shear forces being 12% and 7% higher than the loads calculated using linear aeroelastic methods, respectively. The inclusion of wing twisting effects into the loads predicted by the nonlinear methodology brings the difference in out of plane shear and bending moment to less than 2% along the entire wingspan. The root torque, shown in Figure 21, is 2% and 3% higher than the loads obtained from the linear method. The change in loads between the two nonlinear methodologies is attributed to the change in the lift distribution across the wingspan as the effects of downwash are taken into consideration.

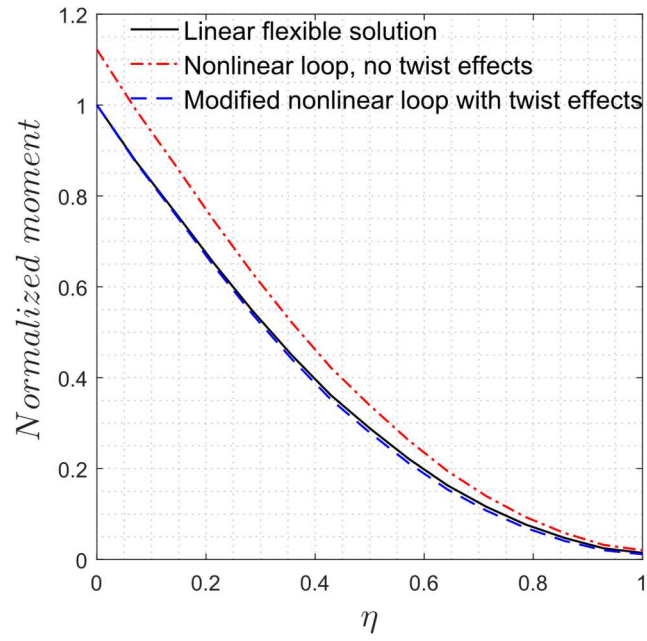


Figure 19: Comparison of out of plane bending moment along wingspan for linear and nonlinear methods

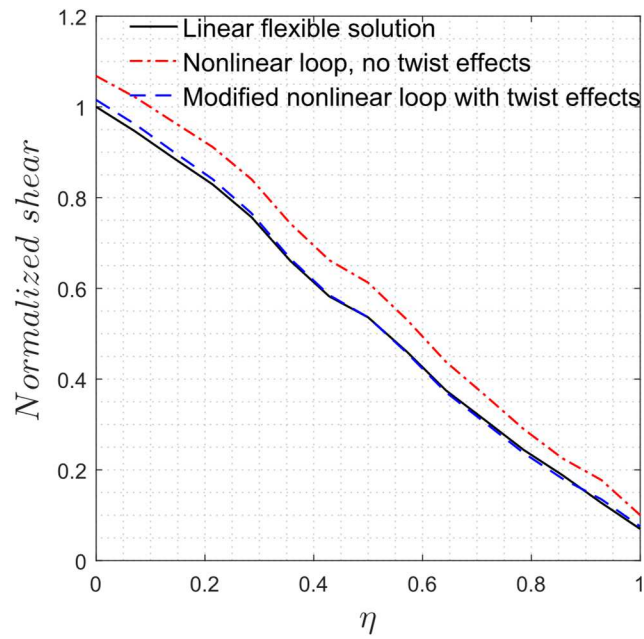


Figure 20: Comparison of out of plane shear force along wingspan for linear and nonlinear methods

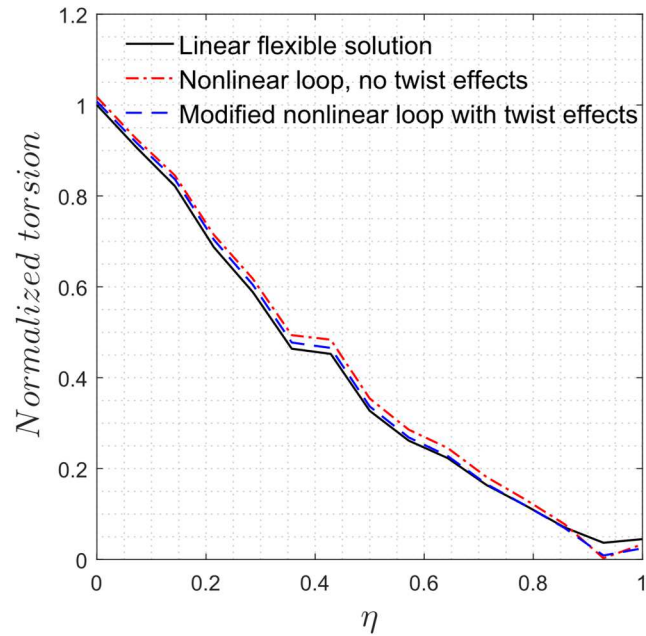


Figure 21: Comparison of twisting moment along wingspan for linear and nonlinear methods

To validate the nonlinear methodology proposed in this section, a structurally nonlinear aeroelastic analysis was performed using ASWING [47].

ASWING, developed by Mark Drela at the Massachusetts Institute of Technology, is a program for the prediction of static and transient loads and deformations of aircraft with flexible surfaces and fuselage beams using the geometrically nonlinear Bernoulli-Euler beam representation, proposed by Minguet [75], for all the airframe beam elements.

To perform this comparison, the Nastran format of the baseline aircraft, along with the aerodynamics, was converted into the ASWING format, and the analysis run under the same flight conditions as in Table 4. The results, shown in Figure 22 and Figure 23, demonstrate a good agreement between the two methods, benchmarking the methodology developed in this thesis.

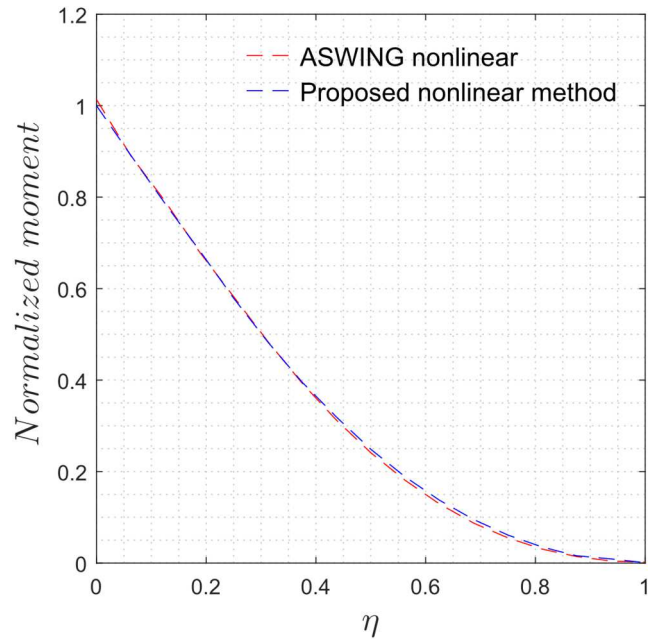


Figure 22: Comparison of out of plane bending moment along wingspan between ASWING and the modified nonlinear iterative method

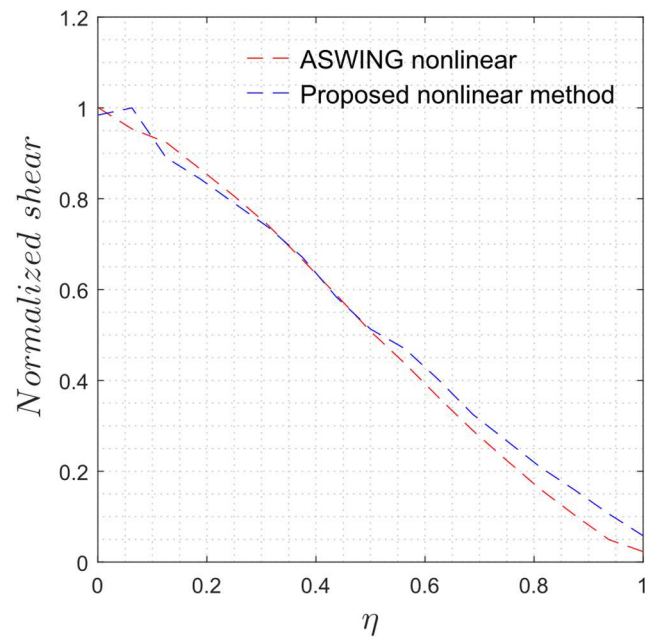


Figure 23: Comparison of out of plane shear force along wingspan between ASWING and the modified nonlinear iterative method

Overall, the modified nonlinear methodology results agree with the linear loads for the baseline aircraft stick, which is considered to be relatively stiff. The difference in the loads

between the nonlinear methodologies are significant as the out of plane loads calculated by the modified nonlinear methodology are lower than the unmodified loop. This is a result of the change in angle of attack along the outer edges of the wingspan, as shown in Figure 18, which is not considered in the original iterative method [9]. As such, the rest of the results will be presented using the modified nonlinear methodology which includes twist effects.

#### 4.3.2 Variation of root angle of attack

The following results are presented for the case when the root angle of attack,  $\alpha_0$ , of the aircraft wing is increased linearly from 0 to 10 degrees. The angle of attack is changed by using a Direct Matrix Input to change the downwash angle at each of the aerodynamic panels of the wing, to implement an effective change in  $\alpha_0$ . The comparison between the loads at the wing root are shown in Figure 23, Figure 24, and Figure 25.

With a root angle of attack of 0 degrees, the out of plane loads along the wing are very close to values obtained from the linear method. This is due to the fact that the aircraft is relatively stiff. As  $\alpha_0$  increases, the loads obtained from both solutions increase, but the loads from the nonlinear solution do not increase as much as the linear loads, indicating that the inclusion of the effect of geometric nonlinearities has the effect of underestimating the loads at high root angles of attack. This is due to the fact that the lift produced by the outboard section of the wing reduces with the increased deformation, resulting in reduced out of plane moment and shear force at the wing root.

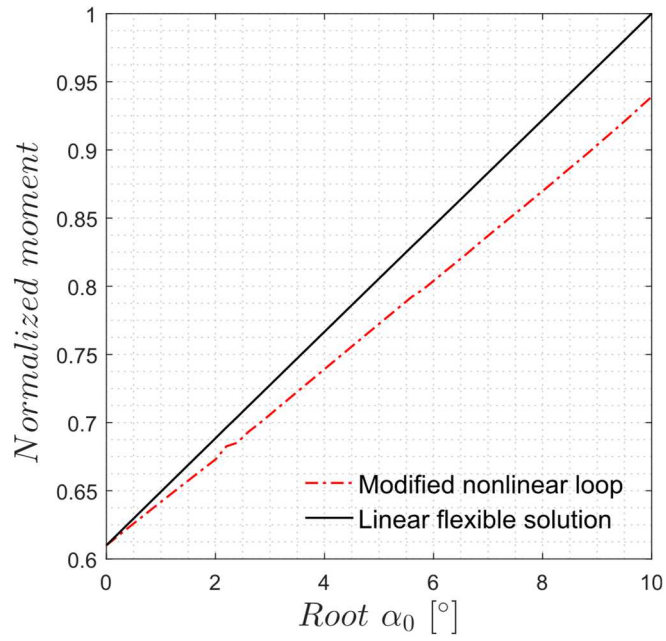


Figure 24: Comparison of out of plane bending moment at wing root, for linear and iterative nonlinear aeroelastic solution methods

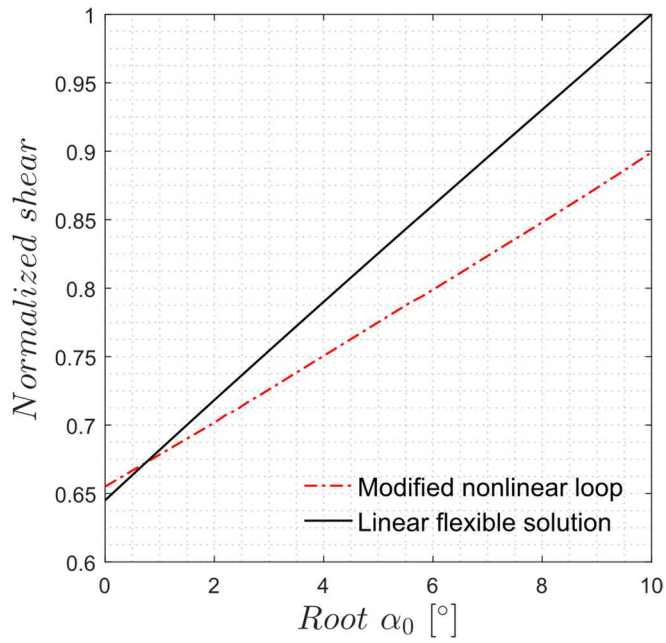


Figure 25: Comparison of out of plane shear force at wing root, for linear and iterative nonlinear aeroelastic solution methods

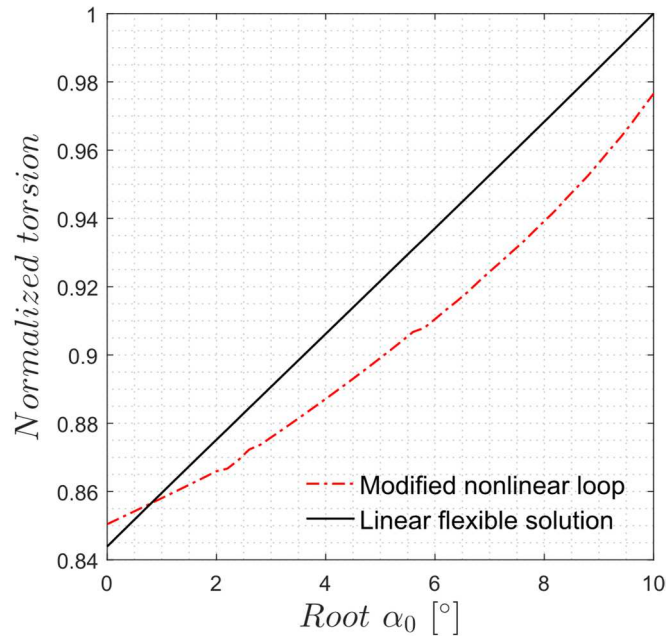


Figure 26: Comparison of torsional moment at wing root, for linear and iterative nonlinear aeroelastic solution methods

### 4.3.3 Parametric variation of equivalent beam dimensions

The variation of the equivalent beam dimensions, as described in Section 4.2.2.3, has the effect of varying the elemental stiffness along the wingspan. In this section, the effects of these variations on the root wing loads are presented and discussed.

#### 4.3.3.1 Effect on static aeroelastic loads

As shown in [76], the stiffness of the overall structure has a significant effect on the difference in the loads obtained through classical linear methods as well as nonlinear methods. However, the effect of changes to the individual structural parameters would give a more in depth look into the loads differences due to nonlinearities. The results presented in this section investigate the effects of varying the individual beam parameters on the significance of the nonlinearities using the modified nonlinear loop.

#### 4.3.3.1.1 Variation of In plane and Out of plane bending stiffness

In this section, the parametric beam dimensions, shown in Figure 11, are varied independently to create a range of test cases where the wing stiffness in both in-plane  $\hat{I}_{22}$ , and out of plane  $\hat{I}_{11}$ , vary. This allows the study of the effect of geometric nonlinearities in the structural calculations during an aeroelastic analysis.

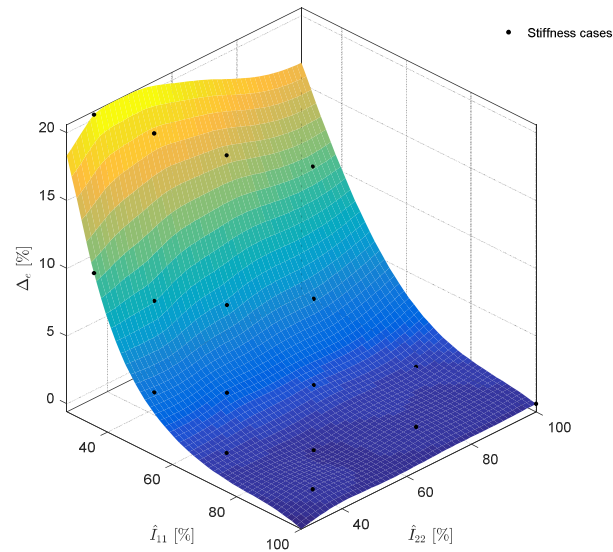


Figure 27: Increase in nonlinear load (out of plane bending moment) at the wing root,  $\Delta_e$ , compared to the corresponding linear load, with parametric variations of the in and out of plane stiffnesses,  $\hat{I}_{22}$ , and  $\hat{I}_{11}$ .

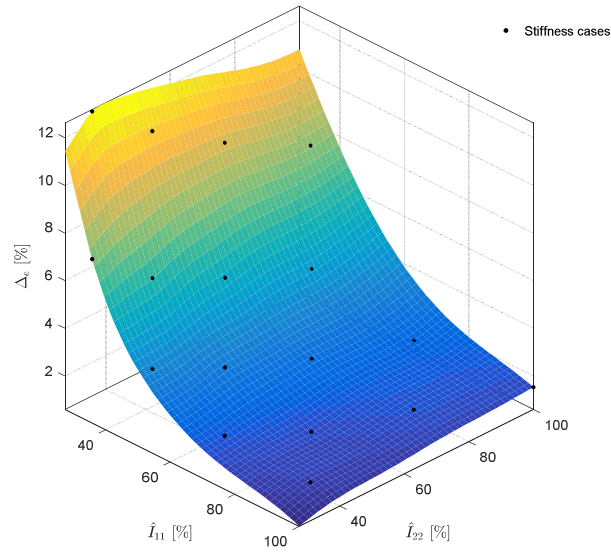


Figure 28: Increase in nonlinear load (out of plane shear force) at the wing root with parametric variations of the in and out of plane stiffnesses,  $\hat{I}_{22}$ , and  $\hat{I}_{11}$ .

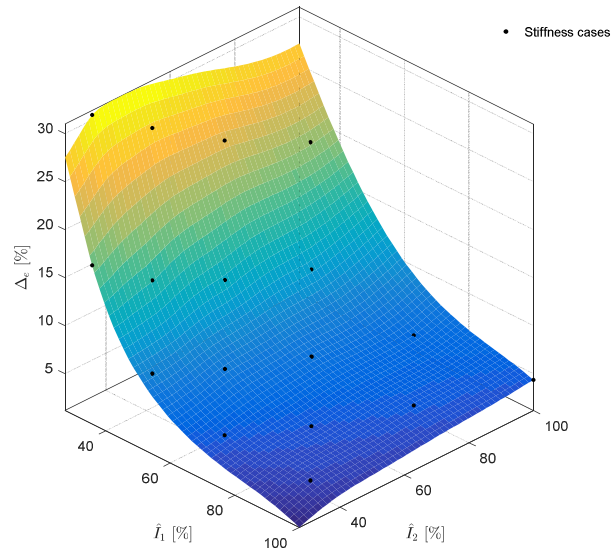


Figure 29: Increase in nonlinear load (torsional moment) at the wing root with parametric variations of the in and out of plane stiffnesses,  $\hat{I}_{22}$ , and  $\hat{I}_{11}$ .

The most significant factor observed to affect the nonlinearities is the variation of the flexural stiffness in the out of plane direction. This can be seen very clearly in Figure 27,

Figure 28, and Figure 29, where the increase in loads due to the inclusion of nonlinear effects can be seen to be only slightly affected by changes in the in plane stiffness of the wing. As such, the following analyses focus only on the variation of the out of plane stiffness,  $\hat{I}_{11}$ , keeping  $\hat{I}_{22}$  at the original reference value of 100%.

#### 4.3.3.1.2 Variation of Out of plane bending stiffness

In the previous section, it was found that the variation of the in-plane stiffness,  $\hat{I}_{22}$ , had very little effect on the wing root loads. Therefore, going forward, the load cases going forward consist only of the out of plane stiffness,  $\hat{I}_{11}$ , being varied. The other structural properties follow the trends shown in Figure 16.

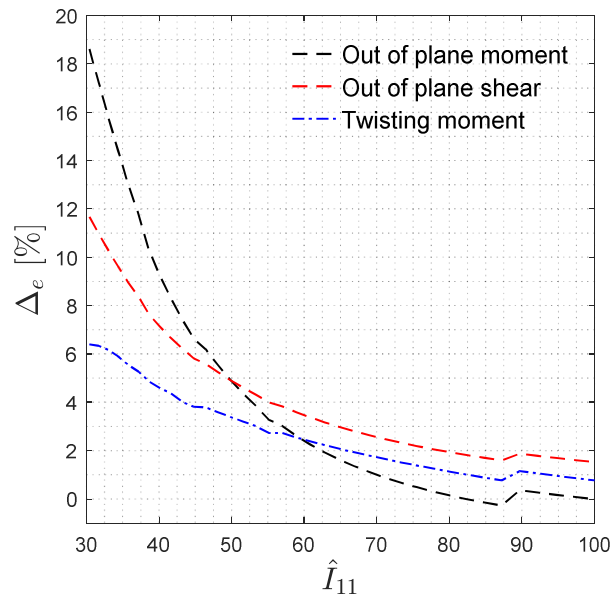


Figure 30: Nonlinear increase in loads at wing root,  $\Delta_e$ , as the out of plane stiffness,  $\hat{I}_{11}$ , is varied

Figure 30 shows the increment in loads at the wing root due to the inclusion of geometric nonlinearity,  $\Delta_e$ , as the out of plane stiffness,  $\hat{I}_{11}$ , is reduced from 100% to 30%. The increase in wing tip deflection due to the nonlinear solver is shown in Figure 31. A 1%

jump in the tip deflection can be seen when  $\hat{I}_{11}$  is at 90%, which is caused by the aerodynamic loads solver trimming the aircraft with a higher aileron deflection at this point, as shown in Figure 43.

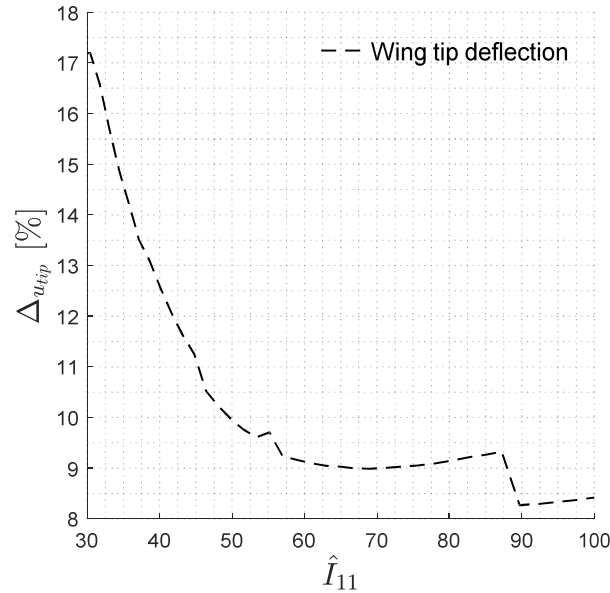


Figure 31: Increase in tip deflection,  $\Delta u_{tip}$ , due to nonlinearity, as the out of plane stiffness,  $\hat{I}_{11}$ , is varied. As shown in Figure 30, the out of plane bending moment and shear force at the wing root are highly dependent on the out of plane flexural stiffness, resulting in up to a 19% increase in the out of plane bending moment and a 12% increase in the out of plane shear force when the out of plane flexural stiffness is reduced to 30% of the original value, while the torsional moment is 6% higher.

For this particular airframe, the acceptable margin of error for this specific aircraft platform are 1%, 10%, 6% and 10%, for the out of plane bending moment, out of plane shear force, wing torsional moment, and wingtip deflection respectively. For this airframe, it is observed that the out of plane bending moment exceeds the acceptable load discrepancy criteria when the relative out of plane stiffness,  $\hat{I}_{11}$ , is lower than 70% of the reference

airframe. The threshold at which our allowable margin for the out of plane shear at the root is exceeded, is much lower, with  $\hat{I}_{11}$  around 35%, while the wing tip deformation threshold is crossed for  $\hat{I}_{11}$  values below 50%.

The distribution of the wing loads along the wingspan as the stiffness is varied, is shown in Figure 32, Figure 33, and Figure 34. The loads are obtained using the modified nonlinear iterative method and are normalized with respect to the root load for their corresponding linear load case. It is observed that the loads along the wingspan, vary uniformly when only the out of plane flexural stiffness is varied. The only significant difference can be seen in Figures Figure 33 and Figure 34, for the out of plane shear force, and torsional bending moment, respectively. It can be observed that there is a sharp spike in the loads near the wing tip. This is because of the loads exerted by the aileron becoming proportionally more significant to the wing loads as the overall magnitude of the loads decreasing with the reduced mass.

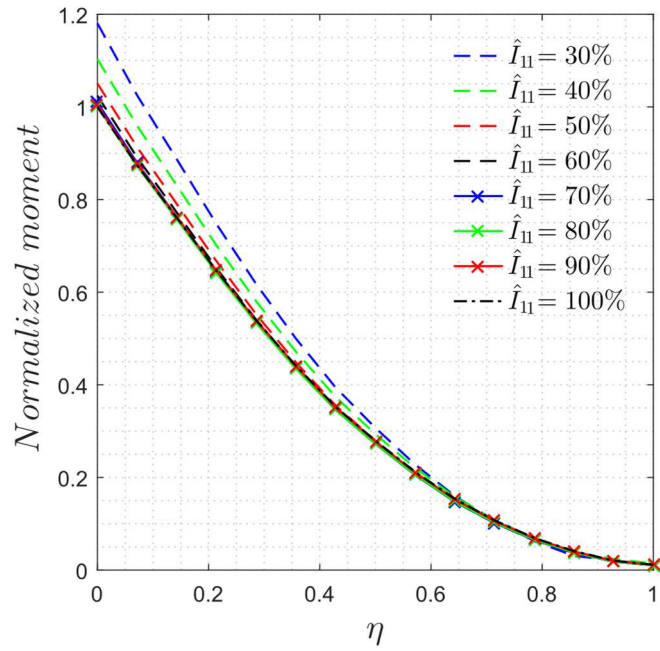


Figure 32: Normalized nonlinear out of plane bending moment across wingspan as stiffness varies.

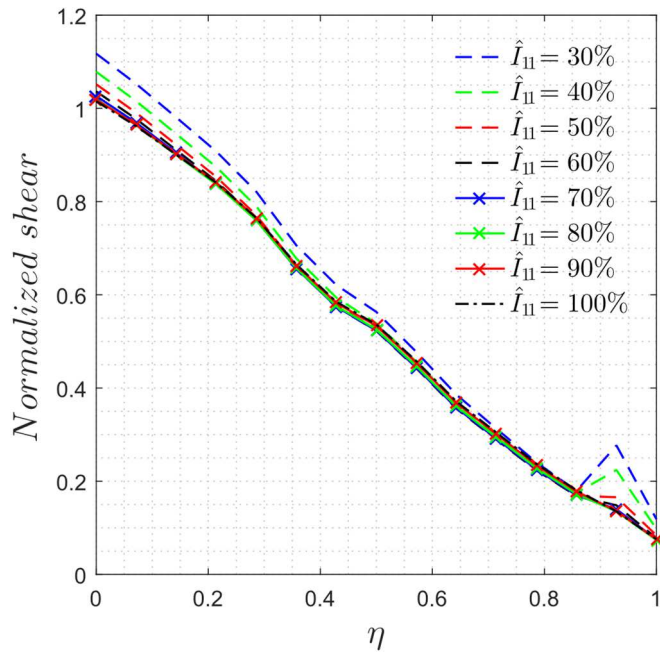


Figure 33: Normalized nonlinear out of plane shear force across wingspan as stiffness varies.

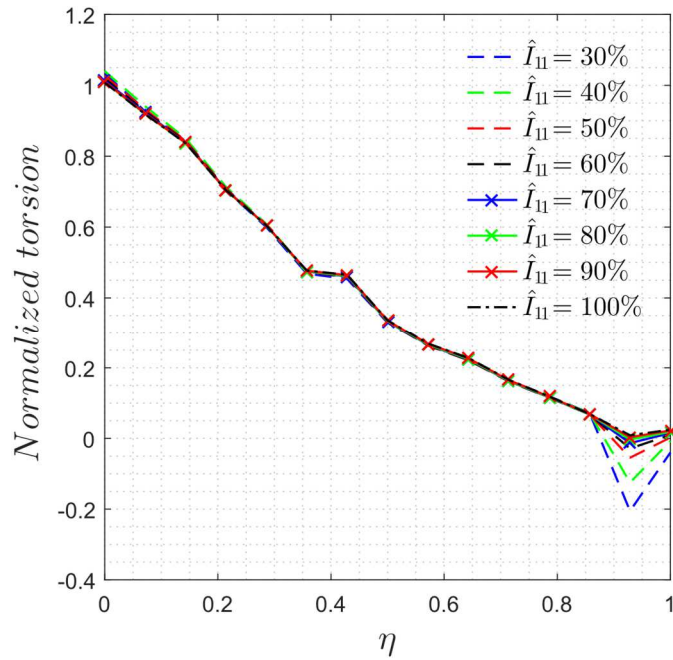


Figure 34: Normalized nonlinear torsional moment across wingspan as stiffness varies.

This overall reduction in the magnitude of the loads as the wings became lighter, and thus more flexible, can be seen in Figure 35, Figure 36, and Figure 37.

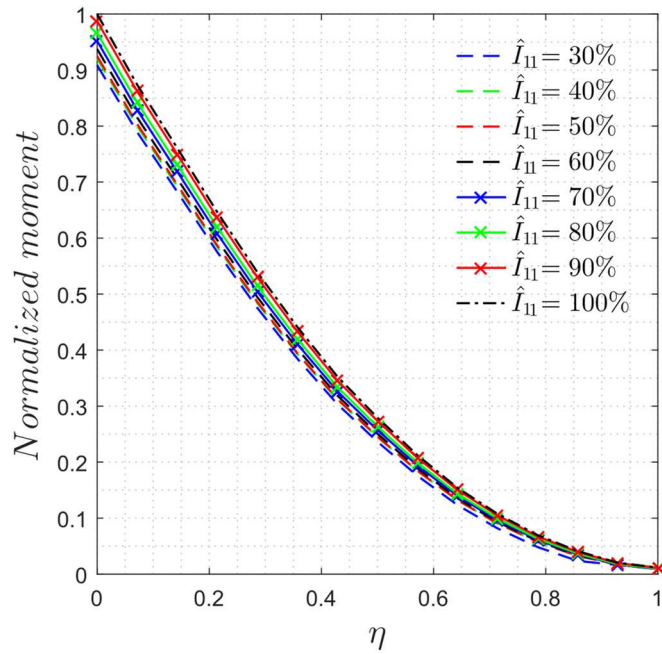


Figure 35: Normalized nonlinear out of plane bending moment across wingspan

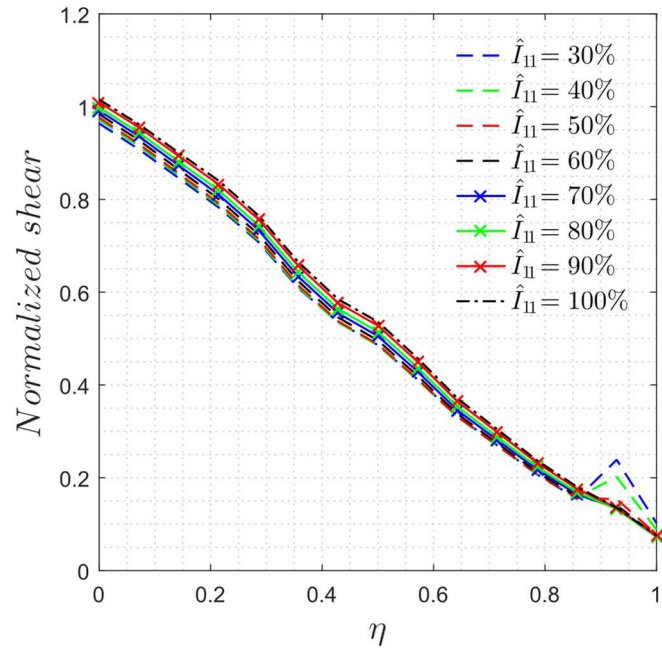


Figure 36: Normalized nonlinear out of plane shear force across wingspan

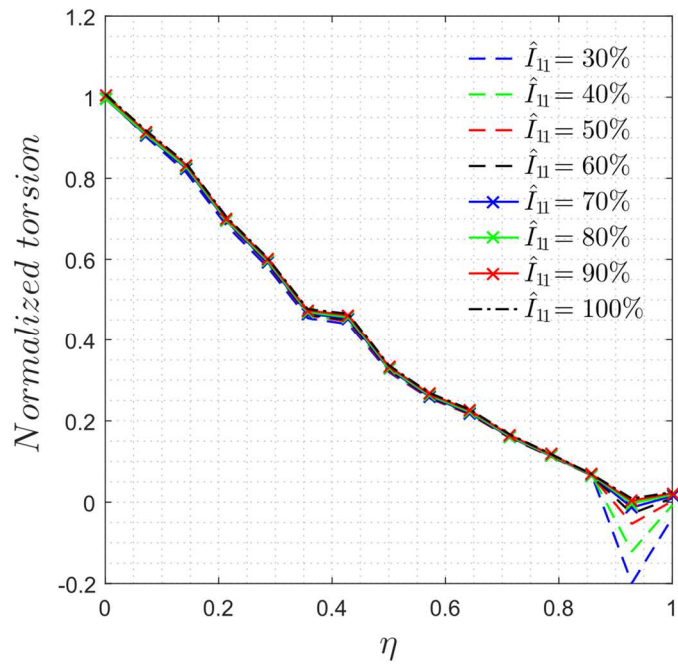


Figure 37: Normalized nonlinear torsional moment across wingspan

It is important to note that all the loads are now normalized with respect to the root load for the baseline load case. The linear load distribution is shown in Figure 38, Figure 39, and Figure 40.

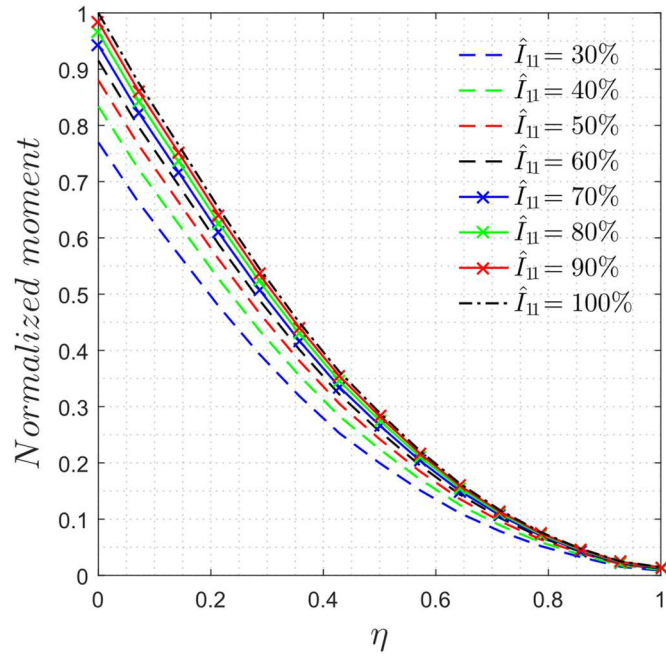


Figure 38: Normalized linear out of plane bending moment across wingspan

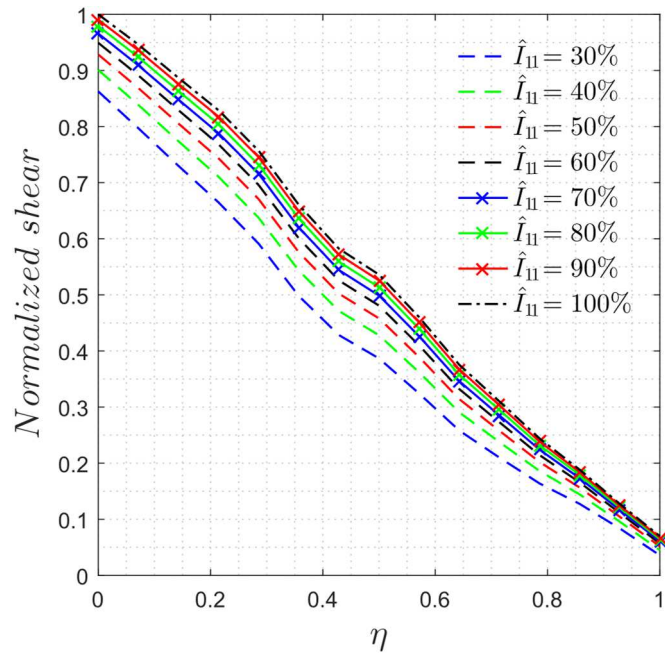


Figure 39: Normalized linear out of plane shear force across wingspan

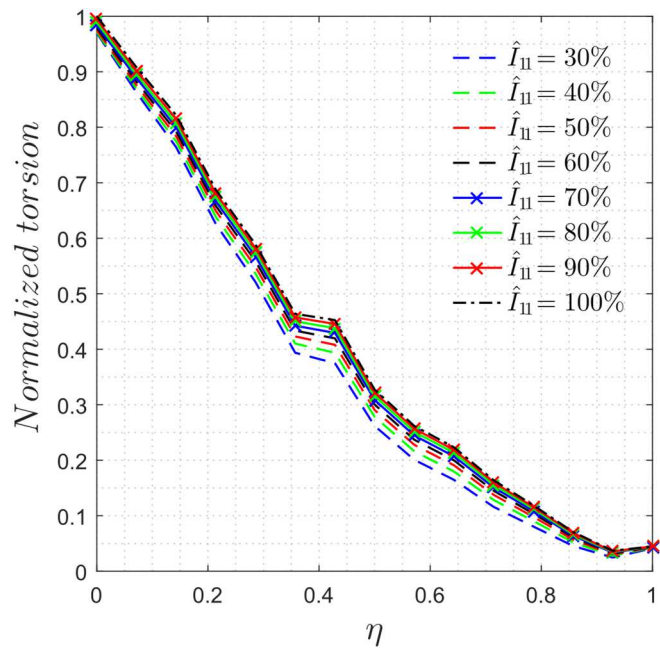


Figure 40: Normalized linear torsional bending moment across wingspan

As the structure of the aircraft is made more flexible, the magnitude of the loads reduces due to the corresponding reduction in mass. However, this reduction is less apparent in the nonlinear case due to the effects of large deformations nonlinearity.

#### 4.3.3.2 Effect on aircraft trimmed configuration

The change in the deformed structure has a significant effect on the trimming configuration of the aircraft, which can be observed in the change in trimmed angle of attack and elevator deflection. Figure 41, Figure 42, and Figure 43 plot the trends of the aircraft trim variables as the flexibility increases.

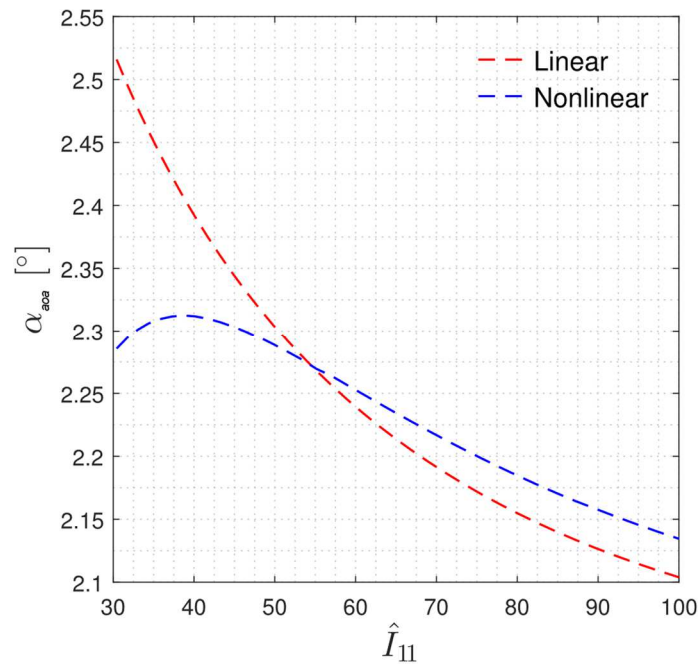


Figure 41: Variation of angle of attack,  $\alpha_{aoa}$ , with wing stiffness

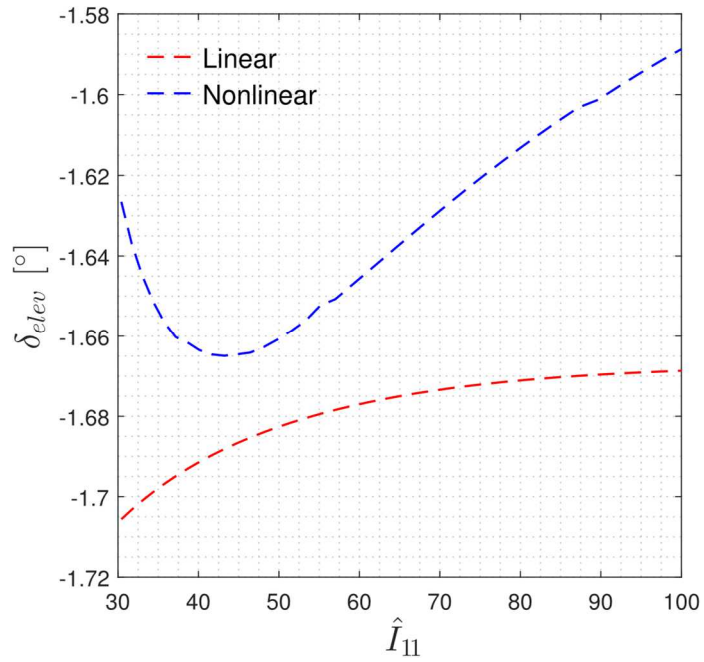


Figure 42: Variation of elevator deflection,  $\delta_{elev}$ , with wing stiffness

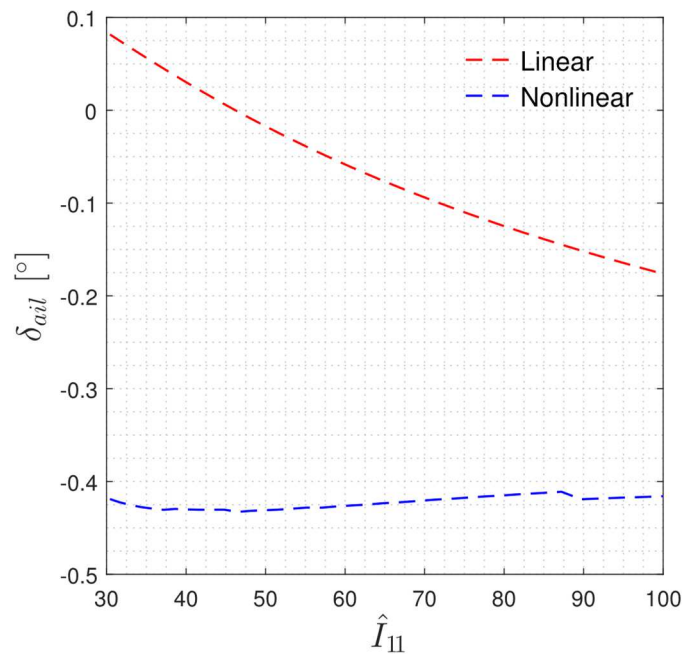


Figure 43: Variation of aileron deflection,  $\delta_{ail}$ , with wing stiffness

The angle of attack, elevator deflection, and aileron deflection are shown for both the linear and nonlinear methods used. Of interest to note are the angle of attack and elevator deflection plots, shown in Figure 41 and Figure 42, which show a local change in behaviour at stiffnesses below 50% of the original structure. The aileron deflection remains relatively constant when the nonlinear methodology is used. However, the aileron deflection does induce significant torsional and shear loads in the nonlinear method, as discussed in the previous section, and shown in Figures Figure 33 and Figure 34.

#### **4.4 Chapter Summary**

The work presented in this Chapter highlights the importance of considering geometrically nonlinear effects during static aeroelastic analyses. The modified iterative method was shown to produce high fidelity loads calculation on par with custom nonlinear aeroelastic codes such as ASWING. The logical progression is to study the effects of including geometrically nonlinear structural formulations on dynamic aircraft loads, which will be explored in the following Chapter.

## 5 Dynamic Aeroelasticity: Parametric Case Study

The effects of geometrical nonlinearities on the aeroelastic loads of aircraft in static flight conditions has been studied quite thoroughly by several authors [9], [59], [77], [78]. Displacement based geometrically nonlinear beam models has been used by Drela and incorporated in ASWING software [79], to model nonlinear behavior of airframes. Using a mixed formulation beam models, the nonlinear flutter performance of aircraft has been investigated by Patil et al [80], and Tang [81]. Ribiero used the strain based beam model, developed originally by Brown and Shearer [31], [82], to create a fully nonlinear aeroelastic solver, namely, AeroFlex [59]. More recently, Castellani et al. [9] used MSC Nastran [36] to create an ad-hoc nonlinear static aeroelastic solver [9], [77], which was improved upon by the author, detailed in the previous section [1].

In the previous section, transient, or dynamic terms in the equations of motion were ignored, as the flight conditions were assumed to be steady, and the aircraft in a state of equilibrium. However, this is not always an accurate assessment, as aircraft can have flight conditions with load conditions which are highly dependant on time.

In general, the behavior of aircraft structure under dynamic loading conditions, such as gust turbulences, is not as well studied in the geometrically nonlinear sense. In this section, the aim is to provide readers with an insight into the effects of airframe conceptual design changes on the dynamic aeroelastic loads, and strategies of conservative dynamic loads estimation are discussed.

The formulation of the gust model, and the methodology used will be presented. Following that, the results of the sensitivity analysis into the importance of design parameters on nonlinear loads will be discussed.

In this section, the same aircraft model from the previous case study is used to investigate the effect of including geometrical nonlinearities into a dynamic gust simulation of the aircraft.

## **5.1 Theoretical Framework**

Most commercial aeroelastic solvers, such as MSC Nastran SOL 144/146, use linear structural mechanics coupled linear panel method aerodynamics to calculate the aeroelastic behaviour of an aircraft [36]. However, as shown in the previous section, effects of geometric nonlinearity can have a significant impact on the loads calculated at critical points of the aircraft structure, such as the wing root.

In this section, ASWING will be used as the nonlinear dynamic aeroelastic tool, due to alternatives such as 3D FEM-CFD fluid structure analyses being extremely computationally expensive in terms of memory resources and time.

### **5.1.1 Sensitivity Analysis**

The sensitivity of the wing root load, namely the out of plane bending moment, to a number of aircraft conceptual design parameters is investigated. The design parameters are varied with respect to a baseline aircraft structure, and the corresponding linear and nonlinear loads are calculated.

Sensitivity of aeroelastic loads to variation in independent design parameter is determined with respect to the local derivative of the output using finite difference. This can be calculated as:

$$\zeta|_{\Delta_0} = \left. \frac{\partial \Delta_e}{\partial \Delta} \right|_{\Delta_0} \quad (145)$$

where  $\zeta$  is the local sensitivity,  $\Delta_e$  is the increment in loads due to the effect of geometric nonlinearity,  $\Delta$  is the configuration of an arbitrary structural parameter at the current state, and  $\Delta_0$  is the value of the parameter in the aircraft structure's baseline configuration.

To evaluate Equation 145 and determine the sensitivity of a system with respect to a given configuration, the local derivative of the nonlinear increment is calculated numerically using either a backward-difference or central-difference gradient operator, depending on the design space of the parameter of interest [24].

### 5.1.2 Mass and stiffness variation

To vary the stiffness of the wing beam elements, each element is parametrized into a thin-walled rectangular box, as shown Figure 44, where a primary assumption is that the thickness of the wall is much less than the other dimensions.

The height of the thin-walled box is then varied from 50% to 100% of the baseline value. The resulting new box dimensions are used to recalculate the wing element structural properties.

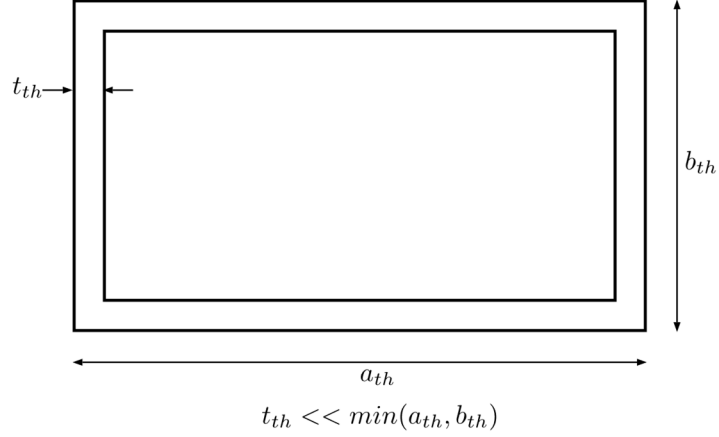


Figure 44: Dimensioning of thin-walled beam used to parametrize wing elements

The cross-sectional area,  $A$ , of the beam is simply calculated as:

$$A = 2t_{th}(a_{th} + b_{th}) \quad (146)$$

and the out-of-plane, in-plane, and polar moments of area are given as:

$$I_{11} = \frac{a_{th}t_{th}b_{th}^2}{3} \quad (147)$$

$$I_{22} = \frac{a_{th}^2t_{th}b_{th}}{3} \quad (148)$$

$$J = \frac{2t_{th}^2(a_{th} - t_{th})^2(b_{th} - t_{th})^2}{b_{th}t_{th} + a_{th}t_{th} - 2t_{th}^2} \quad (149)$$

where  $a_{th}$  is the width of the beam,  $b_{th}$  is the height and  $t_{th}$  is the thickness of the wall.

$I_{11}$  and  $I_{22}$  are the second moments of area, and  $J$  is the polar moment of area. The  $th$  subscript is used due to the thin-walled beam assumption.

As the length of the beam element is fixed, its mass is calculated proportionally to the beam cross section area as:

$$M_{new} = \frac{A_{new}}{A_{base}} M_{base} \quad (150)$$

where the baseline elemental mass and cross-sectional area are represented by the subscript "base" and the modified parameters by "new".

The resulting mass and stiffness distributions are shown in Figure 45 where the normalized stiffness and mass values are expressed as function in the out-of-plane stiffness of the wing.

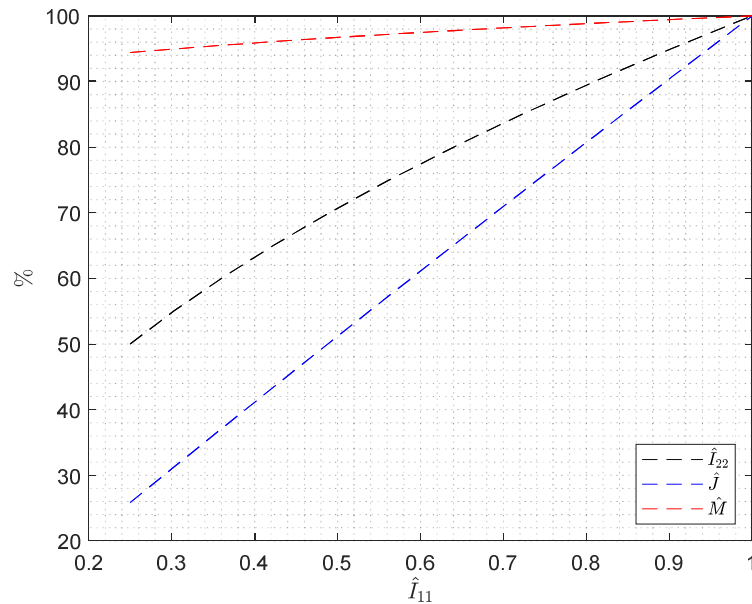


Figure 45: Variation of the in-plane stiffness, torsional stiffness, and element mass, as a function of out of plane stiffness

For the purposes of this case study, a stick model of a Bombardier Aircraft platform is used, as a 3D Global Finite Element (GFEM) model would be computationally expensive to run. Several methods of airframe model order reduction are available in the literature [10]–[14]. In this study, the unitary loading method is employed for the development of the airframe condensed stick model [12], [15], which has been described and validated in Section 4.2.2

### 5.1.3 ASWING beam model

The nonlinear aeroelastic software employed for this work, ASWING, uses the Minguet nonlinear beam model [75]. ASWING is chosen due to its displacement-based beam formulation, as well as the fact that a previous study conducted by the author validates the results of ASWING for nonlinear aeroelastic loads [1]. The equations of motion are reproduced below.

Given a one-dimensional beam with warping effects ignored, the position along the beam can be represented as a single coordinate along the beam length,  $s$ . For any point along the beam, the relationship between the beam local undeformed frame  $\mathbf{b}$  and global reference frame  $\mathbf{A}$  is given as

$$\mathbf{p}_b = \underline{\underline{C^{bA}}} \cdot \mathbf{p}_A \quad (151)$$

where  $\mathbf{p}$  is a vector representing the bases for the corresponding frames of reference, and  $\underline{\underline{C^{bA}}}$  is the transformation matrix from the global to the local frame, given in terms of Euler angles.

Assuming the beam has arbitrary curvature and twist, moving an infinitesimal distance,  $ds$ , along the beam reference line rotates the local reference frame as follows:

$$\frac{d\underline{\underline{C^{bA}}}}{ds} = [\boldsymbol{\kappa}] \underline{\underline{C^{bA}}} \quad (152)$$

where the curvature matrix is given by

$$[\boldsymbol{\kappa}] = \begin{bmatrix} 0 & \kappa_z & -\kappa_y \\ -\kappa_z & 0 & \kappa_x \\ \kappa_y & -\kappa_x & 0 \end{bmatrix} \quad (153)$$

and  $\kappa_x, \kappa_y, \kappa_z$  are the curvatures of the beam about the beam axes.

The transformation matrix is given by pre-multiplication of the 3 individual rotations from the global to the local reference frame.

$$\underline{C}^{bA} = \begin{bmatrix} 1 & 0 & 0 \\ 0 & \cos \theta_1 & \sin \theta_1 \\ 0 & -\sin \theta_1 & \cos \theta_1 \end{bmatrix} \begin{bmatrix} \cos \theta_2 & 0 & \sin \theta_2 \\ 0 & 1 & 0 \\ -\sin \theta_2 & 0 & \cos \theta_2 \end{bmatrix} \begin{bmatrix} \cos \theta_3 & \sin \theta_3 & 0 \\ -\sin \theta_3 & \cos \theta_3 & 0 \\ 0 & 0 & 1 \end{bmatrix} \quad (154)$$

Solving for the curvatures in Equation 153, the following expressions are obtained for the curvatures in terms of the Euler angles.

$$\begin{aligned} \kappa_x &= \frac{d\theta_1}{ds} + \sin \theta_1 \frac{d\theta_3}{ds} \\ \kappa_y &= -\cos \theta_1 \frac{d\theta_2}{ds} + \sin \theta_1 \cos \theta_2 \frac{d\theta_3}{ds} \\ \kappa_z &= \sin \theta_1 \frac{d\theta_2}{ds} + \cos \theta_1 \cos \theta_2 \frac{d\theta_3}{ds} \end{aligned} \quad (155)$$

The equations of motion for a differential beam element are then derived by solving for the equilibrium of a beam element in the deformed position. The beam internal stresses are defined by the local beam force,  $F_{int}$ , and moment,  $M_{int}$ , vectors.

The force equilibrium equation is given as:

$$\begin{aligned} & [\underline{C}^{bA} + d\underline{C}^{bA}]^T (F_{int} + dF_{int}) - [\underline{C}^{bA}]^T F_{int} + [\underline{C}^{bA}]^T F_b ds + F_A ds \\ & = 0 \end{aligned} \quad (156)$$

and the corresponding elemental moment equation is given as

$$\begin{aligned}
& [\underline{C}^{bA} + d\underline{C}^{bA}]^T (M_{int} + dM_{int}) - [\underline{C}^{bA}]^T M_{int} \\
& + [\underline{C}^{bA}]^T (e_1 \times (F_{int} + dF_{int})) + [\underline{C}^{bA}]^T M_b ds + M_A ds \quad (157) \\
& = 0
\end{aligned}$$

where  $F_b$  and  $M_b$  are, respectively, the external force and moment vectors applied in the beam local reference frame, such as aerodynamic loads, while  $F_A$  and  $M_A$  are, respectively, the applied loads in the global reference frame.  $e_1$  is a vector tangent to the differential beam element where  $e_1 = [ds, 0, 0]^T$ .

The strain-displacement relations are then obtained by inverting Equations 155 to obtain the following relations relating rotations to curvatures.

$$\begin{aligned}
\frac{d\theta_1}{ds} &= \kappa_x - \sin \theta_1 \tan \theta_2 \kappa_y - \cos \theta_1 \tan \theta_2 \kappa_z \\
\frac{d\theta_2}{ds} &= -\cos \theta_1 \kappa_y + \sin \theta_1 \kappa_z \\
\frac{d\theta_3}{ds} &= \frac{\sin \theta_1}{\cos \theta_2} \kappa_y + \frac{\cos \theta_1}{\cos \theta_2} \kappa_z
\end{aligned} \quad (158)$$

The translation analogues are given as:

$$\begin{aligned}
\frac{dx}{ds} &= (1 + \varepsilon) \cos \theta_2 \cos \theta_3 \\
\frac{dy}{ds} &= (1 + \varepsilon) \cos \theta_2 \sin \theta_3 \\
\frac{dz}{ds} &= (1 + \varepsilon) \sin \theta_2
\end{aligned} \quad (159)$$

where  $\varepsilon$  is the extensional strain along the beam, and  $x, y, z$  are the deformed beam coordinates.

The final relationships are the stress-strain relations which are given by the classical linear relationships as follows

$$\begin{Bmatrix} F \\ M \end{Bmatrix} = S \begin{Bmatrix} \gamma \\ \kappa \end{Bmatrix} \quad (160)$$

where  $S$  is the sectional stiffness matrix,  $\gamma$  are the extensional and transverse strains, and  $\kappa$  are the curvatures. In the absence of materials with coupling behaviours such as composites, the sectional stiffness matrix can be simply given as

$$S = \begin{bmatrix} EA & 0 & 0 & 0 & 0 & 0 \\ 0 & GK_2 & 0 & 0 & 0 & 0 \\ 0 & 0 & GK_3 & 0 & 0 & 0 \\ 0 & 0 & 0 & GJ & 0 & 0 \\ 0 & 0 & 0 & 0 & EI_2 & 0 \\ 0 & 0 & 0 & 0 & 0 & EI_3 \end{bmatrix} \quad (161)$$

where  $GK_2$  and  $GK_3$  are the shear stiffness,  $EI_2$  and  $EI_3$  are the bending stiffness, and  $EA$  and  $GJ$  are the extensional and torsional stiffness, respectively.

Equations 156 - 159 form a system of 12 nonlinear first order differential equations, which can be solved simultaneously using a finite difference method [75].

#### 5.1.4 Aeroelastic model

The following subsection repeats the aeroelastic model from Section 4.1.3, and expands on the equations of motion required for linear dynamic aeroelasticity.

In a standard aeroelastic analysis, the aerodynamic pressure,  $\hat{f}_{aero}$ , is related to the downwash,  $\hat{w}$ , at the aerodynamic surfaces as:

$$\hat{f}_{aero} = q_{dyn} \mathbf{A}_{AIC}^{-1} \hat{w} \quad (162)$$

where  $q_{dyn}$  is the dynamic pressure of the flight condition, and the Aerodynamic Influence Coefficient (AIC) matrix relates the downwash to the aerodynamic pressure.

The downwash is given as:

$$\hat{w} = \mathbf{D} \mathbf{U}_{aero} + \hat{w}^g \quad (163)$$

The Aerodynamic Influence Coefficient (AIC) matrix is given by  $\mathbf{A}_{AIC}$  and  $\mathbf{D}$  is the matrix relating the displacements of the aerodynamic panels,  $\mathbf{U}_{aero}$ , to the downwash.

The total aerodynamic force vector of the structure,  $\hat{L}$ , can then be given as:

$$\hat{L} = \mathbf{S} \hat{f}_{aero} + \mathbf{F}_{rig} \quad (164)$$

where  $\mathbf{S}$  is a matrix relating nodal pressures to nodal forces, and  $\mathbf{F}_{rig}$  is a vector of rigid applied loads on the structure, such as engine loads and point loads.

The force-displacement relationship for a static structure is given by:

$$\mathbf{R} = \mathbf{K}_{glob} \mathbf{U} \quad (165)$$

where  $\mathbf{R}$  is the total load on the structure,  $\mathbf{U}$  is the global displacement vector due to the applied load, and  $\mathbf{K}_{glob}$  is the global tangent stiffness matrix of the structure.

Equating the RHS of Equations 119 and 120, the expression for an aeroelastic system at equilibrium is given as:

$$\mathbf{S} \hat{f}_{aero} + \mathbf{F}_{rig} = \mathbf{K}_{glob} \mathbf{U} \quad (166)$$

Substituting Equations 117 and 118 into the above expression yield the following relationship

$$\frac{qSA_{AIC}^{-1}}{q} [\mathbf{D}\mathbf{U} + \hat{w}^g] + \mathbf{F}_{rig} = \mathbf{K}_{glob}\mathbf{U} \quad (167)$$

MSC Nastran [36] is used for the linear aeroelastic analysis. Here, the dynamic aeroelastic equation of motion is given as:

$$[-\mathbf{M}_m\omega^2 + i\mathbf{C}_m\omega + \mathbf{K}_m - q_{dyn}\mathbf{Q}_m]\mathbf{X}_m = \mathbf{R}(\omega) \quad (168)$$

where  $\mathbf{M}_m$ ,  $\mathbf{C}_m$  and  $\mathbf{K}_m$  are the modal mass, damping and stiffness matrices, respectively,  $\mathbf{Q}_m$  is a matrix relating the nodal downwash to the corresponding modal forces at the nodes, and  $\mathbf{X}_m$  is a vector of generalized modal coordinates.  $\omega$  is the frequency around which the system is reduced, and  $i$  is a complex number

Equation 168 is solved with respect to an equilibrium condition, which in this work is taken to be a 1G steady flight condition. The physical solution is then obtained by taking the inverse Fourier Transform of the modal response, as follows:

$$\mathbf{U}(t) = \int_{-\infty}^{\infty} \mathbf{H}(\omega)\mathbf{R}(\omega)e^{i\omega t} d\omega \quad (169)$$

where the transfer function  $\mathbf{H}(\omega)$  is given as

$$\mathbf{H}(\omega) = \frac{1}{[-\mathbf{M}_m\omega^2 + i\mathbf{C}_m\omega + \mathbf{K}_m - q_{dyn}\mathbf{Q}_m]} \quad (170)$$

### 5.1.5 Aerodynamic Model

Both ASWING and MSC Nastran use panel method aerodynamics to calculate the aerodynamic loads exerted on the aircraft structure [47], namely the Doublet Lattice Method [36], [70], [71]. This method is based on linearized potential flow theory, where a

line of potential doublets of unknown strength lie along the quarter-chord of each aerodynamic panel. Given  $n$  aerodynamic boxes with a constant force per unit length along the quarter-chord line,  $\mathbf{f}$ , the strength of a doublet line segment  $j$  is given as

$$\frac{\mathbf{f}_j}{4\pi\rho_{air}} \int L_j ds \quad (171)$$

where  $L_j$  is the length of the doublet line,  $ds$  is an increment along the line, and  $\rho_{air}$  is the density of air. The total downwash at any point on the aerodynamic surface  $(x_i, s_i)$  can then be written as the sum of all the downwash due to all the doublets on the surface.

$$\bar{w}(x_i, s_i) = \sum_{j=1}^n \left( \frac{\mathbf{f}_j}{4\pi\rho_{air}} U_{free}^2 \right) \int \hat{\Gamma} ds \quad (172)$$

where  $U_{free}$  is the freestream velocity of the airflow across the panels, and  $\hat{\Gamma}$  is the kernel function for a nonplanar surface [72].

When Equation 128 is applied to all the downwash points, the force per unit length along the quarter-chords of the boxes can be determined, and thus, the average pressure,  $f_{box}$ , on each aerodynamic box is written as

$$f_{box_i} = \frac{\mathbf{f}_i}{\Delta x_j \cos \lambda_j} \quad (173)$$

where  $\Delta x_j$  is the average chord of the  $j$ th box, and  $\lambda_j$  is the sweep angle of the doublet line on the box. Given the  $j$ th index of doublet lines and  $i$ th index of the downwash points, Equation 128 can be re-written as

$$\bar{w} = \sum_{j=1}^n D_{ij} p_j \quad (174)$$

where  $D_{ij}$  are the elements of matrix  $\mathbf{D}$  in Equation 118, given as follows

$$\frac{\pi}{8} \Delta x_j \cos \lambda_j \int \hat{\Gamma} ds \quad (175)$$

Equation 118 represents the downwash acting on an aerodynamic panel. However, trimming the aircraft into a steady state condition often requires the use of aerodynamic degrees of freedom, such as angle of attack, rotation rates, and control surface deflections, to modify the net forces and moments acting on the structure, which can be incorporated into the expression for the downwash as follows:

$$\hat{w} = \mathbf{D}\mathbf{U} + \mathbf{D}_\sigma \hat{u}_\sigma + \hat{w}^g \quad (176)$$

where  $\mathbf{D}_\sigma$  is a matrix relating the aerodynamic degrees of freedom,  $\hat{u}_\sigma$ , to the downwash. All prior equations assume that the aerodynamic forces are applied directly to the structural nodes. However, due to differences in the meshing of aerodynamic panels and structural members, this is not always the case. This is because the aerodynamic panels are applied at the quarter-chord point of each aerodynamic box element, which is quite often much larger in number than the actual structural elements. The forces need to be coupled to the structural degrees of freedom of the airframe, which is achieved using a linear beam spline using an interpolation matrix.

$$\mathbf{U}_{aero} = \mathbf{G}_{spline} \mathbf{U}_{struct} \quad (177)$$

where  $\mathbf{G}_{spline}$  is the interpolation matrix relating the structural deflections  $\mathbf{U}_{struct}$ , to the aerodynamic nodal deflections  $\mathbf{U}_{aero}$

Imposing the condition that the virtual work performed by both deflections is identical, an expression for an arbitrary force transformation between the aerodynamic and structural nodes is given as follows

$$\mathbf{F}_{struct} = [\mathbf{G}_{spline}]^T \mathbf{F}_{aero} \quad (178)$$

where  $\mathbf{F}_{aero}$  is a vector of aerodynamic loads on aerodynamic nodes, and  $\mathbf{F}_{struct}$  are the resulting aerodynamic loads on structural nodes.

### 5.1.6 Discrete Gust Model

Discrete gust model is used in both the linear and nonlinear dynamic aeroelastic analyses. Unlike continuous disturbance models [83], in a discrete gust model, the disturbance is modeled as a single pulse of arbitrary shape and size. In this work, the 1 Minus Cosine (1MC) gust model is used as it more closely represents actual gust velocities in the atmosphere [84].

The vertical discrete gust velocity at a distance  $X$  into the gust profile is computed as:

$$U_{gust} = \frac{U_{ds}}{2} \left( 1 - \cos \left( \frac{2\pi X}{L_{gust}} \right) \right) \quad (179)$$

where  $L_{gust}$  and  $U_{ds}$  are gust length and gust design velocity given by:

$$U_{ds} = U_{ref} g_g \left( \frac{0.5L_{gust}}{350} \right)^{\frac{1}{6}} \quad (180)$$

$U_{ref}$  is the reference gust velocity, and  $g_g$  is the flight profile alleviation factor.

However, it must be noted that the aerodynamic models used in ASWING and MSC Nastran are not identical, and as such, will have slightly differing lift distributions across the wingspan of the aircraft, especially during dynamic gust encounters.

## 5.2 Case Study

The following section presents the details of the model used for the case study, as well as details about the parameters used in the sensitivity analysis. For the purposes of

this work, the gust design velocity,  $U_{ds} = 24 \text{ m/s}$ , and the gust length,  $L_{gust} = 30.5 \text{ ft}$  are considered.

A Bombardier Aircraft platform is used for the purposes of this study. The Global FE model is reduced to a stick model using the unitary loading method described in Section 4.2.2.

The stick model is originally created in MSC. Nastran format, and then converted to ASWING format using an automated script for use with the geometrically nonlinear solver.

Table 1 gives the list of the parameters considered in this study, to determine their effect on the nonlinear moment increment,  $\Delta_e$ , as well as the gradient operator used to compute the local sensitivity.

Table 5: Parameters being studied for the sensitivity analyses

<i>Parameter (<math>\Delta</math>)<sup>1</sup></i>	<i>Baseline value (<math>\Delta_0</math>)</i>	<i>Lower limit</i>	<i>Upper limit</i>	$\Delta_{inc}$ (units)	Finite difference type
<i>Out – of – plane stiffness (<math>\hat{I}_{11}</math>)</i>	100	$-10\Delta_{inc}$	0	7.5 (%)	Backward
<i>Wing position (<math>\Delta_{W_{CA}}</math>)</i>	0	$-5\Delta_{inc}$	$5\Delta_{inc}$	2.54 (cm)	Central
<i>Tail position (<math>\Delta_{T_{CA}}</math>)</i>	0	$-5\Delta_{inc}$	$5\Delta_{inc}$	5.08 (cm)	Central
<i>Engine position – longitudinal (<math>\Delta_{E_{long}}</math>)</i>	0	$-5\Delta_{inc}$	$5\Delta_{inc}$	2.54 (cm)	Central
<i>Engine position – lateral (<math>\Delta_{E_{lat}}</math>)</i>	0	$-5\Delta_{inc}$	$5\Delta_{inc}$	2.54 (cm)	Central
<i>Engine mass (<math>\Delta_{E_M}</math>)</i>	0	$-5\Delta_{inc}$	$5\Delta_{inc}$	1 (%)	Central

---

<sup>1</sup> The delta notation, ( $\Delta$ ), represents small variations of a given parameter with respect to a baseline value of the original aircraft.

The hatted  $\hat{\cdot}$  notation represents values that are normalized with respect to the baseline aircraft's value.

### 5.2.1 Sensitivity due to change in wing stiffness distribution

To evaluate the sensitivity of the peak gust loads to the reduction in out of plane stiffness,  $\hat{I}_{11}$ , the backwards-difference gradient operator is used as:

$$\zeta|_{\Delta_0} = \frac{\Delta_e(\Delta_0 - \Delta_{inc}) - \Delta_e(\Delta_0)}{\Delta_{inc}} \quad (181)$$

where  $\Delta_{inc}$  is a small reduction in the out of plane wing stiffness with respect to the baseline aircraft value.

Here, the aircraft wing is assumed as a stick model [17] represented by a set of beam elements extending along the wing elastic axis.

### 5.2.2 Sensitivity by central difference method

The sensitivity of peak gust loads to the out of plane wing stiffness was presented separate from the other parameters due to the range of acceptable parameters used in this study. The rest of the parameters are varied with respect to their baseline conditions,  $\Delta_0 = 0$ , and as such, the local gradient can be calculated with the use of two points around the baseline value. As such, the gradient operator used to calculate the loads sensitivity to each individual parameter is the central difference method, given as:

$$\zeta|_{\Delta_0} = \frac{\Delta_e(\Delta_0 + \Delta_{inc}) - \Delta_e(\Delta_0 - \Delta_{inc})}{2\Delta_{inc}} \quad (182)$$

### **5.3 Results and Discussion**

The following section presents a comparison of the loads calculated by linear and nonlinear solvers and discusses the results of the parametric variation of the aircraft design parameters.

#### **5.3.1 Baseline comparison**

To obtain a baseline comparison between the linear and the nonlinear dynamic aeroelastic solutions, a 1MC gust simulation is performed on the aircraft model to observe the time-domain behaviour of the aircraft between Nastran SOL 146 and ASWING. The resultant out of plane bending loads are shown in Figure 46. It can be observed that the primary peak bending loads occurring before 0.5s match closely between the two simulations. In this work, the effects being considered are solely the effect of geometric nonlinearities on the primary peak loads, and as such, the ASWING model is deemed appropriate.

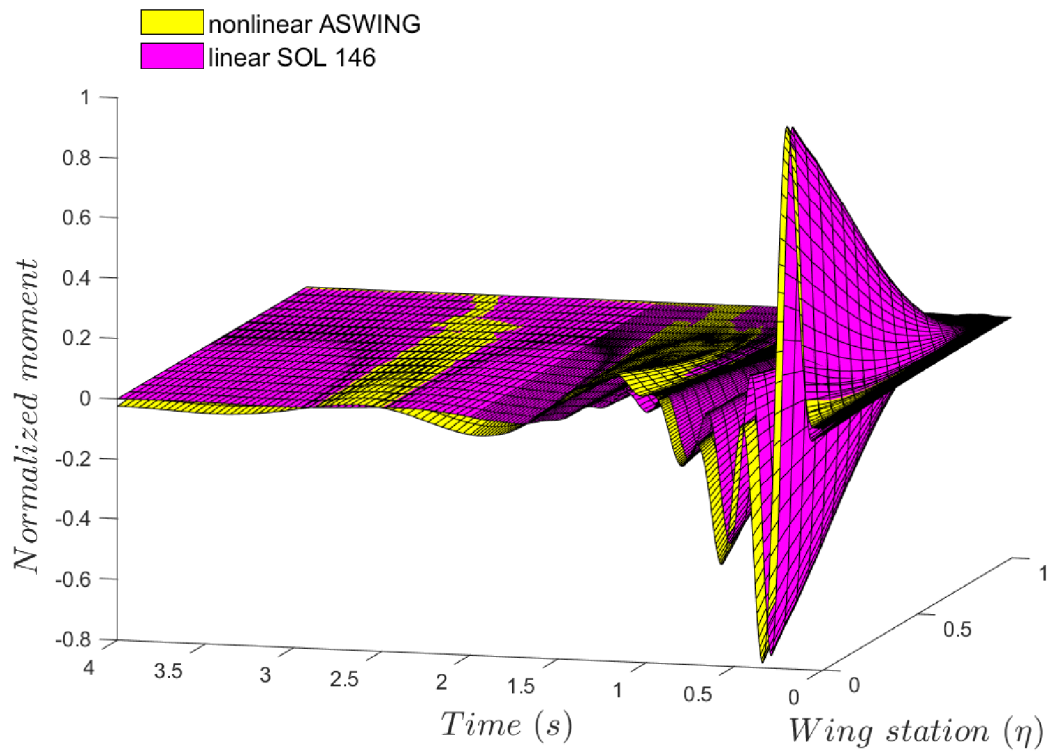


Figure 46: Normalized out of plane bending moment during dynamic gust simulation

### 5.3.2 Variation of Aircraft Design Parameters

For each design parameter, the results are shown for the maximum peak dynamic load using the nonlinear ASWING results, compared with the linear Nastran SOL146 results.

The results for the positive and negative peak bending moment, from both the linear SOL 146, and the nonlinear ASWING solvers are shown in Figure 47 and Figure 48 as a function of the varying out of plane stiffness,  $\hat{I}_{11}$ .

### 5.3.2.1 Variation of wing stiffness

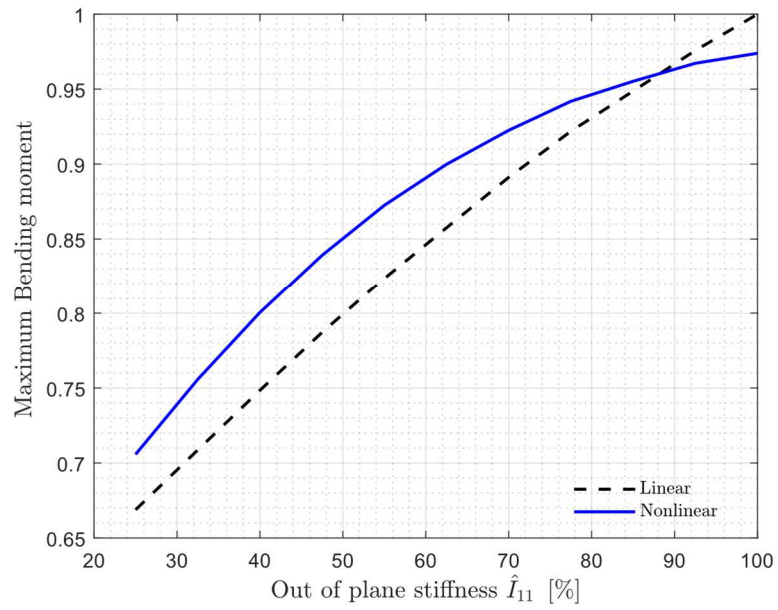


Figure 47: Variation in the positive peak gust load vs wing stiffness,  $\hat{I}_{11}$

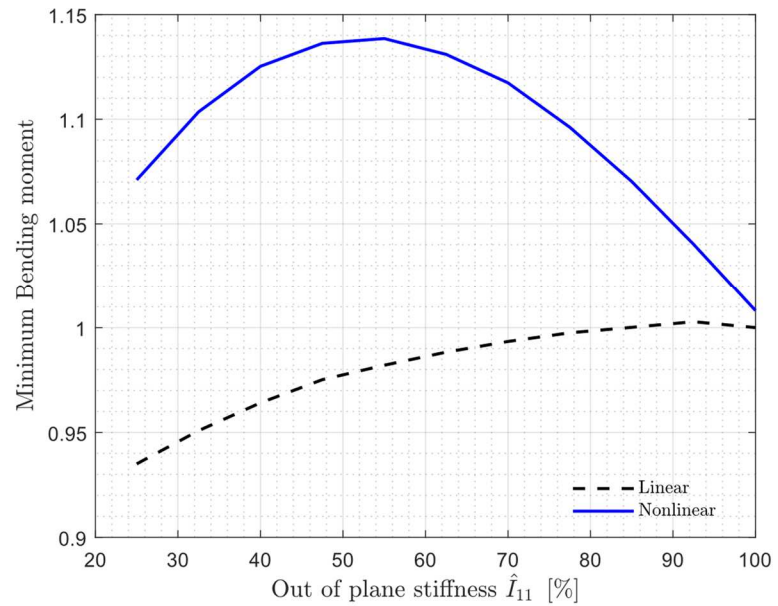


Figure 48: Variation in the negative peak gust load vs wing stiffness,  $\hat{I}_{11}$

As shown in Figure 47 and Figure 48, the out of plane bending moments have a highly nonlinear relationship with respect to the reduction in wing stiffness. As the mass and stiffness of the wing reduce, the overall deflection of the wing increases, which leads to a higher root bending moment. This can be observed in the previous work by the author [1], where the nonlinear root bending moment due to the more flexible wings are shown to be higher than the corresponding linear loads. However as this is a dynamic loading condition, there is another phenomenon in action, in which the highly deformable wing acts as a passive gust alleviation mechanism, reducing the peak loads on the structure [7], [8], [85].

#### *5.3.2.2 Variation of wing-fuselage attachment point*

In this study, the connection point between the elastic axes of the wing and fuselage is shifted about its default position on the baseline aircraft. Denoted  $\Delta W_{CA}$ , this variation has the effect of changing the distance between the aircraft centre of gravity and the mean aerodynamic centre (MAC). Figure 49 provides a visual aid to understand the effect of varying  $\Delta W_{CA}$ .

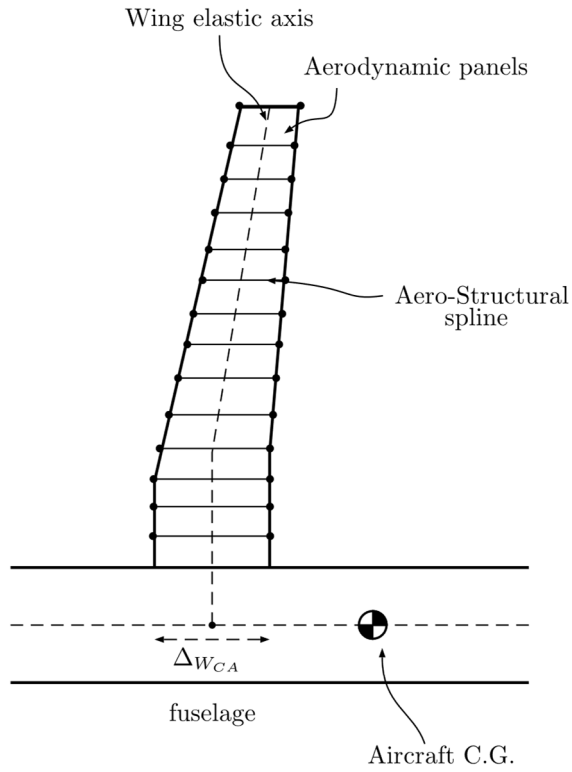


Figure 49: Wing-Fuselage attachment

The aerodynamic centre of the main wing was altered by shifting the attachment point between the wing and fuselage in the forward-aft direction, as shown in Figure 49.

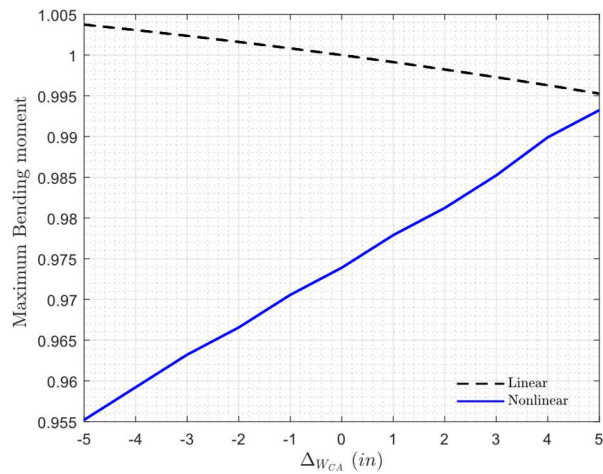


Figure 50: Variation in the positive peak gust load as the aerodynamic centre is moved forward and aft

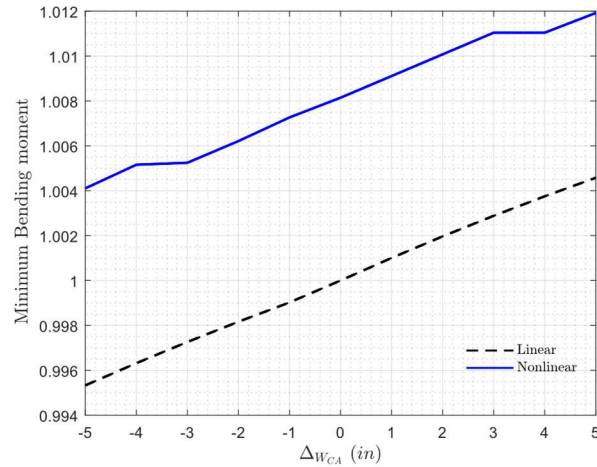


Figure 51: Variation in the negative peak gust load as the aerodynamic centre is moved forward and aft. The effect of these changes on the peak gust moments can be seen in Figure 50 and Figure 51. The changes in root bending loads are close to linear, since the shift in  $\Delta W_{CA}$  results in the linear increase or decrease of the proportion of the aircraft mass supported by the wing. The nonlinear positive peak loads vary by up to  $\pm 2\%$  while the corresponding linear loads are varied by less than 0.5%. The change in the negative peak loads is less than 1% across the entire range of the design space.

### 5.3.2.3 Variation of tail elevator aerodynamic centre of pressure

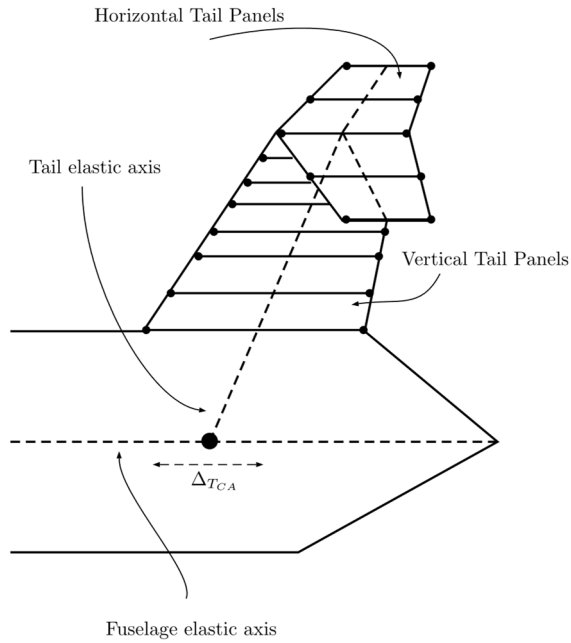


Figure 52: Tail-Fuselage attachment

Similarly to the shift in the wing aerodynamic centre, the attachment point of the tail assembly to the aircraft fuselage is shifted to study if there is any significant change in wing root bending moments.

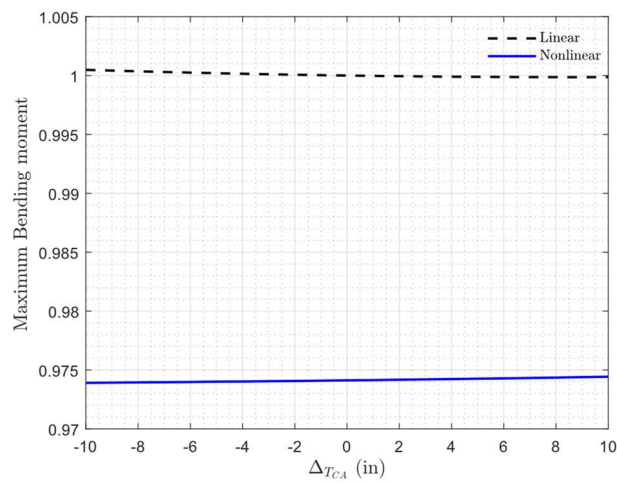


Figure 53: Variation in the positive peak gust load as the tail aerodynamic centre is moved forward and aft

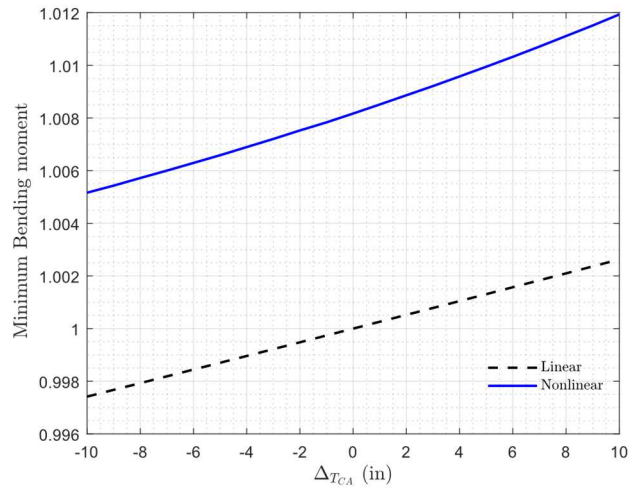


Figure 54: Variation in the negative peak gust load as the tail aerodynamic centre is moved forward and aft

Figure 53 and Figure 54 show that the variation in wing loads is negligible as the tail aerodynamic centre is shifted  $\pm 5$  in. This result is not unexpected as the shift in the overall centre of lift is not significantly affected by  $\Delta T_{CA}$  shift of a few inches.

#### 5.3.2.4 Variation in engine longitudinal position

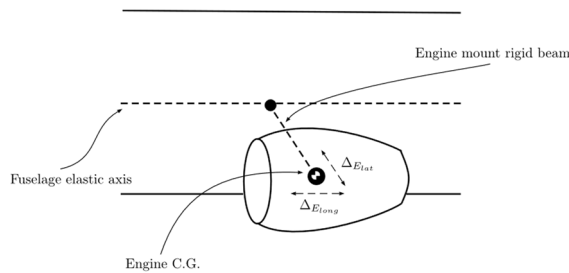


Figure 55: Engine C.G. shift

Figure 55 shows how the C.G. of the engine is shifted longitudinally along the fuselage and laterally perpendicular to it, to study the effects of engine positioning on nonlinear wing root moments.

The forward-aft position of the engine is shifted to observe the effects on the dynamic gust loads experienced, if any.

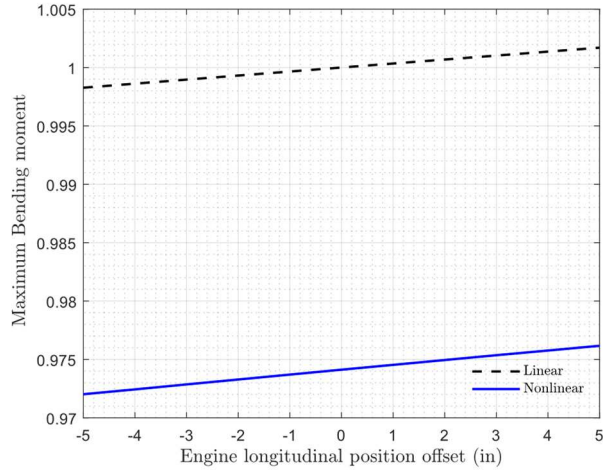


Figure 56: Variation in the positive peak gust load as the engine centre of mass is moved longitudinally

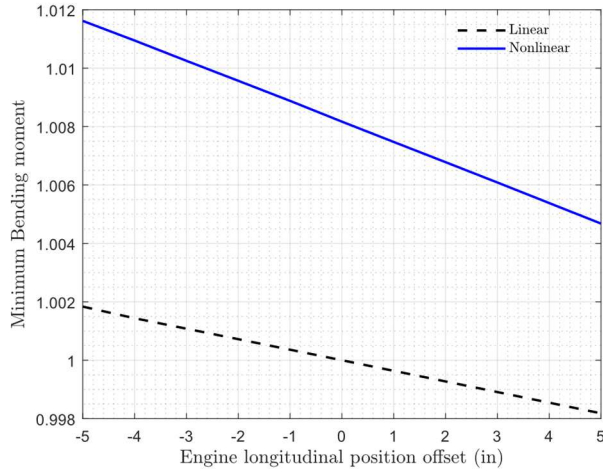


Figure 57: Variation in the negative peak gust load as the engine centre of mass is moved longitudinally

The shift in the engine longitudinal position results in overall loads changes of less than 1%, as the aircraft centre of gravity is shifted closer to the wing when  $\Delta_{E_{long}}$  is negative.

### 5.3.2.5 Variation in engine lateral position

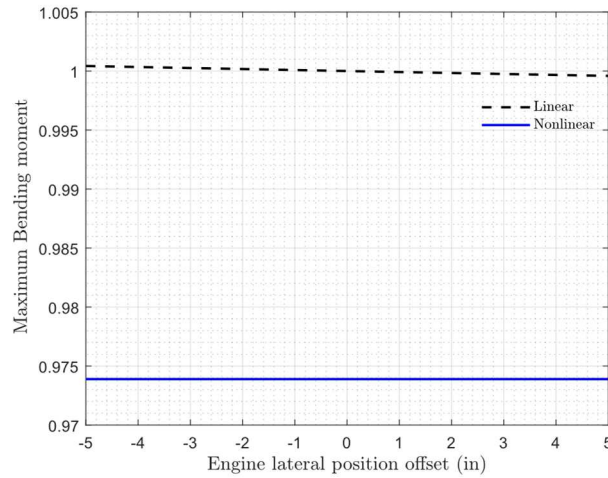


Figure 58: Variation in the positive peak gust load as the engine centre of mass is moved laterally

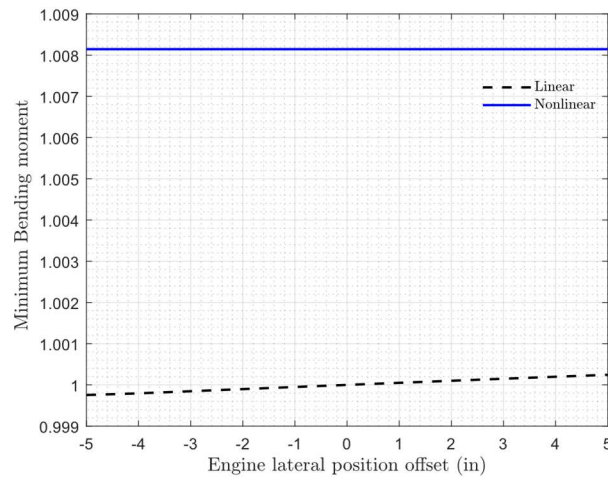


Figure 59: Variation in the negative peak gust load as the engine centre of mass is moved laterally

The change in loads due to lateral engine C.G. shifts, shown in Figure 58 and Figure 59, are negligible as they do not change the C.G. of the aircraft, thus keeping the overall load on the wing the same.

### 5.3.2.6 Variation in engine mass

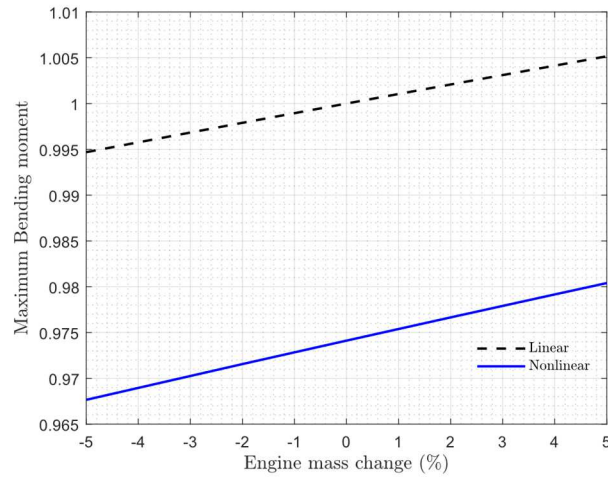


Figure 60: Variation in the positive peak gust load as the engine mass is varied by  $\pm 5\%$

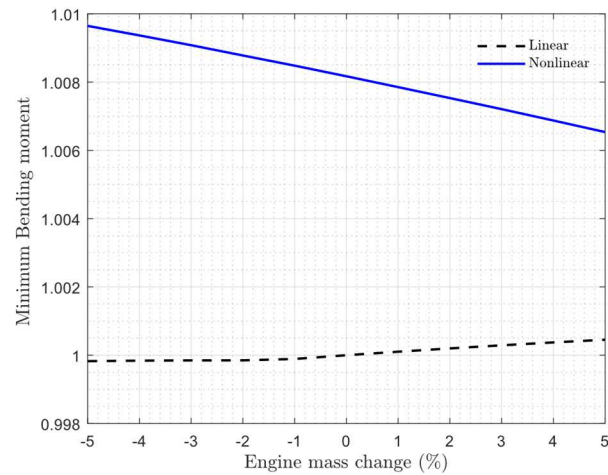


Figure 61: Variation in the negative peak gust load as the engine mass is varied by  $\pm 5\%$

The positive peak loads increase with the increase to the engine mass, while the negative nonlinear peak loads can be seen to follow the opposite trend

## **5.4 Chapter Summary**

This Chapter presented the results of the study into nonlinear dynamic aeroelastic loads by emulating the conceptual design phase of an aircraft through the variation of key aircraft design parameters. The next step would be to investigate the importance of having a geometrically nonlinear solver for the design parameters, and if they can be approximated by a linear approach to save computational time.

## 6 Dynamic Aeroelasticity: Sensitivity Analysis

In this section, the results from the previous section are studied to determine the baseline airframe's sensitivity to change in various structural parameters when geometrically nonlinear effects are considered. The maximum allowable error in dynamic loads, determined to be 0.8% for this specific aircraft platform, is denoted by the dashed red line.

### 6.1 Changes in wing stiffness

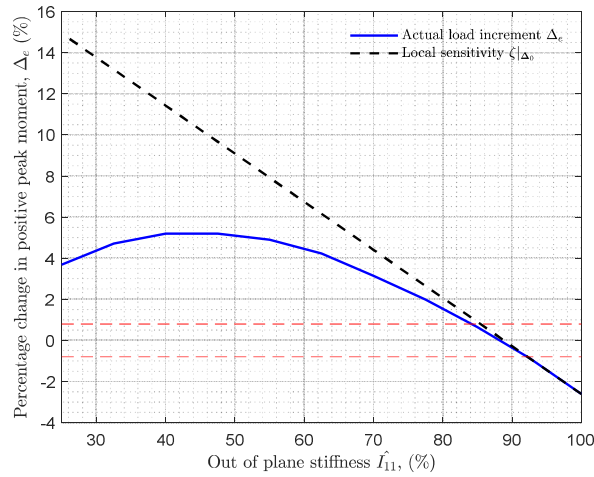


Figure 62: Sensitivity of nonlinear loads to variations in out of plane stiffness

The local sensitivity around the baseline stiffness of the aircraft,  $\zeta|_{\Delta_0}$ , deviates significantly from the actual change in nonlinear bending moment,  $\Delta_e$ , as calculated by the nonlinear solver. This is explained as the combined effect of passive gust load alleviation due to flexible wings [7], [8], [85] as well as increasing nonlinear loads due to large wing deflections [1]. As shown in Figure 62, the highly nonlinear behaviour cannot be estimated with a sensitivity analysis with respect to the baseline structure.

## 6.2 Changes in wing and tail aerodynamic centre

The positioning of the aerodynamic centre,  $\Delta_{WCA}$ , is adjusted by shifting all aerodynamic and structural elements associated with the wing in the forward-aft direction.

The movement of the aerodynamic centre along the fuselage changes the stability of aircraft. As the centre of gravity is located behind the centre of lift, moving the centre of lift closer towards the centre of gravity increases the value of the loads exerted by the wing. This can be seen in in Figure 50 and Figure 51 where the normalized values of the root bending moment increase as the aerodynamic centre is shifted closer to the aircraft's centre of gravity.

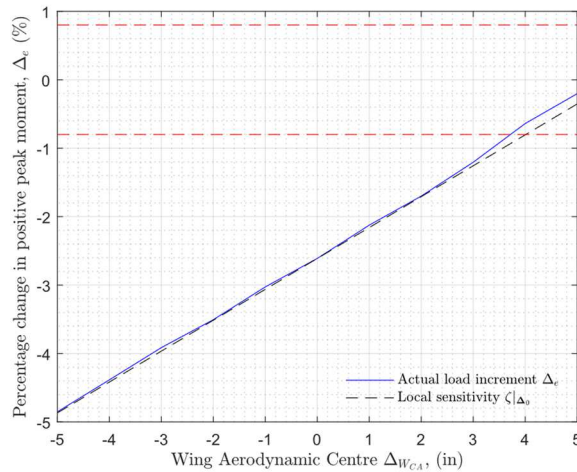


Figure 63: Sensitivity of nonlinear loads to variations in wing positioning

The sensitivity of the nonlinear load increment,  $\Delta_e$ , to the shift in the positioning of the tail aerodynamic centre,  $\Delta_{TCA}$ , is shown in Figure 64.

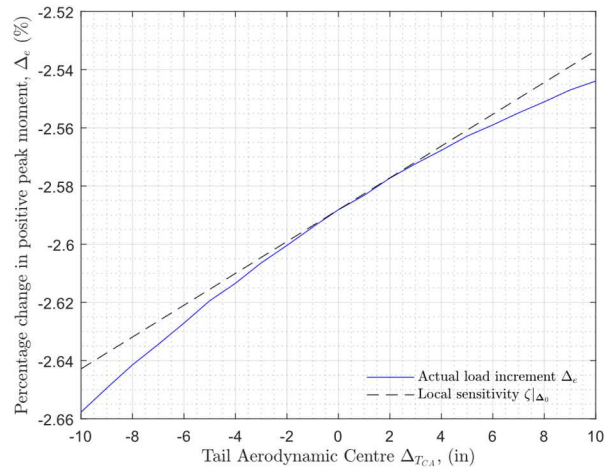


Figure 64: Sensitivity of nonlinear loads to variations in tail positioning

Unlike the shift in the aerodynamic centre of the wing, shifts in the position of the wing are not as significant to the nonlinear loads, with the overall load differences between the linear and nonlinear solution methods,  $\Delta_e$ , of less than 1% over the entire design space. This is due to the fact that the magnitude of the loads on the aircraft wing do not shift much as a result of the shift in tail position, as seen in Figure 53 and Figure 54, where these changes result in less than 0.1% changes in the linear and nonlinear root bending moments at the wing.

### 6.3 Changes in engine mass and position

The changes in the engine mounting positions in the forward-aft and spanwise lateral directions,  $\Delta_{E_{long}}$  and  $\Delta_{E_{lat}}$  respectively, as well as the changes in the mass of the engine itself,  $\Delta_{E_m}$ , are seen to have minimal impact on the nonlinear root bending moment of the aircraft wing. The sensitivity of the nonlinear loads,  $\Delta_e$ , to these engine design parameters,

are shown in Figure 65 to Figure 67, and contribute to less than 1% differences in the peak loads experienced by the aircraft wing root.

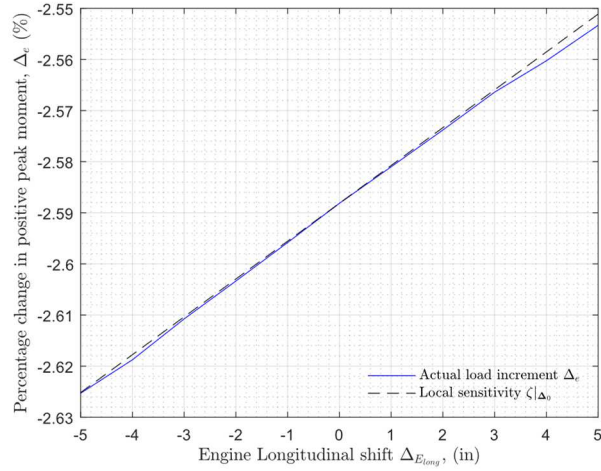


Figure 65: Sensitivity of nonlinear loads to variations in engine longitudinal position

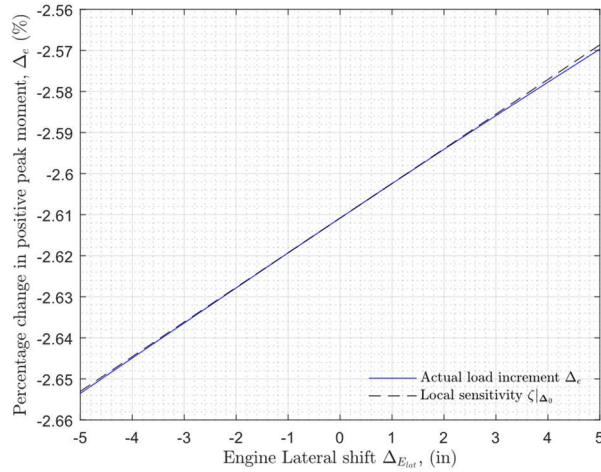


Figure 66: Sensitivity of nonlinear loads to variations in engine lateral position

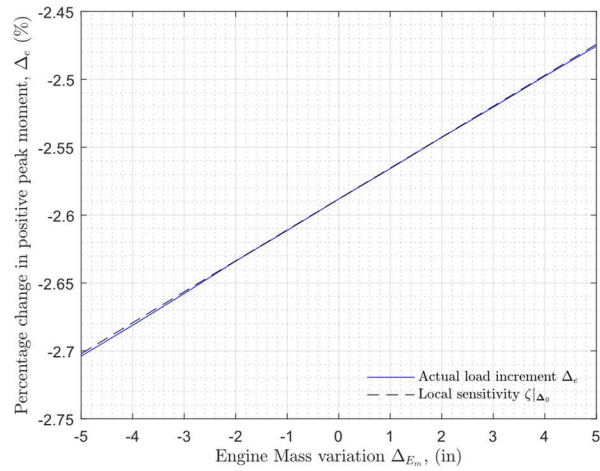


Figure 67: Sensitivity of nonlinear loads to variations in engine mass changes

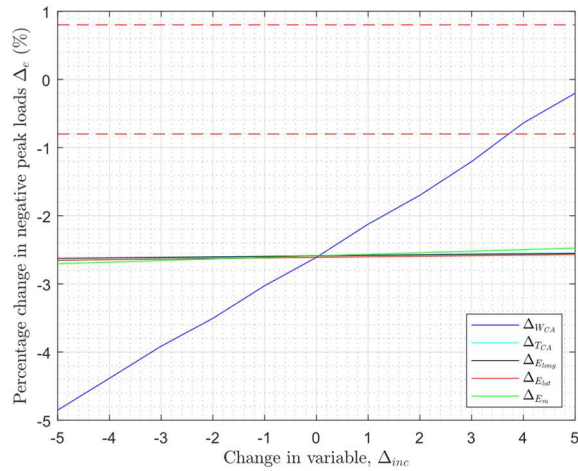


Figure 68: Sensitivity of nonlinear bending peak loads to variations of design parameters

## 6.4 Chapter Summary

This Chapter investigates the sensitivity of the increment in wing loads due to geometrically nonlinear effects as a function of key aircraft conceptual design parameters.

It is found that with the exception of wing stiffness and the positioning of the wing

aerodynamic center, load variations due to changes in all other key design parameters can be estimated by using a local gradient based approach with respect to the aircraft baseline structure. However, a nonlinear aeroelastic solver will be required across the entire design space when changes to the wing positioning or wing flexibility are made.

## 7 Conclusion

The work in this thesis is performed to identify the importance of including geometrically nonlinear effects in the aeroelastic simulation of static and dynamic flight cases.

Firstly, the author is presenting a new methodology for the calculation of nonlinear static aeroelastic loads, which is closely linked to the MSC Nastran environment. The method improves upon the literature by including additional degrees of freedom in the form of wing downwash, with the effect of increasing loads calculation fidelity. Additionally, this method can be easily used by any existing user of Nastran to obtain more accurate loads estimates for various static and quasi-static flight conditions. It is found that the out of plane bending moment exceeds the platform specific accuracy threshold of 1% loads difference, when the out of plane stiffness is reduced to 70% of the original value. For the most flexible variant of airframe considered, differences of 20%, 13% and 30% are observed, respectively, in the out of plane bending moment, out of plane shear force and torque. Additionally, substantial differences are observed in the corresponding trimming configuration, with changes of -12% and -8% in the trimming angle of attack and elevator deflection, respectively.

The second major part of the thesis studies the sensitivity of the airframe structure provided by Bombardier Aerospace, to variations in a multitude of conceptual design parameters. The sensitivity analysis was performed by using a nonlinear dynamic aeroelastic solver, ASWING, in conjunction with MSC Nastran. This allowed the analysis of the change in root bending load due to the inclusion of geometrically nonlinear effects. The reduction of

the out of plane bending stiffness is found to have the greatest effect on the difference between linear and nonlinear bending moment loads. The nonlinear bending moment exceeds the platform specific dynamic loads criteria of 0.8% when the out of plane bending stiffness is reduced to 85% of the original value. The position of the wing aerodynamic centre is found to influence the nonlinear bending moment significantly, resulting in a higher bending moment as the aerodynamic centre is shifted towards the aircraft centre of gravity. The other parameters studied were found to have very little difference in the loads using linear and nonlinear methodologies, indicating an independence from geometric nonlinearity.

Furthermore, the effects of the parametric variations will undoubtedly have an effect on the dynamic flight stability of the aircraft. However, aircraft stability is not considered in this work, and the aircraft dynamic configuration is not studied. Further work could also investigate into the stability of varying the aircraft design parameters when a geometrically nonlinear structural solver is used for dynamic aeroelasticity.

In this work, it was established that there is very little difference between the many methods available for formulating geometric nonlinearities. As such, the main differentiating factor between aeroelastic solvers would be the choice and complexity of the aerodynamic solver used. A convergence study of the different nonlinear methods reviewed here may be of use in the future to compare with established solvers like Nastran.

The most straightforward continuation of the work presented in this thesis would be to implement a dynamic geometrically nonlinear aeroelastic solver within the MSC Nastran environment using the same aerodynamic solver to implement both linear and nonlinear

dynamic aeroelastic solutions, thus allowing engineers to study the aircraft loads when geometrically nonlinear effects are active in a consistent environment.

## 8 References

- [1] M. A. A. Salman, M. S. A. ElSayed, and D. Walch, “Structural Nonlinearities and their Impact on the Fidelity of Critical Steady Maneuver Loads and Trimming Configuration of Very Flexible Airframes,” *J. Aeroelasticity Struct. Dyn.*, vol. 6, no. 1, 2018.
- [2] D. L. Greene, “Energy-efficiency improvement potential of commercial aircraft,” *Annu. Rev. Energy Environ.*, vol. 17, no. 1, pp. 537–573, 1992.
- [3] J. D. Anderson Jr, *Fundamentals of aerodynamics*. Tata McGraw-Hill Education, 2010.
- [4] A. Abbas, J. De Vicente, and E. Valero, “Aerodynamic technologies to improve aircraft performance,” *Aerosp. Sci. Technol.*, vol. 28, no. 1, pp. 100–132, 2013.
- [5] F. Afonso, J. Vale, É. Oliveira, F. Lau, and A. Suleman, “A review on non-linear aeroelasticity of high aspect-ratio wings,” *Prog. Aerosp. Sci.*, 2017.
- [6] J. Xiang, Y. Yan, and D. Li, “Recent advance in nonlinear aeroelastic analysis and control of the aircraft,” *Chinese J. Aeronaut.*, vol. 27, no. 1, pp. 12–22, 2014.
- [7] R. G. Cook, R. Palacios, and P. Goulart, “Robust Gust Alleviation and Stabilization of Very Flexible Aircraft,” *AIAA J.*, 2013.
- [8] K. Fidkowski, I. Kroo, K. Willcox, and F. Engelson, “Stochastic Gust Analysis Techniques for Aircraft Conceptual Design,” in *12th AIAA/ISSMO Multidisciplinary Analysis and Optimization Conference*, 2008.
- [9] C. Howcroft *et al.*, “Aeroelastic modelling of highly flexible wings,” in *15th*

*Dynamics Specialists Conference*, 2016, p. 1798.

- [10] G. Bindolino, G. Ghiringhelli, S. Ricci, and M. Terraneo, “Multilevel structural optimization for preliminary wing-box weight estimation,” *J. Aircr.*, vol. 47, no. 2, pp. 475–489, 2010.
- [11] M. S. A. Elsayed, R. Sedaghati, and M. Abdo, “Accurate stick model development for static analysis of complex aircraft wing-box structures,” *AIAA J.*, vol. 47, no. 9, pp. 2063–2075, 2009.
- [12] G. Corriveau and F. Dervault, “Impact of Wing Box Geometrical Parameters on Stick Model Prediction Accuracy,” in *54th AIAA/ASME/ASCE/AHS/ASC Structures, Structural Dynamics, and Materials Conference*, 2013, p. 1810.
- [13] R. CIRILLO, “Detailed and condensed finite element models for dynamic analysis of a business jet aircraft,” 2011.
- [14] M. Hashemi-Kia and M. Toossi, “Development and application of a technique for reducing airframe finite element models for dynamics analysis,” 1990.
- [15] A. K. Singh and C. W. Nichols, “Derivation of an equivalent beam model from a structural finite element model,” in *Proceedings of the MSC 1988 World Users Conference*, 1988.
- [16] Paul Vazhayil Thomas Mostafa SA ElSayed and D. Walch, “Development of High Fidelity Reduced Order Hybrid Stick Model for Aircraft Dynamic Aeroelasticity,” *J. Aerosp. Sci. Technol.*
- [17] P. V Thomas, M. S. A. Elsayed, and D. Walch, “Model Order Reduction of Complex

Airframes Using Component Mode Synthesis for Dynamic Aeroelasticity Load Analysis.”

- [18] P. V. Thomas, M. S. A. ElSayed, and D. Walch, “Review of Model Order Reduction Methods and Their Applications in Aeroelasticity Loads Analysis for Design Optimization of Complex Airframes,” *J. Aerosp. Eng.*, vol. 32, no. 2, p. 4018156, 2018.
- [19] S. H. Lee, “MSC/NASTRAN Nonlinear Analysis Handbook.” 1992.
- [20] G. R. Bhashyam, “ANSYS Mechanical—A Powerful Nonlinear Simulation Tool,” *Ansys, Inc*, 2002.
- [21] E. Madenci and I. Guven, *The finite element method and applications in engineering using ANSYS®*. Springer, 2015.
- [22] K.-J. Bathe, “Finite elements in CAD and ADINA,” *Nucl. Eng. Des.*, vol. 98, no. 1, pp. 57–67, 1986.
- [23] K. J. Bathe and S. Gracewski, “On nonlinear dynamic analysis using substructuring and mode superposition,” *Comput. Struct.*, 1981.
- [24] K.-J. Bathe, *Finite Element Procedures*. Klaus-Jurgen Bathe.
- [25] O. A. Bauchau and C. H. Hong, “Large displacement analysis of naturally curved and twisted composite beams,” *AIAA J.*, vol. 25, no. 11, pp. 1469–1475, 1987.
- [26] O. A. Bauchau and C. H. Hong, “Nonlinear composite beam theory,” *ASME, Trans. J. Appl. Mech.*, vol. 55, pp. 156–163, 1988.
- [27] W. Su and C. E. S. Cesnik, “Strain-based geometrically nonlinear beam formulation

- for modeling very flexible aircraft,” *Int. J. Solids Struct.*, vol. 48, no. 16, pp. 2349–2360, 2011.
- [28] M. Gams, I. Planinc, and M. Saje, “The strain-based beam finite elements in multibody dynamics,” *J. Sound Vib.*, vol. 305, no. 1, pp. 194–210, 2007.
- [29] H.-S. Ryu and H.-C. Sin, “Curved beam elements based on strain fields,” *Int. j. numer. method. biomed. eng.*, vol. 12, no. 11, pp. 767–773, 1996.
- [30] D. Zupan and M. Saje, “Finite-element formulation of geometrically exact three-dimensional beam theories based on interpolation of strain measures,” *Comput. Methods Appl. Mech. Eng.*, vol. 192, no. 49, pp. 5209–5248, 2003.
- [31] E. L. Brown, “Integrated strain actuation in aircraft with highly flexible composite wings,” 2003.
- [32] M. J. Patil, “Nonlinear aeroelastic analysis, flight dynamics, and control of a complete aircraft,” Georgia Institute of Technology, 1999.
- [33] D. H. Hodges, “A mixed variational formulation based on exact intrinsic equations for dynamics of moving beams,” *Int. J. Solids Struct.*, vol. 26, no. 11, pp. 1253–1273, 1990.
- [34] C. M. Shearer, “Coupled Nonlinear Flight Dynamics, Aeroelasticity, and Control of Very Flexible Aircraft,” University of Michigan, 2006.
- [35] W. Su, “Coupled Nonlinear Aeroelasticity and Flight Dynamics of Fully Flexible Aircraft,” 2008.
- [36] W. P. Rodden and E. H. Johnson, *MSC/NASTRAN aeroelastic analysis: user’s*

*guide; Version 68.* MacNeal-Schwendler Corporation, 1994.

- [37] K.-J. Bathe, *Finite element procedures*. Klaus-Jurgen Bathe, 2006.
- [38] M. Ritter, C. E. Cesnik, and W. R. Krüger, “An Enhanced Modal Approach for Large Deformation Modeling of Wing-Like Structures,” in *56th AIAA/ASCE/AHS/ASC Structures, Structural Dynamics, and Materials Conference*, 2015, p. 176.
- [39] A. E. H. Love, *A treatise on the mathematical theory of elasticity*. Cambridge university press, 1982.
- [40] E. Reissner, “On One-Dimensional Large-Displacement Finite-Strain Beam Theory,” *Stud. Appl. Math.*, vol. 52, no. 2, pp. 87–95, 1973.
- [41] D. H. Hodges, *Nonlinear Composite Beam Theory*. AIAA (American Institute of Aeronautics & Ast, 2006.
- [42] G. A. Hegemier and S. Nair, “A nonlinear dynamical theory for heterogeneous, anisotropic, elastic rods,” *AIAA J.*, vol. 15, no. 1, pp. 8–15, 1977.
- [43] D. H. Hodges, “Geometrically exact, intrinsic theory for dynamics of curved and twisted anisotropic beams,” *AIAA J.*, vol. 41, no. 6, pp. 1131–1137, 2003.
- [44] D. H. Hodges, “Erratum: Geometrically exact, intrinsic theory for dynamics of curved and twisted anisotropic beams,” *AIAA J.*, vol. 47, no. 5, pp. 1308–1309, 2009.
- [45] O. C. Zienkiewicz and R. L. Taylor, *The finite element method for solid and structural mechanics*. Butterworth-heinemann, 2005.
- [46] D. H. Hodges, W. Yu, and M. J. Patil, “Geometrically-exact, intrinsic theory for

- dynamics of moving composite plates,” *Int. J. Solids Struct.*, vol. 46, no. 10, pp. 2036–2042, 2009.
- [47] M. Drela, “ASWING 5.99 Technical Description,” *Massachusetts Inst. Technol. Cambridge, MA*, 2015.
- [48] W. Su and C. E. S. Cesnik, “Nonlinear aeroelasticity of a very flexible blended-wing-body aircraft,” *J. Aircr.*, vol. 47, no. 5, pp. 1539–1553, 2010.
- [49] M. C. Van Schoor and A. H. von Flotow, “Aeroelastic characteristics of a highly flexible aircraft,” *J. Aircr.*, vol. 27, no. 10, pp. 901–908, 1990.
- [50] M. J. Patil and D. H. Hodges, “Flight dynamics of highly flexible flying wings,” *J. Aircr.*, vol. 43, no. 6, pp. 1790–1798, 2006.
- [51] M. A. Crisfield, *Non-Linear Finite Element Analysis of Solids and Structures: Volume I*. Wiley, 1996.
- [52] J.-M. Battini, “Co-rotational beam elements in instability problems,” Royal Institute of Technology, Sweden, 2002.
- [53] P. Sivanagendra, “Geometrically Nonlinear Elastic Analysis of Frames with Application to Vision-Based Forcesensing and Mechanics of Plant Stems,” Indian Institute of Science, 2006.
- [54] H. Stolarski and T. Belytschko, “Shear and membrane locking in curved C0elements,” *Comput. Methods Appl. Mech. Eng.*, 1983.
- [55] H. Stolarski and T. Belytschko, “Membrane Locking and Reduced Integration for Curved Elements,” *J. Appl. Mech.*, 1982.

- [56] O. Weeger, U. Wever, and B. Simeon, “Isogeometric analysis of nonlinear Euler--Bernoulli beam vibrations,” *Nonlinear Dyn.*, vol. 72, no. 4, pp. 813–835, 2013.
- [57] C. A. Felippa, “Standard Mass Matrices For Plane Beam Elements,” 2013.
- [58] K.-J. Bathe, E. Ramm, and E. L. Wilson, “Finite element formulations for large deformation dynamic analysis,” *Int. J. Numer. Methods Eng.*, vol. 9, no. 2, pp. 353–386, 1975.
- [59] F. Ribeiro, P. Paglione, R. G. A. da Silva, and M. S. de Sousa, “Aeroflex: a toolbox for studying the flight dynamics of highly flexible airplanes,” in *Congresso Nacional de Engenharia Mecânica*, 2012, pp. 1786–2012.
- [60] Q. Wang and W. Yu, “Geometrically nonlinear analysis of composite beams using Wiener-Milenković parameters,” *J. Renew. Sustain. Energy*, vol. 9, no. 3, p. 33306, 2017.
- [61] C. Moler and others, *MATLAB users’ guide*. University of New Mexico, 1982.
- [62] L. F. Shampine and M. W. Reichelt, “The MATLAB ODE Suite,” *SIAM J. Sci. Comput.*, 1997.
- [63] Y. Wenbin and W. Qi, “Geometrically Exact Beam Theory.” Jul-2014.
- [64] W. Yu and M. Blair, “GEBT: A general-purpose nonlinear analysis tool for composite beams,” *Compos. Struct.*, 2012.
- [65] M. S. C. Nastran, “Nonlinear user’s guide,” *MSC Softw.*, 2014.
- [66] J. Bonet and R. D. Wood, *Nonlinear continuum mechanics for finite element analysis*. Cambridge university press, 1997.

- [67] M. Sathyamoorthy, *Nonlinear analysis of structures*, vol. 8. CRC Press, 1997.
- [68] T. Belytschko, W. K. Liu, B. Moran, and K. Elkhodary, *Nonlinear finite elements for continua and structures*. John Wiley & Sons, 2013.
- [69] J. Oliver and E. Onate, “A total lagrangian formulation for the geometrically nonlinear analysis of structures using finite elements. Part I. Two-dimensional problems: Shell and plate structures,” *Int. J. Numer. Methods Eng.*, vol. 20, no. 12, pp. 2253–2281, 1984.
- [70] E. Albano and W. P. Rodden, “A doublet-lattice method for calculating lift distributions on oscillating surfaces in subsonic flows.,” *AIAA J.*, vol. 7, no. 2, pp. 279–285, 1969.
- [71] W. P. Rodden, J. P. Giesing, and T. P. Kalman, “Refinement of the nonplanar aspects of the subsonic doublet-lattice lifting surface method.,” *J. Aircr.*, vol. 9, no. 1, pp. 69–73, 1972.
- [72] H. T. Vivian and L. V. Andrew, “Unsteady aerodynamics for advanced configurations. part i. application of the subsonic kernel function to nonplanar lifting surfaces,” 1965.
- [73] J. B. E. Bosco J. Morlier and A. Lucchetti, “Influence of mass modelling in dynamic landing simulations,” in *10th PEGASUS-AIAA student conference*, 2014.
- [74] W. C. Young and R. G. Budynas, *Roark’s formulas for stress and strain*, vol. 7. McGraw-Hill New York, 2002.
- [75] P. J. Minguet, “Static and dynamic behavior of composite helicopter rotor blades

under large deflections,” Massachusetts Institute of Technology, 1989.

- [76] R. G. Cook, D. E. Calderon, J. E. Cooper, M. H. Lowenberg, S. A. Neild, and E. B. Coetzee, “Worst Case Gust Prediction of Highly Flexible Wings,” in *58th AIAA/ASCE/AHS/ASC Structures, Structural Dynamics, and Materials Conference*, 2017, p. 1355.
- [77] M. Castellani, J. E. Cooper, and Y. Lemmens, “Nonlinear static aeroelasticity of high-aspect-ratio-wing aircraft by finite element and multibody methods,” *J. Aircr.*, pp. 1–13, 2016.
- [78] M. J. Patil, D. H. Hodges, and C. E. S. Cesnik, “Nonlinear aeroelasticity and flight dynamics of high-altitude long-endurance aircraft,” *J. Aircr.*, vol. 38, no. 1, pp. 88–94, 2001.
- [79] W. Su *et al.*, “Nonlinear user’s guide,” *J. Aircr.*, vol. 47, no. 1, pp. 8–15, 2011.
- [80] M. J. Patil, D. H. Hodges, and C. E. S. Cesnik, “Characterizing the effects of geometrical nonlinearities on aeroelastic behavior of high-aspect ratio wings,” in *Proceedings of the International Forum on Aeroelasticity and Structural Dynamics*, 1999, pp. 501–510.
- [81] D. Tang and E. H. Dowell, “Experimental and theoretical study on aeroelastic response of high-aspect-ratio wings,” *AIAA J.*, vol. 39, no. 8, pp. 1430–1441, 2001.
- [82] C. M. Shearer, “Coupled Nonlinear Flight Dynamics, Aeroelasticity, and Control of Very Flexible Aircraft,” 2006.
- [83] J. K. Zbrozek, *The relationship between the discrete gust and power spectra*

*presentations of atmospheric turbulence, with a suggested model of low-altitude turbulence.* HM Stationery Office, 1961.

- [84] H. I. Flomenhoft, “Brief history of gust models for aircraft design,” *J. Aircr.*, 1994.
- [85] B. C. B. Tse, “Effects of Inertial and Geometric Nonlinearities in the Simulation of Flexible Aircraft Dynamics,” University of Toronto, 2013.

## Appendix A: Strain Based Formulation Matrices

The exponential and Jacobian matrices used in the strain-based formulation are presented here in full. The matrices are taken from the thesis by Shearer [34].

### Matrix exponential $e^{A(\xi-\xi_0)}$

The matrix exponential used in Equation (62) is obtained as follows

$$\begin{aligned}
 & e^{A(\xi-\xi_0)} \\
 = & \begin{bmatrix} 1 & 0 & 0 & 0 \\ 0 & 1 & 0 & 0 \\ 0 & 0 & 1 & 0 \\ 0 & 0 & 0 & 1 \end{bmatrix} + (\xi - \xi_0) \begin{bmatrix} 0 & 1 + \epsilon_x & 0 & 0 \\ 0 & 0 & \kappa_z & -\kappa_y \\ 0 & -\kappa_z & 0 & \kappa_x \\ 0 & \kappa_y & -\kappa_x & 0 \end{bmatrix} \\
 & + \frac{1 - \cos(\bar{\lambda}(\xi - \xi_0))}{\bar{\lambda}^2} \begin{bmatrix} 0 & 0 & \epsilon_x \kappa_z & -\epsilon_x \kappa_y \\ 0 & -(\bar{\lambda}^2 - \kappa_x^2) & \kappa_x \kappa_y & \kappa_x \kappa_z \\ 0 & \kappa_x \kappa_y & -(\bar{\lambda}^2 - \kappa_y^2) & \kappa_y \kappa_z \\ 0 & \kappa_x \kappa_z & \kappa_y \kappa_z & -(\bar{\lambda}^2 - \kappa_z^2) \end{bmatrix} \\
 & + \left( \frac{(\xi - \xi_0)}{\bar{\lambda}^2} + \frac{\sin(\bar{\lambda}(\xi - \xi_0))}{\bar{\lambda}^3} \right) \begin{bmatrix} 0 & \epsilon_x (\kappa_y^2 + \kappa_z^2) & -\epsilon_x \kappa_x \kappa_y & \epsilon_x \kappa_x \kappa_z \\ 0 & 0 & -\kappa_z \bar{\lambda}^2 & \kappa_y \bar{\lambda}^2 \\ 0 & \kappa_z \bar{\lambda}^2 & 0 & -\kappa_x \bar{\lambda}^2 \\ 0 & -\kappa_y \bar{\lambda}^2 & \kappa_x \bar{\lambda}^2 & 0 \end{bmatrix}
 \end{aligned} \tag{183}$$

where

$$\epsilon_x = 1 + \epsilon_x \tag{184}$$

and

$$\bar{\lambda} = \sqrt{\kappa_x^2 + \kappa_y^2 + \kappa_z^2} \tag{185}$$

## Jacobian Matrices

The relationship between the independent strains and rotations, and the dependent displacements and orientation are given as follows

$$\begin{aligned}
 dh &= J_{h\varepsilon}d\varepsilon + J_{hb}db \\
 dp &= J_{p\varepsilon}d\varepsilon + J_{pb}db \\
 d\theta &= J_{\theta\varepsilon}d\varepsilon + J_{\theta b}db
 \end{aligned} \tag{186}$$

As shown in Equation 76, the rigid body components of the strain equations of motion are neglected due to the conditions of the test case being studied. As such, only the  $J_{h\varepsilon}$ ,  $J_{p\varepsilon}$ , and  $J_{\theta\varepsilon}$  Jacobians are detailed here.

### Matrix $J_{h\varepsilon}$

$$J_{h\varepsilon} = \begin{bmatrix}
 0 & 0 & 0 & \dots \\
 \frac{\partial e^{\bar{G}_1}}{\partial \varepsilon_1} h_{bc,1} & 0 & 0 & \dots \\
 \frac{\partial e^{\bar{2G}_1}}{\partial \varepsilon_1} h_{bc,1} & 0 & 0 & \dots \\
 D_{2,1}(J_{h\varepsilon})_{3,1} & 0 & 0 & \dots \\
 e^{\bar{G}_2}(J_{h\varepsilon})_{4,1} & \frac{\partial e^{\bar{G}_2}}{\partial \varepsilon_2} h_{bc,2} & 0 & \dots \\
 e^{\bar{G}_2}(J_{h\varepsilon})_{5,1} & \frac{\partial e^{\bar{2G}_2}}{\partial \varepsilon_2} h_{bc,2} & 0 & \dots \\
 D_{3,2}(J_{h\varepsilon})_{6,1} & D_{3,2}(J_{h\varepsilon})_{6,2} & 0 & \dots \\
 e^{\bar{G}_3}(J_{h\varepsilon})_{7,1} & e^{\bar{G}_3}(J_{h\varepsilon})_{7,2} & \frac{\partial e^{\bar{G}_3}}{\partial \varepsilon_2} h_{bc,3} & \dots \\
 e^{\bar{G}_3}(J_{h\varepsilon})_{8,1} & e^{\bar{G}_3}(J_{h\varepsilon})_{8,2} & \frac{\partial e^{\bar{2G}_3}}{\partial \varepsilon_2} h_{bc,3} & \dots \\
 \vdots & \vdots & \vdots & \ddots
 \end{bmatrix} \tag{187}$$

where  $(J_{h\varepsilon})_{i,j}$  is the  $i^{th}$  row,  $j^{th}$  column of the  $J_{h\varepsilon}$  matrix, and each component in itself is a  $12 \times 4$  sub-matrix. The above matrix is for a beam with  $n$  elements, and the  $h_{bc,n}$  is the boundary conditions for each element, and  $D_{n,n-1}$  is a rotation matrix that relates the orientation of the  $n^{th}$  element to the previous one and accounts for slope discontinuity between the undeformed elements.

The  $D$  matrix is given as

$$D_{n,n-1} = \begin{bmatrix} [\mathbf{1}] & 0 & 0 & 0 \\ 0 & \underline{C_{xx}^{wb}}[\mathbf{1}] & \underline{C_{yx}^{wb}}[\mathbf{1}] & \underline{C_{zx}^{wb}}[\mathbf{1}] \\ 0 & \underline{C_{xy}^{wb}}[\mathbf{1}] & \underline{C_{yy}^{wb}}[\mathbf{1}] & \underline{C_{zy}^{wb}}[\mathbf{1}] \\ 0 & \underline{C_{xz}^{wb}}[\mathbf{1}] & \underline{C_{yz}^{wb}}[\mathbf{1}] & \underline{C_{zz}^{wb}}[\mathbf{1}] \end{bmatrix} \quad (188)$$

where the individual  $\underline{C_{\{xyz\}\{xyz\}}^{wb}}$  are diagonal matrices containing the individual components of the  $\underline{C^{wb}}$  rotation matrix and  $[\mathbf{1}]$  is the  $3 \times 3$  identity matrix.

The exponential matrices are given as follows

$$e^{\bar{G}} = \begin{bmatrix} [\mathbf{1}] & [e^{A(s-s_0)}]_{1,2}[\mathbf{1}] & [e^{A(s-s_0)}]_{1,3}[\mathbf{1}] & [e^{A(s-s_0)}]_{1,4}[\mathbf{1}] \\ 0 & [e^{A(s-s_0)}]_{2,2}[\mathbf{1}] & [e^{A(s-s_0)}]_{2,3}[\mathbf{1}] & [e^{A(s-s_0)}]_{2,4}[\mathbf{1}] \\ 0 & [e^{A(s-s_0)}]_{3,2}[\mathbf{1}] & [e^{A(s-s_0)}]_{3,3}[\mathbf{1}] & [e^{A(s-s_0)}]_{3,4}[\mathbf{1}] \\ 0 & [e^{A(s-s_0)}]_{4,2}[\mathbf{1}] & [e^{A(s-s_0)}]_{4,3}[\mathbf{1}] & [e^{A(s-s_0)}]_{4,4}[\mathbf{1}] \end{bmatrix} \quad (189)$$

where  $[e^{A(s-s_0)}]_{i,j}$  is the component corresponding to the  $i^{th}$  row,  $j^{th}$  column of the matrix  $e^{A(s-s_0)}$ .

The evaluation of the partial derivative of  $e^{\bar{G}}$  is presented below, taken from [34].

$$\begin{aligned}
\frac{\partial e^{\bar{G}}}{\partial \varepsilon} &= \frac{\partial \hat{\alpha}_3}{\partial \varepsilon} AAA + \hat{\alpha}_3 \left( \frac{\partial A}{\partial \varepsilon} AA + A \frac{\partial A}{\partial \varepsilon} A + \frac{\partial A}{\partial \varepsilon} AA \right) + \frac{\partial \hat{\alpha}_2}{\partial \varepsilon} AA \\
&+ \hat{\alpha}_2 \left( \frac{\partial A}{\partial \varepsilon} A + A \frac{\partial A}{\partial \varepsilon} \right) + \frac{\partial \hat{\alpha}_1}{\partial \varepsilon} A + \hat{\alpha}_1 \frac{\partial A}{\partial \varepsilon} + \frac{\partial \hat{\alpha}_0}{\partial \varepsilon} [\mathbf{1}]
\end{aligned} \tag{190}$$

where coefficients  $\hat{\alpha}_{0-3}$  and their partial derivatives are given as

$$\begin{aligned}
\hat{\alpha}_0 &= 1 \\
\hat{\alpha}_1 &= \xi - \xi_0 = \Delta\xi \\
\hat{\alpha}_2 &= \frac{1 - \cos(\bar{\lambda}\Delta\xi)}{\bar{\lambda}^2} \\
\hat{\alpha}_3 &= \left( \frac{\Delta\xi}{\bar{\lambda}^2} + \frac{\sin(\bar{\lambda}\Delta\xi)}{\bar{\lambda}^3} \right)
\end{aligned} \tag{191}$$

and

$$\begin{aligned}
\frac{\partial \hat{\alpha}_0}{\partial \varepsilon} &= \frac{\partial \hat{\alpha}_1}{\partial \varepsilon} = 0 \\
\frac{\partial \hat{\alpha}_2}{\partial \varepsilon} &= \left( \bar{\lambda}\Delta\xi \sin(\bar{\lambda}\Delta\xi) - \frac{2(1 - \cos(\bar{\lambda}\Delta\xi))}{\bar{\lambda}^4} \right) \begin{bmatrix} 0 \\ \kappa_x[\mathbf{1}] \\ \kappa_y[\mathbf{1}] \\ \kappa_z[\mathbf{1}] \end{bmatrix} \\
\frac{\partial \hat{\alpha}_3}{\partial \varepsilon} &= \left( \frac{3 \sin(\bar{\lambda}\Delta\xi)}{\bar{\lambda}^5} - \frac{2\Delta\xi + \Delta\xi \cos(\bar{\lambda}\Delta\xi)}{\bar{\lambda}^4} \right) \begin{bmatrix} 0 \\ \kappa_x[\mathbf{1}] \\ \kappa_y[\mathbf{1}] \\ \kappa_z[\mathbf{1}] \end{bmatrix}
\end{aligned} \tag{192}$$

### Matrix $J_{pe}$

This matrix contains the rows  $i$  to  $j$  of  $J_{h\varepsilon}$  which correspond to the  $p_n$  absolute position vectors. For a beam with  $n$  elements

$$[J_{p\varepsilon}]_n = [J_{h\varepsilon}]_{rows\ i \rightarrow j} \quad (193)$$

where

$$i = 1 + 12(n - 1) \quad (194)$$

$$j = 3 + 13(n - 1)$$

The final matrix for  $J_{p\varepsilon}$  is assembled as follows

$$J_{p\varepsilon} = \begin{bmatrix} [J_{p\varepsilon}]_1 \\ [J_{p\varepsilon}]_2 \\ [J_{p\varepsilon}]_3 \\ \vdots \\ [J_{p\varepsilon}]_n \end{bmatrix} \quad (195)$$

### Matrix $J_{\theta e}$

This matrix relates the rotation of the deformed beam frame,  $w$ , due to a change in the strain vector of an element, expressed in the body reference frame,  $B$ .

$$[J_{\theta\varepsilon}]_n = \begin{bmatrix} \left(\frac{\partial\theta_x}{\partial\varepsilon_x}\right)_1^B & \left(\frac{\partial\theta_x}{\partial\kappa_x}\right)_1^B & \left(\frac{\partial\theta_x}{\partial\kappa_y}\right)_1^B & \left(\frac{\partial\theta_x}{\partial\kappa_z}\right)_1^B \\ \left(\frac{\partial\theta_y}{\partial\varepsilon_x}\right)_1^B & \left(\frac{\partial\theta_y}{\partial\kappa_x}\right)_1^B & \left(\frac{\partial\theta_y}{\partial\kappa_y}\right)_1^B & \left(\frac{\partial\theta_y}{\partial\kappa_z}\right)_1^B \\ \left(\frac{\partial\theta_z}{\partial\varepsilon_x}\right)_1^B & \left(\frac{\partial\theta_z}{\partial\kappa_x}\right)_1^B & \left(\frac{\partial\theta_z}{\partial\kappa_y}\right)_1^B & \left(\frac{\partial\theta_z}{\partial\kappa_z}\right)_1^B \\ \left(\frac{\partial\theta_x}{\partial\varepsilon_x}\right)_2^B & \left(\frac{\partial\theta_x}{\partial\kappa_x}\right)_2^B & \left(\frac{\partial\theta_x}{\partial\kappa_y}\right)_2^B & \left(\frac{\partial\theta_x}{\partial\kappa_z}\right)_2^B \\ \left(\frac{\partial\theta_y}{\partial\varepsilon_x}\right)_2^B & \left(\frac{\partial\theta_y}{\partial\kappa_x}\right)_2^B & \left(\frac{\partial\theta_y}{\partial\kappa_y}\right)_2^B & \left(\frac{\partial\theta_y}{\partial\kappa_z}\right)_2^B \\ \left(\frac{\partial\theta_z}{\partial\varepsilon_x}\right)_2^B & \left(\frac{\partial\theta_z}{\partial\kappa_x}\right)_2^B & \left(\frac{\partial\theta_z}{\partial\kappa_y}\right)_2^B & \left(\frac{\partial\theta_z}{\partial\kappa_z}\right)_2^B \\ \left(\frac{\partial\theta_x}{\partial\varepsilon_x}\right)_3^B & \left(\frac{\partial\theta_x}{\partial\kappa_x}\right)_3^B & \left(\frac{\partial\theta_x}{\partial\kappa_y}\right)_3^B & \left(\frac{\partial\theta_x}{\partial\kappa_z}\right)_3^B \\ \left(\frac{\partial\theta_y}{\partial\varepsilon_x}\right)_3^B & \left(\frac{\partial\theta_y}{\partial\kappa_x}\right)_3^B & \left(\frac{\partial\theta_y}{\partial\kappa_y}\right)_3^B & \left(\frac{\partial\theta_y}{\partial\kappa_z}\right)_3^B \\ \left(\frac{\partial\theta_z}{\partial\varepsilon_x}\right)_3^B & \left(\frac{\partial\theta_z}{\partial\kappa_x}\right)_3^B & \left(\frac{\partial\theta_z}{\partial\kappa_y}\right)_3^B & \left(\frac{\partial\theta_z}{\partial\kappa_z}\right)_3^B \end{bmatrix} \quad (196)$$

The individual components of the above matrix are obtained by taking the change in position vector due to strain, components from  $J_{h\varepsilon}$ , and premultiplying them with the corresponding nodal orientation vector,  $[w_x \ w_y \ w_z]_n^T$  as follows, for a given node  $i = 1,2,3$ .

$$\begin{bmatrix} \left(\frac{\partial \theta_x}{\partial \varepsilon_x}\right)_i^B \\ \left(\frac{\partial \theta_y}{\partial \varepsilon_x}\right)_i^B \\ \left(\frac{\partial \theta_z}{\partial \varepsilon_x}\right)_i^B \end{bmatrix} = \underline{C}^{Bw} \begin{bmatrix} w_{zx} \frac{\partial w_{yx}}{\partial \varepsilon_x} + w_{zy} \frac{\partial w_{yy}}{\partial \varepsilon_x} + w_{zz} \frac{\partial w_{yz}}{\partial \varepsilon_x} \\ w_{xx} \frac{\partial w_{yx}}{\partial \varepsilon_x} + w_{xy} \frac{\partial w_{yy}}{\partial \varepsilon_x} + w_{xz} \frac{\partial w_{yz}}{\partial \varepsilon_x} \\ w_{yx} \frac{\partial w_{yx}}{\partial \varepsilon_x} + w_{yy} \frac{\partial w_{yy}}{\partial \varepsilon_x} + w_{yz} \frac{\partial w_{yz}}{\partial \varepsilon_x} \end{bmatrix} \quad (197)$$

The final  $J_{\theta_\varepsilon}$  matrix is assembled as follows, for a beam with  $n$  elements

$$J_{\theta_\varepsilon} = \begin{bmatrix} [U_{\theta_\varepsilon}]_1 \\ [U_{\theta_\varepsilon}]_2 \\ [U_{\theta_\varepsilon}]_3 \\ \vdots \\ [U_{\theta_\varepsilon}]_n \end{bmatrix} \quad (198)$$

## Appendix B: Intrinsic Formulation Matrices

The formation of the additional  $\mathbf{Z}^+$ ,  $\mathbf{Z}^-$  matrices used in the intrinsic formulation are shown here, taken from [60], [64].

For the  $i^{th}$  element, the matrices are given as

$$\mathbf{Z}_{u_i}^\pm = \mp \underline{C}^{bw} \underline{C}^{Bb} \mathbf{F}_i^* - \bar{f}_i^\mp + \frac{L_i}{2} \left[ \widetilde{\omega}_B \underline{C}^{bw} \underline{C}^{Bb} \mathbf{P}_i^* + \underline{C}^{bw} \widetilde{\dot{C}^{Bb}} \mathbf{P}_i^* \right] \quad (199)$$

$$\begin{aligned} \mathbf{Z}_{\psi_i}^\pm &= \mp \underline{C}^{bw} \underline{C}^{Bb} \mathbf{M}_i^* - \bar{m}_i^\mp + \\ &\frac{L_i}{2} \left[ \widetilde{\omega}_B \underline{C}^{bw} \underline{C}^{Bb} \mathbf{H}_i^* + \underline{C}^{bw} \widetilde{\dot{C}^{Bb}} \mathbf{H}_i^* + \underline{C}^{bw} \underline{C}^{Bb} (\tilde{\mathbf{v}}_i \mathbf{P}_i^* (\tilde{e}_1 + \tilde{\gamma}_i) \mathbf{F}_i^*) \right] \end{aligned} \quad (200)$$

$$\mathbf{Z}_{F_i}^\pm = \pm u_i - \frac{L_i}{2} \left[ \underline{C}^{bw} \underline{C}^{Bb} (e_1 + \gamma_i) - \underline{C}^{Bb} e_1 \right] \quad (201)$$

$$\mathbf{Z}_{M_i}^\pm = \pm c_{WM_i} - \frac{L_i}{2} Q_{WM_B}^{-1} \underline{C}^{Bb} \kappa_i \quad (202)$$

$$\mathbf{Z}_{P_i} = \underline{C}^{bw} \underline{C}^{Bb} \mathbf{v}_i - \mathbf{v}_i - \widetilde{\omega}_B u_i - \dot{u}_i \quad (203)$$

$$\mathbf{Z}_{H_i} = \boldsymbol{\omega}_i - \underline{C}^{bB} \underline{C}^{wb} \boldsymbol{\omega}_i - \underline{C}^{bB} Q_B c_{WM_i} \quad (204)$$

where  $\widetilde{(\quad)}$  indicates the time derivative of a virtual quantity.

The  $\bar{f}_i^\mp$  and  $\bar{m}_i^\mp$  terms are given as follows

$$\bar{f}_i^- = \int_0^1 (1 - \hat{\xi}) \check{f}_B L_i d\hat{\xi} \quad (205)$$

$$\bar{f}_i^+ = \int_0^1 \hat{\xi} \check{f}_B L_i d\hat{\xi} \quad (206)$$

$$\bar{m}_i^- = \int_0^1 (1 - \hat{\xi}) \tilde{m}_{B L_i} d\hat{\xi} \quad (207)$$

$$\bar{m}_i^+ = \int_0^1 \hat{\xi} \tilde{m}_{B L_i} d\hat{\xi} \quad (208)$$